Metabolic maturation and morphological phenotyping of patient-derived induced pluripotent stem cell-derived cardiomyocytes to better understand dilated cardiomyopathy

Alyson Jiang

Degree of Master of Science

Department of Pharmacology & Therapeutics

McGill University, Montreal

September 2023

A thesis submitted to McGill University in partial fulfillment of the requirements of the degree of Master of Science

© Alyson Jiang, 2023

ACKNOWLEDGEMENTS

The journey to completing this thesis could not have been possible without the support of many and I would like to thank them all here.

First and foremost, to my supervisor, Terry, thank you for your continued support, guidance, and encouragement over the years. I deeply admire your work ethic, values, and dedication to your research and to your students. You have fostered a learning environment that has enabled me to grow in so many ways. I genuinely could not have asked for a better lab to do my Master's in. It has been a privilege to work under your supervision.

To Kyla Bourque, you have taught me almost everything I know whether it is how to culture iPSCs or to believe in myself. I owe so much of who I am today to your guidance, support, and kindness. Thank you for being an amazing mentor, colleague, and friend.

To Cara Hawey, Karima Alim, and Grace Mazarura, thank you for all the joy (and laughter) you have brought me during this degree and while culturing iPSCs together. I have learned so much from each of you (GPCR signaling, sarcomere organization, and more). I am grateful to have had you as colleagues and now friends.

Thank you to the members of the Hébert lab (Phan, Domo, Darlaine, Julianna, Étienne, Jace, Jacob, Giada, Aneesah, Ashika, Kim, Hanan, Emma, Robert, and Deanna) for making me love coming to work and for your help whether it was with ordering reagents, training me on equipment, or lending me autoclaved pipette tips. I am so lucky to have worked with all of you.

To Dr. Nicolas Audet, thank you for all your patience, kindness, and help. I could not have developed the Cell Painting assay or taken beautiful images without you. Thank you for teaching me so much and for all the laughs.

Thank you to Jordan Thompson from Revvity for his help and kindness in refining the Cell Painting analysis protocol.

Thank you to members of my thesis advisory committee, Dr. Jean-François Trempe, Dr. Bruce G. Allen, and Dr. Alvin Shrier for all of their feedback and advice in helping me progress through this degree. I am grateful to have had such kind and enthusiastic experts advise me.

Thank you to members of the Heart-in-a-dish project without whom this project would not be possible, particularly Ida Derish, Natalie Gendron, Dr. Cecere, and Dr. Giannetti.

Thank you to the members of the Pharmacology departmental administration team: Nadee, Cathy, Chantal, Hong, and Tina for their positive energy and help in various forms.

Thank you to my friends, especially Sabrina, Simon, Diane, Paary, Jacob, Sofia, and Elaine, for all their emotional support and encouragement when I needed it.

Finally, thank you to my parents and my brother, Daniel, for always supporting me in everything that I do. I would not be anywhere without the love, support, and sacrifice of my family.

TABLE OF CONTENTS

ABSTRACT

The most common indication for heart transplantation and the second most common cause of heart failure is dilated cardiomyopathy (DCM), a disease affecting the heart's ability to deliver oxygenated blood to the body. Given the poor prognosis, there is a need for earlier intervention and more effective treatments for DCM patients. However, diagnosing and treating DCM is made difficult by its diverse causes and heterogeneous clinical manifestations. Our objective is to better understand the distinct phenotypes of DCM, particularly genetic and chemotherapeutic-induced forms, using patient-derived induced pluripotent stem cell-derived cardiomyocytes (iPSC-CMs). iPSC-CMs harbor the same genetic mutations and many of the same features of the disease as the patient from which they were derived. We hypothesize that phenotypic properties of DCM iPSC-CMs reflect underlying disease mechanisms and that generating phenotypic profiles can help stratify DCM patients into defined disease subtypes. We aim to 1) characterize morphological differences between DCM and healthy iPSC-CMs using a high-content imaging-based assay called "Cell Painting", and 2) induce more mature and disease-relevant phenotypes in our iPSC-CMs using media formulations that modify cellular signaling and metabolic profiles. We developed a cell painting assay to characterize features of iPSC-CM, nucleus, mitochondria, and sarcomere morphology at the single cell level in a high-throughput manner with which we demonstrated morphological differences in both control- and DCM patient-derived iPSC-CMs. Additionally, we tested two published metabolic maturation protocols, one of which produced iPSC-CMs with more mature sarcomere organization and gene expression. Generating phenotypic profiles will enable us to better understand disease mechanisms in DCM and cluster patients with similar phenotypic profiles, paving the way for improved diagnostic guidelines, more personalized treatments, and identifying novel drug targets to ultimately improve quality of life and outcomes for DCM patients.

RÉSUMÉ

L'indication la plus courante de transplantation cardiaque et la deuxième cause la plus fréquente d'insuffisance cardiaque est la cardiomyopathie dilatée (CMD), une maladie affectant la capacité du cœur à fournir du sang oxygéné au corps. Compte tenu du mauvais pronostic, une intervention plus précoce et des traitements plus efficaces sont nécessaires pour les patients avec la CMD. Cependant, le diagnostic et le traitement de la CMD sont rendus difficiles par ses causes diverses et ses manifestations cliniques hétérogènes. Notre objectif est de mieux comprendre les phénotypes distincts de la CMD, en particulier les formes génétiques et induites par la chimiothérapie, en utilisant des cardiomyocytes dérivés de cellules souches pluripotentes induites provenant des patients avec la CMD (CM-CSPi). Les CM-CSPi présentent les mêmes mutations génétiques et plusieurs caractéristiques de la maladie que le patient dont ils sont issus. Nous émettons l'hypothèse que les propriétés phénotypiques des CM-CSPi CMD reflètent les mécanismes sous-jacents de la maladie et que la génération de profils phénotypiques peut aider à stratifier la population de patients avec la CMD en sous-types de maladie définis. Notre objectif est de 1) caractériser les différences morphologiques entre les CM-CSPi CMD et sains à l'aide d'un test basé sur l'imagerie à haut contenu appelé "Cell Painting", et 2) induire des phénotypes plus matures et plus pertinents pour la maladie dans nos CM-CSPi en utilisant des formulations de médias qui modifient la signalisation cellulaire et les profils métaboliques. Nous avons développé un protocol de cell painting pour caractériser diverses caractéristiques de la morphologie des CM-CSPi, du noyau, des mitochondries et des sarcomères au niveau de la cellule individuelle d'une manière à haut débit avec laquelle nous avons démontré des différences morphologiques entre les CM-CSPi dérivés de patient contrôle et avec la CMD. De plus, nous avons testé deux protocoles de maturation métabolique publiés, dont l'un a produit des CM-CSPi avec une organisation de sarcomère et une

expression génique plus matures. La génération de profils phénotypiques nous permettra de mieux comprendre les mécanismes de la maladie chez les patients avec la CMD et de grouper les patients présentant des profils phénotypiques similaires, ouvrant la voie à des directives de diagnostic améliorées, à des traitements plus personnalisés et à l'identification de nouvelles cibles médicamenteuses pour finalement améliorer la qualité de vie pour les patients affecté par la CMD.

CONTRIBUTION OF AUTHORS

Ida Derish, Jeremy Zwaig, Elise Rody, Kashif Khan, David Derish, Janice To, and Patrick Young generated the HID project hiPSC lines from patient and control subject blood samples. Cara Hawey developed the sarcomere organization analysis protocol from which the one described in this thesis is adapted from. Dr. Nicolas Audet from the Imaging and Molecular Biology Platform at McGill and Jordan Thompson from Revvity helped develop the hiPSC-CM segmentation analysis protocol. Dr. Nicolas Audet helped develop the percentage mitochondria area analysis protocol.

Unless specified above, all work in this thesis was completed by Alyson Jiang. This thesis was written by Alyson Jiang and edited by Dr. Kyla Bourque and Dr. Terry Hébert.

LIST OF ABBREVIATIONS

ACE inhibitors	Angiotensin-converting enzyme inhibitors
anti-α-actinin-647	anti-α-actinin primary antibody, then Alexa Fluor 647 secondary antibody staining
AT_1R	Angiotensin II receptor type 1
CM	Cardiomyocyte
cTnT/I/C	Cardiac troponin T, cardiac troponin I, and cardiac troponin C
DCM	Dilated cardiomyopathy
EHT	Engineered heart tissue
$ERK_{1/2}$	Extracellular signal-regulated kinase 1/2
GPCR	G protein-coupled receptor
HCM	Hypertrophic cardiomyopathy
iPSC	induced pluripotent stem cell
iPSC-CM	induced pluripotent stem cell-derived cardiomyocyte
KOSR	Knockout serum replacement
LMNA	Lamin A/C
PKA	Protein kinase A
PLN	Phospholamban
PBMC	Peripheral blood mononuclear cells
ROCK inhibitor	Rho kinase inhibitor
WGA-488	Wheat germ agglutinin coupled to Alexa Fluor 488
WGA-555	Wheat germ agglutinin coupled to Alexa Fluor 555

LIST OF FIGURES

LIST OF TABLES

1. INTRODUCTION

1.1 Dilated Cardiomyopathy

Cardiovascular diseases remain the leading cause of death worldwide as many of these diseases will inevitably progress towards heart failure [1]. Heart failure (HF) is a condition in which the heart cannot deliver enough oxygenated blood to the rest of the body and affected approximately 669,600 Canadians as of 2018 [2]. With the 5-year survival rate being only 50% after HF diagnosis [3], there is a need for improved diagnostic and treatment strategies for HF. After coronary artery disease, the second most common cause of HF, accounting for about 36% of cases, is dilated cardiomyopathy (DCM) [4]. As the most common indication for heart transplant, DCM places a significant burden on healthcare systems worldwide [5]. DCM is characterized by the dilatation of the left or both ventricles, thinning of the ventricular walls, and systolic dysfunction. This is a contrast to other types of cardiomyopathies such as hypertrophic and restrictive cardiomyopathy which are characterized by thickening of the ventricular wall and diastolic dysfunction [6].

Diverse causes of DCM include genetic mutations, viral infections, excessive alcoholism, previous exposure to chemotherapeutics, inflammation-mediated events, endocrine or autoimmune diseases, and even pregnancy or connective tissue disorders [7]. In many cases, DCM is clinically labelled as idiopathic, when there is no clear genetic insult and other suspected causes have been excluded. Idiopathic DCM accounts for almost half of DCM cases, though this may be an overestimation as a result of insufficient genetic testing [8]. To further add complexity to the disease, DCM is notorious for its heterogeneous clinical presentation among patients. Symptoms, age of onset, etiology, disease progression, and response to treatments vary from patient to patient. Patients with DCM may present symptoms such as shortness of breath, chest pain, fatigue, or

swelling in the legs, ankles, and stomach. Onset of symptoms may begin at any age ranging from early childhood to the late elderly years, but the disease is most often diagnosed between the ages of 20-50 years old [9]. However, DCM is often underdiagnosed as patients are asymptomatic in the early stages of the disease [10]. This is unfortunate as late diagnosis is associated with poorer outcomes, highlighting the importance of developing improved diagnostic tools to enable clinicians to intervene at earlier stages of the disease [11]. As such, there are few defined phenotypes associated with specific etiologies in terms of biological sex, age of onset, symptoms, and response to treatments [10]. For instance, familial forms of DCM often have variable penetrance or only manifest symptoms in response to additional stressors [12].

Treatments for DCM include pharmacological agents, devices, and etiology-specific treatments. The standard drug therapy for heart failure and DCM is comprised of angiotensin-converting enzyme (ACE) inhibitors (perindopril and ramipril), β-blockers (carvedilol and metoprolol), and angiotensin receptor blockers (valsartan). Other pharmacological therapies for DCM include angiotensin receptor blocker/neurolysin inhibitors (ARNI) (sacubitril/valsartan), aldosterone receptor inhibitors (spironolactone and eplerenone), and sodium/glucose cotransporter-2 (SGLT2) inhibitors (dapagliflozin and empagliflozin) [13]. Response to these therapies may vary from patient to patient and this variability is also affected by the combination of treatments used and the sequence in which these therapies are administered [14, 15]. Device therapy may also be used following or in addition to pharmacological therapies to treat systolic dysfunction. It involves cardiac pacing with either a cardiac resynchronization therapy (CRT)-pacemaker or a combined CRT-implantable cardioverter-defibrillator which can deliver an electric shock to restore regular heart rhythm following arrhythmias in addition to having pacemaker

function [10]. In the case of pharmacological agents and device therapies being insufficient to maintain adequate cardiac output, heart transplantation may be required. Patients may also receive implantation of long-term mechanical circulatory support while awaiting transplantation [10]. The long wait times for heart transplantation highlight a need for additional and improved therapies before reaching such a severe stage. Finally, personalized therapy based on etiology may be necessary in some patients. For example, viral- or inflammation-mediated cases of DCM may require antiviral therapies or immunosuppressive agents. In a prospective, randomized, placebo-controlled study, immunosuppressive therapies resulted in significant improvement in left ventricular ejection fraction (LVEF) in patients with inflammatory DCM who were previously refractory to standard therapy [16]. However, treatment guidelines for etiology-specific cases are currently lacking, in part due to our lack of understanding of etiology-specific mechanisms of DCM [10].

The heterogeneity of DCM etiologies and clinical presentations make it difficult to achieve early diagnosis, guide clinical decision-making, personalize therapies, and inform therapeutic development. Toward this end, there is a clear need to better understand the underlying mechanisms of DCM progression.

1.2 Cardiomyocyte dysfunction and pathophysiology of DCM

1.2.1 Cardiomyocyte dysfunction in DCM

To gain insight into the molecular events underlying DCM, we must first examine the mechanisms at play in cardiomyocytes (CMs), the cells responsible for the heart's contractile

function which comprise 70-80% of the heart's volume [17]. The contractile unit of the cardiomyocyte is the sarcomere. Each sarcomere is composed of interlacing thick myosin and thin actin filaments that, in response to calcium binding, slide along each other to shorten and initiate contraction [18]. The process of converting electrical stimulation from action potentials into muscle contractions is known as excitation-contraction coupling [19]. This process begins with an action potential that depolarizes the plasma membrane of CMs. Membrane depolarization triggers the opening of L-type calcium channels (LTCCs) and the influx of calcium ions into the cell. The influx of extracellular calcium then triggers a large-scale release of calcium from intracellular calcium stores in the sarcoplasmic reticulum (SR) into the cytosol via ryanodine receptors (RyRs). Cytosolic calcium then binds to the troponin complex anchored to the myofilament which causes a conformational change in the tropomyosin component of the thin filament to move aside and allow for the thin and thick filaments to interact and initiate contraction [19]. The troponin complex has three subunits: troponin T anchors the complex to tropomyosin, troponin I blocks myosin binding sites on actin until calcium is bound, and troponin C binds calcium [20]. Contraction stops when calcium is released from the troponin complex and leaves the cytosol either by exiting the cell via the sodium-calcium exchanger (NCX) or by being taken back up into the SR via the sarco-endoplasmic reticulum Ca^{2+}-ATPase (SERCA2a) [19].

Excitation-contraction coupling is a highly regulated process and as such, dysregulation in any of its components can compromise the function of the heart and lead to disease. It is therefore unsurprising that most DCM-causing genetic mutations are found in genes that encode sarcomere proteins such as subunits of the troponin complex (cTnT/I/C), cardiac actin, and titin. Titin is a sarcomere protein that stabilizes the thick filament and acts as a spring to maintain passive tension.

Mutations in the titin gene account for 12-25% of familial DCM cases, making it the most common DCM-causing gene [4] [21] [22].

Other cellular processes or structures important to CM health are disrupted in DCM such as calcium handling, electrophysiology, nuclear-cytoskeletal interactions, mitochondria, metabolism, alternative splicing, protein folding, cell adhesion [23], inflammation, autoimmunity, and toxin exposure [10]. For example, alcohol exposure [24] disrupts contractility which can lead to apoptosis and necrosis in DCM and doxorubicin treatment disrupts calcium handling, metabolic function, and antioxidant pathway activation in DCM [25]. This is in line with the fact that other commonly described causal mutations are found in genes encoding nuclear envelope proteins and proteins involved in the cytoskeleton (dystrophin, desmin), cell adhesion, mitochondria, calcium handling, and alternative splicing [23]. Thus, many key processes are disrupted in DCM and may result in impaired contractility or myocyte loss. Further study is required to understand the underlying mechanisms of these changes as many are not fully understood or even identified yet.

1.2.2 G protein-coupled receptor signaling in DCM

Furthermore, the signaling events in the heart that mediate processes crucial to maintaining heart function and in the face of external stressors may also be dysregulated in DCM [26]. Activation of the same small group of G protein-coupled receptors (GPCRs) in the heart, namely the α- and β-adrenergic receptors, angiotensin II receptor type 1 (AT_1R), and endothelin receptors regulate normal, adaptive, and maladaptive responses in the heart, but it is not well understood how signaling pathways downstream of these receptors choose between each of these fates. Acute

activation of these pathways regulate cardiac contractility, heart rate, growth, and survival whereas chronic activation can result in pathophysiological responses such as cardiac hypertrophy and cardiomyocyte death [26].

Acute β-adrenergic stimulation in the heart via β1-adrenergic receptors, in response to endogenous agonists such as epinephrine and norepinephrine, serves to increase rate and force of contraction in response to increased demand and as an early compensatory mechanism in cases of cardiac dysfunction. In contrast, chronic β-adrenergic stimulation is associated with receptor downregulation, CM apoptosis, and heart failure [27]. The success of β-blockers as therapeutics for heart failure has been in part accredited to their ability to block the adverse effects of chronic β-adrenergic stimulation [28, 29]. β-adrenergic receptors are also found in the vasculature, predominantly β2-adrenergic receptors, wherein stimulation of these receptors induces relaxation and dilation of blood vessels [30].

Angiotensin II receptors, activated upon binding to the angiotensin II peptide hormone, are important for cardiac function as they regulate vascular tone and blood pressure via the renin-angiotensin-aldosterone axis. These receptors have been reported to be dysregulated in various cardiovascular diseases [31, 32]. Acute activation of the AT_1R in the vasculature results in vasoconstriction and sodium retention to increase blood pressure as a compensatory mechanism in response to declining cardiac output. Acute AT_1R activation also mediates cell growth at the CM level [33]. However, chronic activation of the AT_1R results in cardiac remodeling, fibrosis, cardiac hypertrophy, and hypertension [34]. ACE inhibitors and angiotensin receptor blockers are

successful in treating heart failure as they antagonize the adverse hypertensive effects of chronic AT_1R activation.

Endothelin receptors, ET_A and ET_B, located in the heart become activated by the potent vasoconstrictor, endothelin-1, which is endogenously produced in endothelial cells [35]. These receptors mediate vasoconstriction in blood vessels [36]. In the heart, these receptors mediate heart rate, and force of contraction upon acute activation, but have been linked to the development of cardiac hypertrophy and fibrosis upon sustained activation [36].

It is challenging to investigate the link between pathway activation and outcome as there are diverse downstream effectors that could be studied at different proximities from the receptor of interest and in different compartments. However, many signaling pathways downstream of the cardiac GPCRs of interest have in common two critical effector pathways involving either protein kinase A (PKA) or extracellular signal-regulated kinase 1/2 ($ERK_{1/2}$) [26, 37]. These two pathways also represent endpoints relevant to cardiac function and disease. In the heart, PKA mediates contractility, heart rate, and apoptosis whereas $ERK_{1/2}$ is associated with mediating hypertrophy, cardioprotection, survival, and remodeling [26].

There is evidence that both these pathways are dysregulated in DCM. One study revealed altered PKA signaling in a familial from of DCM caused by a mutation in the phospholamban gene due to weakened interactions between PKA and phospholamban binding [38]. Phosphoproteomic analysis also unveiled downstream PKA effectors of the PKA-anchoring protein (AKAP), Cypher/ZASP, to play a role in the pathogenesis of DCM in mice [39]. Finally, another study

reported increased $ERK_{1/2}$ signaling altered cardiac actin dynamics via the phosphorylation of cofilin-1 in DCM caused by mutations in the lamin A/C gene [40] .

It has also been observed that nuclear PKA activity in CMs or fibroblasts mediates cardiac hypertrophy [41], whereas cytosolic PKA activity does not induce hypertrophy [42], highlighting the importance of studying compartment-specific pathway activation. As for $ERK_{1/2}$, it can act in the nucleus and cytoplasm to phosphorylate effector proteins that regulate proliferation, survival, apoptosis, and transcription [43, 44]. The role of PKA and $ERK_{1/2}$ in their various downstream pathways and outcomes are contingent on duration, intensity, and compartmental localization, further complicating our understanding of mechanisms underlying DCM [26].

In summary, at the CM level, although not fully understood, various molecular signaling events and functional processes are disrupted in DCM and require further investigation.

1.2.3 Pathophysiology of DCM

In the face of impaired contractility or myocyte loss, the heart will undergo several compensatory mechanisms to buffer the fall in cardiac output. These compensatory mechanisms include the Frank-Starling mechanism, sustained neurohormonal activation, cellular remodeling, an upregulated fibrotic response, and cell death [45] [46]. As a result of impaired contractility, stroke volume and cardiac output decline which lead to an increased blood volume remaining in the ventricles during diastole. The Frank-Starling mechanism describes the process in which the elevated ventricular diastolic volume increases the stretch of the myofibers resulting in CMs

becoming stretched and elongated [47]. Increased sarcomere length results in increased force of contraction and calcium sensitivity at the troponin complex and thereby increases the subsequent stroke volume to initially compensate for the decline in cardiac output. However, persistent stretching of the sarcomeres due to pressure overload in the ventricles can cause the overlap distance between actin and myosin to become insufficient for effective binding and contractions, worsening the progression of DCM and heart failure [47]. At the same time, neurohormonal activation mediated by the sympathetic nervous system and the release of endogenous catecholamines such as norepinephrine and epinephrine cause an increase in heart rate and contractility [46]. These compensatory mechanisms may render a patient asymptomatic during the early stages of disease, but as cardiomyocyte degeneration and volume and pressure overload ensue, clinical symptoms of heart failure will appear [46].

Furthermore, cellular remodeling also takes place to compensate for contractile dysfunction and myocyte death. In response to CM death or dysfunction, adult CMs undergo a hypertrophic response by adding sarcomeres either in parallel or in series as they no longer have the ability to proliferate or regenerate [48]. While these adaptive mechanisms serve to increase cardiac output in the early stages of the disease, prolonged activation of these mechanisms can become maladaptive and worsen disease progression [49]. Sarcomeres added in parallel, known as concentric hypertrophy, result in an increase in CM width and consequently an increase in ventricular wall thickness which can lead to hypertrophic cardiomyopathy with prolonged activation. In contrast, adding sarcomeres in series, known as eccentric hypertrophy, results in an increase in CM length, length of the ventricular wall, and dilation of the heart chambers which can lead to the development of DCM with prolonged activation [50]. Furthermore, pressure overload

and damage to the myocardium can in turn result in CM death which exacerbates thinning of the walls and worsens cardiac dysfunction in DCM [49].

Persistent decline in cardiac output results in the decline of renal blood flow which prompts the kidneys to increase the secretion of renin. Activation of the renin-angiotensin-aldosterone axis increases peripheral blood pressure by increasing peripheral vascular resistance mediated by angiotensin II and by increasing intravascular volume mediated by aldosterone [46]. Although an increase in blood pressure buffers the fall in cardiac output at first, over time the increased systemic resistance makes it challenging for the damaged left ventricle to eject blood. The increase in intravascular volume also burdens the ventricles which can lead to pulmonary and systemic congestion [51]. Furthermore, chronically elevated levels of angiotensin II and aldosterone directly contribute to pathological cardiac remodeling and fibrosis [52]. Fibrosis, a process in which cardiac fibroblasts increase the production of extracellular matrix deposits, serves to heal damaged tissue, provide structural support, and secrete signaling factors that aid in cardiomyocyte survival [53]. However, persistent and excessive extracellular matrix deposition causes scarring of the heart tissue, hardening of the myocardium, reduced compliance of the muscle, reduced filling capacity of the ventricles, and worsening of cardiac dysfunction [51].

In summary, many mechanisms underly DCM at both the CM level and at the whole organ level, but details of these disease processes are not fully understood. A better understanding of these mechanisms in relation to the complex clinical presentations of DCM is required to form early diagnoses and predict treatment responses for patients. One way to bridge this gap is to study these mechanisms in human induced pluripotent stem cell models which recapitulate the same

genetic mutations and many similar features of the disease as the patient from which they were derived from.

1.3 Human iPSC-derived cardiomyocytes as a model of DCM

In recent years, human induced pluripotent stem cells (hiPSCs) [54] and their differentiated derivatives have become an attractive cell source for disease modeling of cardiovascular diseases and therapeutic screening in addition to their use for regenerative medicine purposes [26]. Adult somatic cells, such as fibroblasts or peripheral blood mononuclear cells, can be obtained from patients and be reprogrammed into hiPSCs which can then be directed to differentiate into any cell type of the three germ layers [54, 55]. The use of hiPSCs in disease modeling hold multiple advantages over other cellular models, particularly in the context of studying patient-specific differences in DCM. First, hiPSCs are derived from somatic cells of patients and thus, harbour the same genetic mutations as the patient from which they came from, making them more accurate *in vitro* models of disease in human patients compared to animal models [56, 57]. Most importantly, hiPSCs can recapitulate patient-specific cases of a certain disease, making it especially useful in modeling patient-specific cases of heterogeneous diseases, such as DCM. The use of hiPSCs may eliminate species-specific and inter-personal variations, paving the way for personalized medicine [58]. Secondly, given that the heart cannot sufficiently replace CMs after heart failure due to the terminally differentiated state of mature CMs, proliferative hiPSCs provide an essentially unlimited source of cells until they are ready for differentiation to use for heart disease modeling, drug screening, or to eventually replace lost tissue with regenerative medicine [59]. This offers an advantage over the use of human or animal primary cells which only survive up to 2 weeks in

culture [56, 60]. Finally, the use of hiPSCs does not engender ethical concerns associated with animal models or human embryonic stem cells [59].

Well-defined differentiation protocols have been developed and commercial kits are now available to differentiate hiPSCs into various cell types and lineages. Building upon early embryonic development studies, methods for differentiating hiPSCs into cardiomyocytes (hiPSC-CMs) involve the sequential use of small molecules and/or growth factors added to culture medium to drive hiPSCs down a mesodermal fate to differentiate into CMs [26]. Temporal modulation of the Wnt signalling pathway is a commonly used method to generate CMs from hiPSCs by initially activating and later inhibiting Wnt signalling in the initial absence of insulin followed by the reintroduction of insulin later on in the differentiation process [61]. Insulin suppresses the formation of the mesoderm, the germ layer from which CMs are derived from, which explains why insulin is only introduced in later steps of many differentiation protocols [62]. Another commonly used hiPSC-CM differentiation method utilizes the growth factors BMP-4 and Activin A to drive hiPSCs towards a CM fate as BMP-4 stimulates the endogenous production of Wnt ligands [63].

Many familial forms of DCM have been studied using hiPSC-CM model systems. In one study, hiPSC-CMs were generated from a family of DCM patients carrying the R173W point mutation in the gene encoding the sarcomere protein, cardiac troponin T (TNNT2), and demonstrated that the DCM hiPSC-CMs exhibited altered calcium handling, decreased contractility, and abnormal sarcomere distribution compared to healthy hiPSC-CMs. The authors then showed that a 7-day treatment with 10 μM norepinephrine (NE), as a model for β-adrenergic stress *in vitro*, resulted in DCM hiPSC-CMs exhibiting reduced beating rates, reduced contractile

forces, and a significantly higher number of cells with abnormal sarcomere organization. This suggested that DCM hiPSC-CMs were more sensitive to β-adrenergic stress compared to healthy controls. Treatment with β-blockers, 10 μM carvedilol or metoprolol, for 24 hours was protective against the NE stress-induced responses [64].

hiPSC-CMs have also been used to some extent as patient-specific predictive models of disease. Doxorubicin is a commonly used anthracycline chemotherapy agent for the treatment of cancers such as breast and thyroid cancer. Unfortunately, it is well-established that doxorubicin-treated patients can develop cardiomyopathy that may progress towards heart failure. It is currently not possible to predict which patients will develop doxorubicin-induced cardiotoxicity (DIC), but a study using hiPSC-CMs was able to recapitulate individual predispositions to developing DIC. hiPSC-CMs from breast cancer patients treated with doxorubicin who developed DIC demonstrated decreased cell viability, mitochondrial and metabolic function, calcium handling, and antioxidant pathway activity in response to doxorubicin treatment compared to hiPSC-CMs from breast cancer patients who did not develop DIC. This suggested that hiPSC-CMs derived from breast cancer patients with DIC were more sensitive to doxorubicin toxicity than hiPSC-CMs from breast cancer patients who were not affected [25]. This model not only provides insight into the underlying molecular mechanisms of DIC, but also serves as a potential predictive model of DIC in cancer patients.

Finally, with the advent of CRISPR genome editing technology, studies using hiPSC-CMs can further be refined as CRISPR enables the generation of isogenic control lines. Studies often compare hiPSC-CMs derived from patients with specific mutations to control hiPSC-CMs derived

from healthy individuals. The issue with this method is that it is then difficult to determine if differences observed are attributable to the specific mutations of interest, or to other confounding inter-personal genetic differences [26]. Isogenic control lines enable us to eliminate inter-personal genetic variations beyond the mutation of interest. CRISPR technology also facilitates the generation of mutant lines that otherwise may not be accessible from actual patients [26]. One study utilized CRISPR technology in this manner to study the p.Arg14del mutation in the gene encoding phospholamban (PLN), a regulatory protein involved in calcium reuptake into the SR and ER [65]. This mutation is involved in DCM and severe heart failure. hiPSC-CMs from patients with the p.Arg14del mutation in PLN were generated and then also corrected to generate an isogenic control line. The hiPSC-CMs with the PLN p.Arg14del mutation revealed prolonged calcium transient decay times, irregular beating patterns, and lower forces of contraction compared to isogenic controls and revealed disturbances in lipid transfer via the ER/mitochondria contact sites which could be reversed using calcium scavengers. [65].

In summary, harnessing the ability of hiPSC-CMs to reflect the same genetic makeup as the patient from which they originated from has revolutionized the study of patient-specific cases of disease [66], the development of novel and personalized therapies, and the ability to potentially predict treatment response and disease risk.

1.4 hiPSC-CM morphology in DCM

Beyond functional phenotypes in DCM revealed by hiPSC-CMs, such as altered calcium handling, metabolism, and electrophysiological parameters, morphological phenotypes have also been observed in DCM [67]. The genotype-phenotype link remains poorly understood, however,

and efforts have been made to characterize macro- and ultrastructure phenotypes in conjunction to functional phenotypes as the combination may help identify underlying mechanisms of disease, especially in the context of cellular models of the disease.

1.4.1 Sarcomere alignment in DCM

Sarcomere disorganization is a common feature of hiPSC-CMs from DCM patients compared to controls and reflects the functional phenotype of contractile dysfunction. In DCM, sarcomere organization has also been reported to become increasingly disorganized in response to β-adrenergic stress *in vitro* compared to the response of healthy hiPSC-CMs [64]. Sarcomere disorganization is commonly reported in DCM cases caused by mutations in sarcomere proteins. However, this phenotype has also been reported in *LMNA*-related DCM cases when challenged with a hypoxic environment [68] and in *RBM20*-related DCM cases at baseline and worsened in response to β-adrenergic stress [69]. Sarcomere morphology have most commonly been visualized either by confocal microscopy with immunofluorescence staining for sarcomere proteins such as α-actinin and cardiac troponin T or by transmission electron microscopy for increased detail of Z-lines and A-bands of sarcomeres [64]. The extent of sarcomere disorganization has previously been quantified by the proportion of cells with punctate α-actinin staining [64] or by training image analysis softwares to categorize hiPSC-CMs into levels of sarcomere organization, resulting in a proportion of cells in each category as the output [70].

1.4.2 hiPSC-CM shape and area in DCM

To our knowledge, no difference has been reported in terms of basal cell area in hiPSC-CMs from DCM patients compared to healthy subjects. The opposite case is true in hypertrophic cardiomyopathy (HCM) where HCM hiPSC-CMs are significantly larger than healthy hiPSC-CMs [67]. Cell area and membrane morphology have previously been visualized and measured using immunofluorescence staining and fluorescence microscopy. Membrane stains such as CellMask™ and wheat germ agglutinin (WGA) coupled to a fluorescent probe have both been described previously in cardiomyocytes and hiPSC-CMs [71] [72].

1.4.3 Mitochondrial morphology in DCM

Studies have reported that dysfunction and dysregulation in mitochondrial structure, metabolism, and function contribute to the pathogenesis of DCM [73]. Morphological phenotypes in mitochondria and their networks have also been observed in DCM [74]. For example, one study found that hiPSC-CMs from DCM patients with *DNAJC19* mutations had highly fragmented mitochondrial networks and swollen mitochondria with highly disorganized cristae compared to elongated mitochondria with organized cristae found in healthy hiPSC-CMs [74]. hiPSC-CMs were stained with TOMM20, a translocase of the outer mitochondrial membrane, to visualize mitochondrial networks. Transmission electron microscopy was used to visualize detailed mitochondrial ultrastructure such as cristae organization and mitochondrial morphology [74].

Furthermore, it has been established that during the early stages of DCM, mitochondrial number will increase as a compensatory mechanism to sustain a high energy supply [75]. However, as the disease progresses, the number of mitochondria will decline, resulting in decreased ATP production, reduced contractility, and increased reactive oxygen species production which all lead to systolic dysfunction and heart failure [73]. Mitophagy, the process of removing damaged mitochondria, may also be compromised in DCM, resulting in the accumulation of damaged mitochondria [73]. Mitochondrial mass, an indicator of total mitochondria number, can be measured by flow cytometry [76] or confocal microscopy [77] after staining mitochondria with the fluorescent probes, MitoTracker^{TM} Green or Nonyl Acridine Orange. These two probes will accumulate in mitochondria regardless of mitochondrial membrane potential [76]. Membrane potential-dependent compounds such as JC-1 [78] or MitoTracker^{TM} Deep Red have previously been used with MitoTracker^{TM} Green or Nonyl Acridine Orange to assess mitochondrial potential per unit of mitochondrial mass on a single cell basis or in a single mitochondrion as means to measure healthy mitochondrial mass [77].

Finally, in cardiomyocytes, mitochondria are divided into three subpopulations based on their location, function, and morphology: subsarcolemmal mitochondria, intermyofibrillar mitochondria (IFM) and perinuclear mitochondria (PNM) [79]. PNM are clustered around the nucleus and have well developed cristae, enabling them to generate higher levels of ATP [80]. In contrast, IFM lie closely parallel to sarcomeres [81]. Immature CMs are characterized by having more PNM than IFM until they mature and develop increased IFM networks along their sarcomeres [82]. In failing hearts, it has been reported that PNM are more susceptible to membrane potential depolarization than IFM at baseline and under physiological stress [83]. Therefore,

investigating mitochondrial distribution may provide insight into the state of disease and maturity of CMs, especially if using membrane potential-dependent dyes such as MitoTracker Deep Red.

1.4.4 Nuclear morphology in DCM

Studies have also reported altered nuclear morphology associated with DCM. A study characterized hiPSC-CMs generated from a father and son with an E342K mutation in the *LMNA* gene, which encodes nuclear lamins, revealed abnormal and irregular nuclear morphologies, altered gene expression, as well as electrophysiological abnormalities. Lamins are intermediate filament proteins found in the nuclear lamina and matrix that are essential for nuclear integrity, function, and anchoring of cytoskeletal components important for mechanotransduction and contractility within CMs [84]. Transmission electron microscopy identified that *LMNA*-mutated hiPSC-CMs had highly indented nuclei, invisible nuclear lamina, and significantly increased nuclear perimeters due to irregular nuclear shape compared to control hiPSC-CMs that had very round nuclear morphologies and visible nuclear lamina [84].

Another study generated hiPSC-CM lines with L35P, R249Q, and G449V mutations in the *LMNA* gene, each of which affected a different domain of the lamin A/C protein, and observed altered nuclear shape in the L35P and R249Q hiPSC-CM lines, but not in the G449V-mutated hiPSC-CM lines [85]. To further highlight the phenotypic variability of *LMNA* mutations in DCM, another study generated seven hiPSC-CM and hiPSC-derived cardiac fibroblast (hiPSC-CFs) lines each carrying different mutations in *LMNA* (M1I, R216C/R399H, R216C from a male subject, R216C from a female subject, R335Q, R337H, and R541C) and observed various types of irregularities in nuclear membrane morphology in the hiPSC-CFs, but none in the hiPSC-CM lines

[86]. Together, these studies demonstrate the phenotypic variability of mutations within the same gene, *LMNA,* in DCM and further study is required to understand the underlying mechanisms of these heterogeneous phenotypes. Nuclear morphology may be assessed with immunofluorescence labelling of Lamin B1 in the nuclei or staining with DAPI or Hoechst followed by image acquisition with a fluorescence microscope. Image analysis tools can measure morphological properties such as nuclear circularity index, area, and volume [85].

We have highlighted various morphological phenotypes at the level of the myofilaments, mitochondria, nuclei, and basal cell area in DCM and it is clear that phenotypic variability is prevalent among all of these cellular components, even among mutations in the same causative gene. Identifying and understanding the link between genotype and phenotype may reveal important nuances to the cause and progression of DCM in specific patients.

1.4.5 Cell painting to characterize morphology of hiPSC-CM patient lines

Methods for identifying genotype-phenotype links at the individual component level have been discussed above, but there has recently been a push for methods that can stratify multiple structures within a single cell simultaneously with a view toward phenotyping. “Cell Painting” [87], is one of them. This method multiplexes 6 fluorescent probes to visualize various cellular components or organelles such as the nucleus, cytoskeleton, mitochondria, the Golgi apparatus, the cell membrane, endoplasmic reticulum, cytosolic RNA presence, and more. The protocol involves seeding cells into micro-well plates, staining with six fluorescent probes, perturbing cells with genetic or chemical stressors, and then acquiring images using a high-throughput microscope.

Alternatively, cells can also be stained and visualized at baseline. An automated image analysis software then identifies individual cells and extracts ~1500 morphological features of size, shape, texture, intensity, and more for each cellular component to generate rich morphological profiles (**Figure 1).**

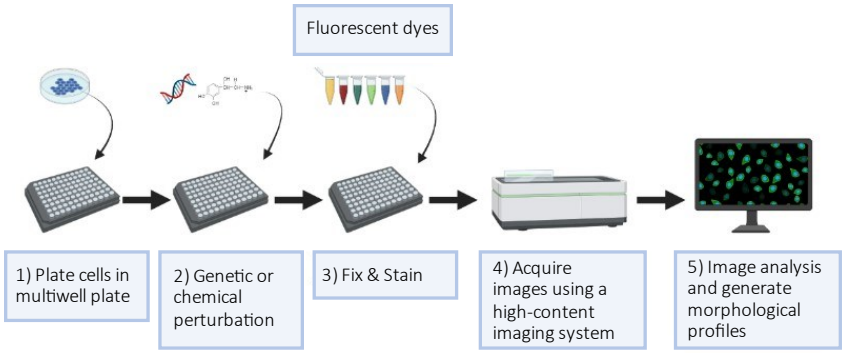

Figure 1. Cell Painting Workflow. The method consists of plating cells in multiwell plates, adding chemical or genetic perturbations, fixing cells, staining with dyes, acquiring images with a high-content screening system, and finally, using image analysis to extract morphological features.

These morphological profiles enable the detection of subtle phenotypes, paving the way for understanding underlying disease mechanisms, drug screening, and the identification of disease biomarkers [87]. This method has now become easier as commercial kits and analytical software for this purpose have become more readily available [88]. The protocol can also be modified by replacing the original dyes with ones more suitable to particular experimental objectives. This method can be used for phenotyping and comparing various mutated hiPSC-CM lines from DCM patients to better understand their genotype-phenotype associations.

1.5 Maturation of hiPSC-CMs

Although hiPSC-CMs hold enormous potential for modeling heart diseases and have created platforms for the discovery of novel phenotypes, therapies, and diagnostic or predictive tools, the largest barrier to their widespread use is their immature phenotype. Immature CMs lack, among other features, proper sarcomere alignment, a rod-shaped phenotype, sufficient expression of certain ion channels and sarcomere proteins, proper mitochondrial distribution, fatty acid metabolism, and electrophysiological and biochemical characteristics that are necessary for mature CM function (**Table 1** and **Figure 2A**) [82]. Additionally, immature CMs beat spontaneously whereas adult CMs only beat in response to pharmacological or electrical stimulation [82].

The immaturity of hiPSC-CMs make them *incompletely adequate* representations of adult CMs found in patients which may hamper the translation of their applications into the clinic. This is of particular concern as heart disease is most often diagnosed in middle-aged adults. Therefore, in recent years, more research has been geared towards understanding the mechanisms of cardiomyocyte maturation and identifying methods to drive maturation in hiPSC-CMs, *in vitro*. Currently, no single method has successfully matured hiPSC-CMs to a fully 'adult-like' and mature state, but significant progress in this field has been made. Recent advances in hiPSC-CM maturation methods have focused on metabolic maturation, co-cultures, manipulation of substrate stiffness, prolonged time in culture, electrical pacing and mechanical strain, and 3-dimensional (3D) culture models which we describe below (**Figure 2B**) [82, 89, 90].

1.5.1 Metabolic maturation of hiPSC-CMs

Over the years, various cell culture additives have been introduced to hiPSC-CM culture media formulations and have achieved varying degrees of success in enhancing maturity in these cells [82, 89]. The feasibility and low costs of media formulation-based maturation methods make them attractive methods for most research groups compared to methods that require more specialized and expensive equipment such as instruments to generate mechanical and electrical stimulation.

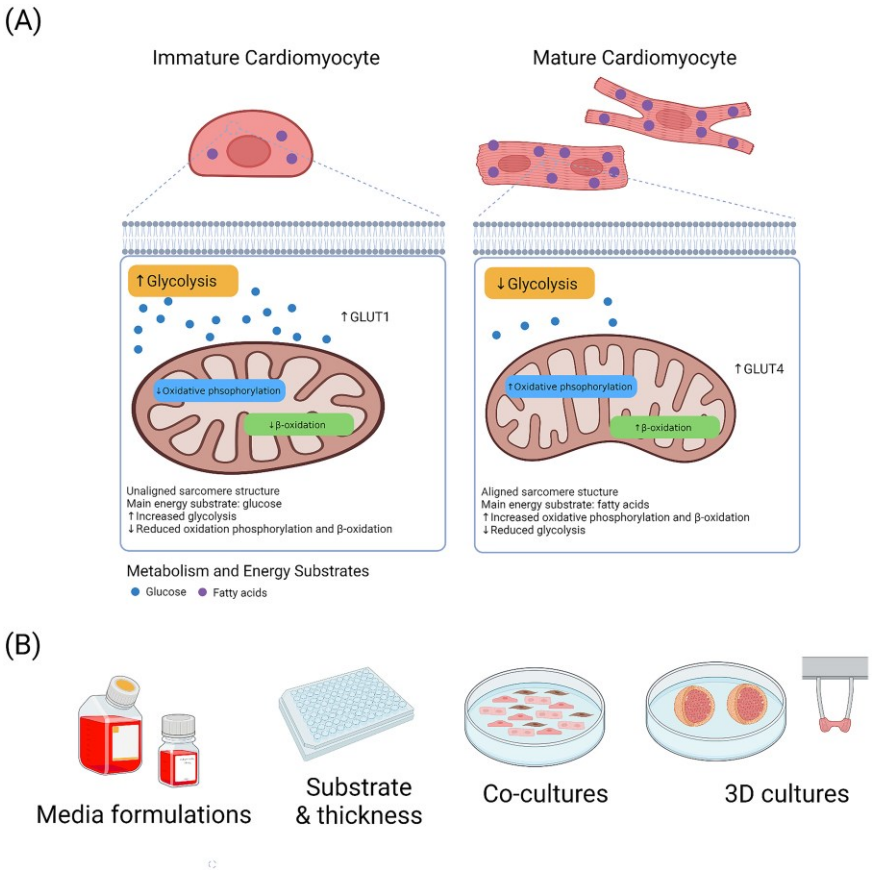

Figure 2. Comparison of Immature and Mature CMs and Maturation Methods from Bourque *et al.* with permission [26] **(A)** Differences between immature and mature cardiomyocytes include sarcomere organization, primary energy substrates, primary form of metabolism, and mitochondria morphology. **(B)** Methods to mature hiPSC-CMs *in vitro* include

media formulations containing agents such as fatty acids or hormones, manipulating substrate type and stiffness, co-culture with non-cardiomyocyte cells, and 3D cultures such as organoids.

	Immature cardiomyocytes	**Mature cardiomyocytes**
Morphology	Round shaped, small	Elongated and rod-shaped, large
	Mononucleated	25–30% Binucleated
Sarcomere organization	Short and poorly organized sarcomeres	Long and well-organized sarcomeres
	Reduced M-line formation	Increased M-line formation
Sarcomere Length	~1.6 μm	~2.2 μm
Myofibrillar isoform switches	Titin: *N2BA* Myosin heavy chain: *MYH6* Troponin I: *TNNI1* Myosin light chain: *MYL7*	Titin: *N2B* Myosin heavy chain: *MYH7* Troponin I: *TNNI3* Myosin light chain: *MYL2*
Mitochondria Structure	Small and round-shaped, reduced formation and organization of cristae	Oval-shaped, occupy ~30% of total cardiomyocyte volume, and increased formation and organization of cristae
Mitochondrial distribution	Close to nucleus and at cell periphery	Aligned in the direction of the sarcomere in longitudinal rows between myofilament bundles, under the sarcolemma, and on opposite sides of the nucleus
Metabolism	Glycolysis Main energy substrate: glucose	Oxidative Phosphorylation and β-oxidation Main energy substrate: fatty acids
Beating	Spontaneous beating	Non-spontaneous beating
Contractility	Smaller contractile force and asynchronous contraction	Larger contractile force and synchronous contraction
Electrophysiology	Upstroke velocity: ~ 50 V/s	Upstroke velocity: ~ 250 V/s
	Resting Membrane Potential: ~ − 60 mV	Resting Membrane Potential: ~ −90 mV
	Reduced ventricular ion channel expression (ex: *KCNJ2*)	Increased ventricular ion channel expression (ex: *KCNJ2*)
	Increased level of automaticity ion channels (ex: *HCN4*)	Decreased level of automaticity ion channels (ex: *HCN4*)
	Increased reliance on calcium currents rather than sodium currents for action potential generation	Increased reliance on sodium currents rather than calcium currents for action potential generation
Calcium handling	Reduced calcium handling: Reduced expression of calcium handling molecules and proteins (ex: LTCC, *RYR2*, and *SERCA2a*)	Increased calcium handling: Increased expression of calcium handling molecules and proteins (ex: LTCC, *RYR2*, and *SERCA2*)

	Reduced size, content, and organization of sarcoplasmic reticulum	Increased size, content, and organization of sarcoplasmic reticulum
T-tubule networks	None/underdeveloped T-tubule network	Extensive T-tubule network
Proliferation	Highly proliferative (hyperplasia)	Undergo hypertrophy and reduced proliferation

Table 1. Properties of immature versus mature cardiomyocytes from Bourque *et al.* with permission [26, 82, 89-93]. Legend: *KCNJ2* encodes the inward-rectifier potassium channel subfamily J member 2 (Kir2.1); *HCN4* encodes the hyperpolarization activated cyclic nucleotide gated potassium channel 4; LTCC: L-type calcium channel; *RYR2* encodes ryanodine receptor 2 found in the sarcoplasmic reticulum of cardiac muscle cells; *SERCA2a*: Ca2+-ATPase expressed in the sarcoplasmic reticulum.

During development, as CMs transition from fetal to neonatal CMs, a radical switch occurs in their cellular metabolism that is essential to their maturation process. Fetal metabolism relies heavily on glycolysis as the main source of ATP generation as the main energy substrates are glucose and lactate during placental nutrition. In contrast, postnatal metabolism relies heavily on fatty acid β-oxidation and oxidative phosphorylation for ATP generation as lipid content in maternal milk becomes the new primary energy substrate [94]. Thus, manipulating substrate energy availability in culture medium is an attractive method to drive hiPSC-CMs towards an *adult-like* phenotype. Following this premise, Yang *et al*. developed a glucose-free medium supplemented with palmitic, oleic, and linoleic acids in complex with albumin [94]. After a 2-week fatty acid (FA) treatment, the treated hiPSC-CMs exhibited numerous markers of improved maturity such as a 59% increase in cell area, modestly decreased circularity index, increased twitch force and action potential upstroke velocity, improved maximal mitochondrial respiratory capacity, and upregulation of genes involved in β-oxidation compared to control cells. Several other studies have reported similar findings after adding the same or modified combinations of FAs to hiPSC-CM culture medium [95-99], making this a reproducible and robust strategy.

Other studies have focused on the addition of hormones to hiPSC-CM culture medium. Supplementing cell culture medium with 20 ng/ml of triiodothyronine (T3) for one week led to increased cell size and sarcomere length, reduced cell cycle activity, and a nearly two-fold higher contractile force per beat in treated hiPSC-CMs compared to control [100]. Glucocorticoids have also been found to be essential for cardiac development given that mice deficient in glucocorticoid receptors have misaligned myofibrils and dysfunctional contractile activity [101]. Even more interesting is that these biochemical cues act synergistically. Treating hiPSC-CMs with a combination of both T3 hormone and dexamethasone (a glucocorticoid agonist) compared to either of them alone resulted in the development of an extensive T-tubule network and increased coupling between L-type calcium channels and ryanodine receptors [102]. Treatment with small molecule activators of the peroxisome proliferator-activated receptor β/δ and gamma coactivator 1α (PPAR/PGC-1α) pathway, asiatic acid and GW501516, promoted hiPSC-CM maturation demonstrated by increased sensitivity to mitochondrial respiratory chain inhibitors and the increased expression of sarcomere, ion channel, and mitochondrial metabolism-related genes [103].

1.5.2 hiPSC-CM maturation via co-culture with cardiac resident cells

In the myocardium, cardiomyocytes represent 70-80% of the mass, but only represent 20-30% of the total cell population. The non-CM cardiac resident cell population is comprised of fibroblasts (27%), endothelial cells (64%), smooth muscle cells, neurons, and immune cells (9%) [89]. These non-CM cells all play important roles in cardiac development and maturation through cell-cell interactions and paracrine signaling [104]. Pasquier *et al*. cultured human embryonic stem cell-derived CMs (hESC-CMs) with endothelial cells (ECs) in 2D cultures and found that ECs

increased synchrony and beating rate of hESCs to near physiological heart rates compared to control [105]. As for fibroblasts, Ieda *et al*. found that fibroblast maturity is crucial to CM maturation. Using mouse hearts, they found that co-culturing with embryonic cardiac fibroblasts induced CM proliferative capacity whereas co-culturing with adult fibroblasts promoted CM hypertrophy and increased sarcomere organization [106]. In 3D microtissues comprised of hiPSC-CMs and cardiac fibroblasts, the CMs displayed improved sarcomere structure and T-tubule networks, improved contractility, increased mitochondrial respiration, and more mature electrophysiological properties compared to microtissues without cardiac fibroblasts [107]. More studies are needed to examine the role of smooth muscle cells, immune cells, and peripheral neurons in CM maturation as these cells are also present in the adult heart, but have been less studied in co-culture with CMs.

1.5.3 hiPSC maturation through the modulation of substrate stiffness

The extracellular matrix (ECM) is a dynamic non-cellular 3D network of collagens, proteoglycans, elastin, fibronectin, and other glycoproteins that bind to each other and to cell adhesion receptors to form a network for cells to reside in. Not only does it provide structural support, it also contains and secretes growth factors and signaling molecules that control survival, proliferation, adhesion, differentiation, and maturation [108]. As CMs mature from the neonatal to adult stage, the stiffness of the ECM, quantified by an elastic modulus value, increases to ~10 kPA in the native adult heart tissue. However, the stiffness of the heart tissue in diseased or fibrosis tissue surpasses this value [109]. Based on this, it could be hypothesized that replicating substrate stiffness near healthy adult physiological values *in vitro* would enhance CM maturity. However,

there is conflicting evidence regarding the optimal stiffness for CM maturation in the current literature. This is in part because underlying mechanisms of how substrate stiffness impacts CM maturation have yet to be fully elucidated and because it is challenging to accurately measure stiffness in an *in vivo* environment [110]. Many studies have manipulated substrate type, stiffness, and micropatterning to induce more mature phenotypes in hiPSC-CMs with varying degrees of success (**Table 2**). There seems to be more solid evidence that substrate stiffness at or above physiological stiffness levels is optimal for maturation, but the role of softer substrates should still be further explored as softer substrates have also yielded improved maturation in hiPSC-CMs [111]. We still lack understanding of the role of substrate stiffness and materials in maturing CMs, hence, further study is required.

Substrate	Optimal stiffness/elastic modulus	Observed maturation effects	Reference
0.4 mm–0.8 mm thick mattress undiluted Matrigel	5.8 kPa	Rod-shaped, ↑max return velocity of twitch, ↑upstroke velocity, ↑expression of *TNNI3* encoding cTnI.	[111]
Poly-ε-caprolactone planar layers	Softer substrate (~0.91 to ~1.53 MPa)	Assembled sarcomeres, ↑expression of α-actinin and myosin heavy chain, organized electromechanical coupling, ↑upregulation of sarcomeric actin mRNA	[112]
Matrigel-coated PDMS coverslips rather than conventional glass coverslips	~1 MPa	2× faster impulse propagation velocities, hypertrophy, ↑expression of ion channel genes (*SCN5A*, *KCNJ2*, ↑Connexin43, ↑myofilament marker (cTnI)	[113]
Polyacrylamide hydrogel	16 kPa	Improved sarcomere alignment and calcium handling	[114]
PDMS	~200 to ~1000 kPa	↓proliferation, mature morphology	[115]
Polyacrylamide	10 kPa + 7:1 (length to width) Matrigel micropatterns	7:1 produced highest translation of sarcomere shortening to mechanical output, aligned myofibrils, ↑mitochondrial content, ↑action potential amplitude and upstroke velocity, more negative resting membrane potential, and T-tubule formation	[109]

Table 2. The effect of culture substrate on cardiomyocyte maturation from Bourque *et al.* with permission [26]. Comparison of different studies testing various substrate materials and thicknesses to culture mature hiPSC-CMs.

1.5.4 Electrical pacing and mechanical strain

The lack of electrophysiological maturity in hiPSC-CMs, as described above, also affects mechanical output as action potentials (APs) trigger calcium-induced calcium release, a process necessary for muscle contraction. As such, subjecting CMs to various mechanical and electrical stimulations to regulate or induce beat rates have induced more mature phenotypes in hiPSC-CMs [89]. In one study, electrical stimulation was applied at the beginning of the differentiation process of hiPSCs into hiPSC-CMs on day 0 for 15 days and was found to induce a more mature phenotype and specialized conduction system phenotype compared to unstimulated cells [116]. In another study, hiPSC-CMs were subjected to mechanical static stress through maintenance around fixed parallel posts and electrical pacing for 2 weeks. Stimulated hiPSC-CMs demonstrated increased sarcomere alignment, contractility, cell size, tensile stiffness, and Frank-Starling force-length relationships [117]. Mechanical and electrical stimulation can improve hiPSC-CM maturity, but are more difficult to implement given the associated costs of specialized equipment required [118].

1.5.5 Time in culture

In 2D monolayer cultures, it has been observed that long-term culture can also increase hiPSC-CM maturity while remaining a cost-effective approach [118]. One study tracked and modeled the development of key ionic currents and calcium handling properties over a period of 30 to 80 days in *in vitro* culture. The authors observed that hiPSC-CMs cultured past 50 days post-

differentiation demonstrated electrophysiological maturation. hiPSC-CMs cultured for more than 50 days also had significantly larger systolic calcium release from the SR and increased calcium, sodium, and potassium currents, contributing to increased calcium handling transients, increased upstroke velocity, and decreased AP duration. Many other studies have also demonstrated hiPSC-CMs with improved electrophysiology following long-term culture [119-122]. The downside of this method is the time it takes to generate hiPSC-CMs that can be used for experiments.

1.5.6 3-dimensional cultures: organoids and engineered heart tissues

Most of the previously mentioned approaches for maturing hiPSC-CMs have been performed in 2-dimensional (2D) cultures. It is important to recognize that CMs in 2D cultures do not recapitulate the complexity of the native heart tissue where the architecture, presence of other cell types, and their interaction with the ECM play a vital role [123]. Therefore, the field has been shifting towards 3-dimensional (3D) hiPSC-CM models [89]. Two types of 3D models have been developed recently: engineered heart tissues (EHTs) and cardiac organoids [124]. EHTs use engineering techniques to construct a 3D cell culture of hiPSC-CMs. For example, the compaction of hiPSC-CMs and hydrogels around two wires or posts, or the accumulation of hiPSC-CMs on an engineered scaffold [124]. Cardiac organoids and their derivatives, on the other hand, are formed through the self-organization of differentiating cardiac cells from hiPSCs [124]. It has been argued that 3D systems are the most successful methods so far to increase maturation of hiPSC-CMs *in vitro*, particularly when coupled with mechanical and electrical stimulation as well as long-term culture [82]. In one study, authors generated 3D scaffold-free human organotypic cardiac microtissues (hoCMTs) from hiPSCs which contained multiple cell types found in the heart. The

hoCMTs beat without external stimuli for more than 100 days in culture and displayed increased length and alignment of sarcomeres, the formation of transverse tubules, higher oxygen consumption rates, and improved cardiac specification compared to standard 2D monolayer cultures. Another study generated EHTs from hiPSC-CMs seeded on a decellularized porcine scaffold and subjected the EHTs to physiologically relevant calcium levels and electrical pacing for 25 days and revealed improved calcium handling, improved cardiac troponin I expression, and robust response to β-adrenergic stress [125]. The combination of multiple maturation methods has made strides towards directing immature hiPSC-CMs towards a more mature phenotype.

These methods have been used to improve maturity in disease models which have enabled more accurate phenotyping of cardiac diseases. For example, metabolic maturation of hiPSC-CMs was performed prior to characterization of electrophysiological phenotypes in hiPSC-CMs from patients with catecholaminergic polymorphic ventricular tachycardia caused by mutations in the cardiac ryanodine receptor gene [126]. Furthermore, cardiotoxicity screens and phenotypic studies of heart diseases such as hypertrophic cardiomyopathy, dilated cardiomyopathy, long QT syndrome, and Duchenne muscular dystrophy have been studied in 3D hiPSC-CM models such as EHTs to increase maturity and biological relevance prior to phenotyping [127].

Although all the methods mentioned above have enhanced maturation in hiPSC-CMs, it is crucial to understand that none of these methods have successfully matured hiPSC-CMs to reflect a fully adult-like phenotype or have even come close. These techniques alone are not sufficient to fully mature hiPSC-CMs. Future directions should look towards using a combination of various methods mentioned and further investigate 3D models and *in vivo* methods to mature hiPSC-CMs.

[89]. Significant progress has been made, but there is still a long way to go before we can fully mature hiPSC-CMs *in vitro* [90].

1.6 Thesis objectives, rationale, and contributions to new scientific knowledge

The diverse etiologies and underlying disease mechanisms along with the heterogeneous clinical presentations of DCM make it a complex disease to identify early on and treat effectively. Despite available treatments, morbidity and mortality remain unacceptably high and many DCM patients will progress to developing heart failure and require cardiac transplantation. There is an urgent need to better understand the distinct phenotypes of DCM and their associated underlying disease mechanisms on a patient-specific basis to develop personalized treatment options to improve DCM patient outcomes.

Many studies have used hiPSC-CMs for personalized disease modeling of cardiac diseases *in vitro* and have demonstrated that patient-derived hiPSC-CMs can recapitulate to a certain extent the features of the disease in the patient from which they were derived. Therefore, hiPSC-CMs from DCM patients of various or unknown etiologies can be studied to understand disease pathways and develop personalized plans and new therapies. For this reason, the "Heart-in-a-Dish" Project, funded by the Courtois Foundation, was founded as a collaborative project led by Dr. Nadia Gianetti, Dr. Renzo Cecere, and Dr. Terry Hébert with the aim of understanding patient-specific differences in DCM, particularly genetic and chemotherapeutic-induced forms of DCM. The objective is to better understand the distinct phenotypes of DCM using patient-derived hiPSC-CMs. We hypothesize that phenotypic properties will reflect underlying molecular mechanisms of

DCM hiPSC-CMs and comparing phenotypic profiles of DCM hiPSC-CMs compared to sex- and age-matched controls will help stratify DCM patients into defined disease subtypes.

Methods and tools for phenotyping or maturing hiPSC-CMs have been published, but remain to be validated by our research group. Work in this thesis aimed to develop new tools and methods for phenotyping DCM using patient-derived hiPSC-CMs. The **specific aims** of this thesis were to: **1)** characterize differences in morphology between DCM hiPSC-CMs and healthy hiPSC-CMs and **2)** induce more mature and disease-relevant phenotypes in DCM hiPSC-CMs.

Associations between DCM-causing genetic mutations and morphological phenotypes in hiPSC-CMs have been reported. Characterizing morphological phenotypes of DCM may shed light onto the underlying disease mechanisms of patient-specific DCM cases or expose the genetic basis of idiopathic forms of DCM. My thesis outlines and tests a workflow for a modified Cell Painting protocol to characterize morphological features of nuclei, mitochondria, basal cell shape and size, cell membrane, and sarcomere organization of DCM hiPSC-CMs, simultaneously and at the single-cell level. Methods in this thesis for characterizing nuclei, cell shape and size, cell membrane, and mitochondria in hiPSC-CMs were new to the Hébert lab. The method for characterizing sarcomere organization was based on the protocol established by Cara Hawey, a previous Master's student in our lab, and improved upon with the addition of a cellular membrane marker, enabling more accurate segmentation of individual hiPSC-CMs within confluent monolayers. This workflow introduces new methods to evaluate ultrastructure in patient-derived hiPSC-CMs enrolled in the Heart-in-a-Dish program. Various troubleshooting and optimization steps led to the establishment of this workflow which are outlined in this thesis.

The immature phenotype of hiPSC-CMs hinders their use in disease modeling applications as they may not fully reflect features of the disease as found in adult CMs *in vivo*. My thesis lays the groundwork for introducing hiPSC-CM maturation methods to the Hébert lab to generate a more disease-relevant model for phenotyping patient-specific differences in DCM. Various optimizing and troubleshooting steps were taken in efforts to validate metabolic maturation protocols published by Funakoshi *et al*. [128] and by Feyen *et al*. [129]. Work presented in this thesis may provide insight into future steps for improving hiPSC-CM maturation in the Hébert lab.

2. MATERIALS AND METHODS

2.1 Cell Lines

Experiments in this thesis were performed in hiPSCs and hiPSC-CMs. The use of hiPSCs in this research was approved by the McGill University Health Centre Research Ethics Board. Peripheral blood mononuclear cells (PBMCs) obtained from consenting patients participating in the "Heart-in-a-Dish" (HID) project were reprogrammed by collaborators in Dr. Renzo Cecere's laboratory into hiPSCs using the Epi5™ Episomal iPSC Reprogramming Kit (Invitrogen, A15960) and the Neon Transfection System (Invitrogen, MPK5000) [130]. To ensure rigorous quality control, hiPSC lines were validated by 1) immunofluorescence staining for core pluripotency markers, 2) RT-PCR to confirm expression of pluripotency genes, and 3) using the tri-lineage differentiation assay (R&D Systems, SC027B) to assess capacity to differentiate into the three germ layers. The hiPSC lines used in this thesis were HID04C (healthy control subject), HID041020 (DCM patient), HID041127 (DCM patient), and AIW002-02 (healthy control subject), see **Table 3**. The HID04C, HID041020, and HID041127 hiPSC lines were generated in the "Heart-in-a-Dish" project and the AIW002-02 hiPSC line was obtained from the Montreal Neurological Institute through the Open Biorepository, C-BIGR. The AIW002-02 hiPSC line has previously been described and validated [131].

Cell Line Identifier	Disease status	Male/Female	Age at HID project entry	Etiology
HID04C	Control	Female	45	N/A
HID041020	DCM	Male	65	Idiopathic
HID041127	DCM	Male	47	Viral

Table 3. hiPSC lines from the HID project used in this thesis.

2.2 Human iPSC maintenance and passaging

2.2.1 Human iPSC maintenance

hiPSCs were cultured in 100-mm tissue culture dishes (VWR, 10062-880) coated with ESC-qualified Matrigel® (Corning, 355277) diluted in DMEM/F12 (Wisent, 319-085-CL). Maintenance media for hiPSCs consisted of the mTESRPlus kit (STEMCELL Technologies, 100-0276) which was changed every two days and double fed on weekends.

2.2.2 Passaging hiPSCs

Passaging of hiPSCs was done when iPSCs were ~80% confluent. Using a light microscope, spontaneously differentiated cells were marked using a permanent marker and removed in a sterile environment through scratching with a 9" Pasteur pipet (Fisherbrand, 63B1367820C). Cells were then rinsed once with warm DMEM/F12 before incubating in gentle cell dissociation reagent (GCDR, STEMCELL Technologies, 100-0485) for 4-5 minutes at room temperature (RT). After aspirating the GCDR, cells were rinsed once again with warm DMEM/F12. Then, hiPSCs were gently lifted using a cell scraper and transferred to a 15 mL conical tube using a 5 mL borosilicate glass pipette. Cells in suspension were centrifuged at 1,200 RPM for 3 minutes at RT. The supernatant was then aspirated and the pellet was resuspended in mTESR Plus by pipetting up and down 6-8 times with a glass pipette. Cell suspension was then split into Matrigel coated plates and topped up to a final volume of 8 mL per 10-cm plate with mTESR Plus.

2.3 Differentiation of hiPSCs into hiPSC-CMs

hiPSCs between passages 2-8 after thawing were directed towards a cardiomyocyte fate using an adapted version of the GiWi iPSC-CM differentiation protocol [132]. On Day -2, spontaneously differentiated cells were removed by scratching, rinsed once with DMEM/F12, and left to incubate in 5 mL of Accutase (Sigma Aldrich, A6964-500ML) at 37°C for 5 minutes. DMEM/F12 was then added to dilute the Accutase solution and the cell suspension was centrifuged at 1,200 RPM for 3 minutes at RT. The supernatant was aspirated and the pellet was resuspended using a p1000 tip stacked on top of a p200 tip (**Figure 3**) in mTESR Plus media supplemented with 10 μM RHO kinase (ROCK) inhibitor Y27632 (Selleck Chemicals, S1049). Using an automated cell counter, cells were counted with trypan blue and plated into Matrigel-coated 24-well plates (Corning, 3526) at a density of 500,000 live cells per well. The next day, medium was exchanged to mTESR Plus medium without ROCK inhibitor. On Day 0, cells were stimulated with 12 μM of CHIR99021 (Cayman Chemicals, 13122), a Wnt activator, in RPMI1640 (Wisent, 350-007-CL) basal medium supplemented with B27 without insulin (50x) (Life Technologies, 0050129SA) (RPMI/B27 without insulin) for 24 hours. On Day 1, medium was exchanged for RPMI/B27 without insulin. On day 3, cells were treated with 5 μM IWP2 (Selleck Chemicals, 3533), a Wnt inhibitor, in RPMI/B27 without insulin for 48 hours. On day 5, medium was exchanged for RPMI/B27 without insulin. On day 7 and day 10, medium was changed to RPMI1640 with complete B27 with insulin (50x) supplement (Life Technologies, 15504-044). On day 12 and day 14, hiPSC-CMs were metabolically selected for by glucose starvation with RPMI without D-glucose (Wisent, 350-060-CL) supplemented with B27 with insulin and 4 mM sodium-L-lactate (Sigma Aldrich, L7022-10G) prepared in HEPES (Fisher Scientific, BP410-500) [133]. On day 16, wells with beating hiPSC-CMs were dissociated with Accutase for 30 minutes at 37°C

and replated into 6-well plates (Thermo Scientific, 140675) coated with human plasma fibronectin (Sigma Aldrich, FC010-10MG) diluted in phosphate buffered saline (PBS) without Ca^{2+}, without Mg^{2+} (PBS) (Corning, 21-040-CM). Replating medium consisted of RPMI1640 with 1X B27 with insulin supplemented with 10% knockout serum replacement (KOSR; Gibco, 10828028) and 10 μM ROCK inhibitor. Cells were washed three times with basal RPMI and medium was changed to RPMI/B27 with insulin the day after replating to remove KOSR and ROCK inhibitor. Cells were maintained in RPMI/B27 with insulin until the start of metabolic maturation experiments or replating into 96-well plates for Cell Painting assays. To replate hiPSC-CMs from 6-well plates into 96-well plates, cells were dissociated with Accutase for 30 minutes at 37°C and replated into fibronectin-coated optical bottom, black 96-well plates (Thermo Scientific Nunc, 165305) using RPMI1640 with B27 with insulin supplemented with KOSR and ROCK inhibitor. Cells were maintained in RPMI/B27 with insulin until at least day 28 before being used in assays.

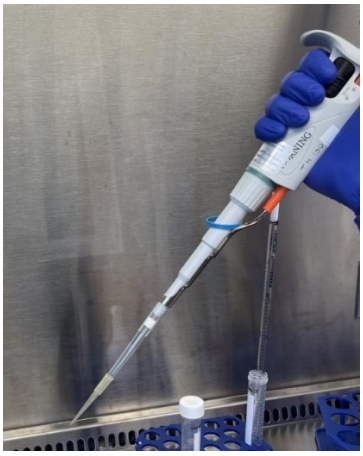

Figure 3. p1000 tip on top of p200 tip used for resuspending hiPSC pellet during Day -2 of hiPSC-CM differentiation protocol.

2.4 Metabolic maturation media

The first metabolic maturation medium (MM) tested in our monolayer hiPSC-CMs was adapted from the published protocol by Funakoshi *et al.* [128]. At day 16 of our hiPSC-CM

differentiation protocol, hiPSC-CMs were seeded at a density of 2 million cells per well in 6-well plates. The next day, medium was exchanged for RPMI/B27 with insulin to remove ROCK inhibitor used during the replating step. Cells were maintained in RPMI/B27 for 3-4 days before switching to maturation medium composed of DMEM low glucose (1g/L) (Thermo Scientific, 11885084) supplemented with 200 μM BSA-Palmitate Saturated Fatty Acid Complex (Cayman Chemical, 29558), 100 ng/mL dexamethasone (Bioshop, DEX002) in DMSO, 4 nM T3 hormone (3,3′,5-Triiodo-L-thyronine sodium salt, Sigma, T6397), and 1 μM of the PPARα agonist, GW7647 (Sigma, G6793), in DMSO. In the original publication, the authors complexed their palmitic acid with bovine serum albumin (BSA) themselves, but we lacked the necessary equipment and therefore used palmitic acid already in complex with BSA purchased from Cayman Chemical. hiPSC-CMs were maintained in MM for 9 days and then in DMEM low glucose with 200 μM BSA-palmitic acid for the following 5 days. Cells in the control condition were maintained in RPMI/B27 with insulin.

The second metabolic maturation medium tested in our hiPSC-CM monolayers was by Feyen *et al*. [129]. hiPSC-CMs were plated at 2 million cells per well in a 6-well plate and then glucose starved for 3 days using RPMI without glucose with B27 prior to switching to the maturation medium. The maturation medium was composed of DMEM no glucose (Thermo Scientific, 11966025) supplemented with 3 mM glucose (Sigma, G7021), 10 mM sodium-L-lactate, 5 mM creatine monohydrate (Sigma, C3630), 2 mM taurine (Sigma, T0625), 2 mM L-carnitine (Sigma, C0283), 0.5 mM ascorbic acid (Sigma, A8960), 0.5% (w/v) AlbuMAX^{TM} I Lipid-Rich BSA (Thermo Scientific, 11020021), 1x MEM Non-Essential Amino Acids Solution (Thermo Scientific, 11140076), 1x B27, 1% KOSR, 5 mg/mL Vitamin B12 dissolved in dH_2O (Sigma,

V6629), and 0.82 μM biotin dissolved in dH_2O (Sigma, B4639). We maintained hiPSC-CMs in maturation medium for 3-5 weeks, changing medium every three days, as directed by the original protocol. Control hiPSCs were maintained in RPMI/B27.

2.5 Gene expression studies to validate the effect of maturation media on hiPSC-CMs

RNA was isolated from samples resuspended in 1 mL TRI reagent® RNA Isolation Reagent (Sigma, T9424) and vortexed for 30 seconds before being left to incubate at RT for 5 minutes. 200 μL bromo-chloro-propane (BCP) was then added to samples before vortexing for 10 seconds and incubating for 15 minutes at RT. Samples were then centrifuged at 12,000 RPM for 15 minutes at 4°C and then kept on ice moving forward. Supernatants were transferred to new RNase-free low retention Eppendorf tubes. Isopropanol was added to the sample supernatants in a 1:1 ratio before being vortexed lightly for 5 seconds and being left to incubate for 15 minutes at RT. Sample supernatants in isopropanol were then centrifuged for 8 minutes at 12,000 RPM at 4°C. Sample tubes were then inverted to gently remove supernatant without disturbing the pellets. Pellets were gently detached with cold 70% ethanol before being centrifuged at 7500 RPM for 5 minutes at RT. Supernatant was removed by inversion and pellets were air-dried. Dry pellets were resuspended in RNAse free water and quantified with a NanoDrop microvolume spectrophotometer.

Isolated RNA was treated with DNAse to digest contaminant genomic DNA. Then, the isolated RNA was reverse transcribed into cDNA using random hexamer primers and M-MLV reverse transcriptase. qRT-PCR was performed using the BrightGreen 2X qPCR Mastermix – No

Dye kit (Applied Biological Materials, MasterMix-S-XL) on a ViiA 7 Real-Time PCR System (Thermo Scientific). Fold change in expression of each gene was normalized to the housekeeping gene, *GAPDH*. Refer to **Table 4** for primer sequences.

Gene target	Forward sequence (5' -> 3')	Melting Temperature (°C)	Reverse Sequence (5' -> 3')	Melting Temperature (°C)
GAPDH	GGCAAATTCCA TGGCACCGTCA	60.8	ATCGCCCCACTT GATTTTGGAGG	59.8
GATA4	GCCTGTCATCTC ACTACGGGCA	61.1	TGAGAACGTCTG GGACACGGAG	60.7
NKX2.5	CACCGGCCAAG TGTGCGTCT	63.1	GCAGCGCGCACA GCTCTTTC	62.4
TNNI1	CCAACCTCAAGT CTGTGAAGAAG	55.5	TCGGAGACTTGG CGGCATCAAA	61.3
TNNI3	GGTGGACAAAG TGGATGAAGAG	55.6	GGTGGGCCGCTT AAACTTG	56.9

Table 4. Primer sequences for GAPDH, GATA4, NKX2.5, TNNI1, and TNNI3 primers used for validation of metabolic maturation protocols.

2.6 Characterizing hiPSC-CM morphology using Cell Painting

Various dyes, antibodies, and conditions were optimized to build our preliminary workflow for characterizing morphological differences in hiPSC-CMs. See **Table 5** for a comprehensive list of reagents used in troubleshooting of the Cell Painting protocol described in this thesis.

Dye, antibody, kit	Description	Brand and catalog number
PhenoVue Cell Painting JUMP Kit 1 [88]	Contains: • **PhenoVue Hoechst 33342 Nuclear Stain** • **PhenoVue Fluor 488 - Concanavalin A** (endoplasmic reticulum)	Revvity (previously Perkin Elmer), PING21

	• **PhenoVue 512 Nucleic Acid Stain** • **PhenoVue Fluor 555 – WGA** (cell membrane and Golgi apparatus) • **PhenoVue Fluor 568 – Phalloidin** (actin filaments) • **PhenoVue 641 Mitochondrial Stain**	
Hoechst nucleic acid stain	Stains nuclei	Thermo Scientific, H3570
MitoTracker™ Deep Red FM	Mitochondrial membrane potential-dependent dye	Thermo Scientific, M22426
Wheat Germ Agglutinin Conjugated to Alexa Fluor™ 488 (WGA-488)	Cellular membrane stain	Thermo Scientific, W11261
Wheat Germ Agglutinin Conjugated to Alexa Fluor™ 555	Cellular membrane stain	Thermo Scientific, W32464
DRAQ5™ Fluorescent Probe Solution	DNA-stain (also stains cytosol at lower intensity than nucleus)	Thermo Scientific, 62251
Mouse anti-α-actinin primary antibody	Sarcomere marker	Sigma, A7811
Goat anti-mouse IgG Alexa Fluor™ 555 secondary antibody	To visualize sarcomeres in the 555 channel (used in the second version of the Cell Painting protocol)	Thermo Scientific, A-21422
Rabbit anti-mouse IgG Alexa Fluor™ 647 secondary antibody.	To visualize sarcomeres in the 647 channel (used in the first version of the Cell Painting protocol)	Thermo Scientific, A-21239

Table 5. Reagents used in troubleshooting steps and finalized versions of the Cell Painting protocol for characterizing hiPSC-CM morphology.

Two versions of the finalized Cell Painting protocol were tested. The first version involved a live cell staining component and a fixed cell staining component wherein mitochondria morphology and sarcomere morphology were acquired from different cells. The second version of the protocol involved a live cell staining step followed by a fixed cell staining step which enabled

us to extract mitochondrial morphology features and sarcomere morphology features from the same individual cells. The fixed cell staining protocol from the first version of the Cell Painting protocol was used to assess sarcomere organization for validation of the metabolic maturation protocol by Feyen *et al*. [129].

2.6.1 Cell Painting protocol 1: Live cell staining of mitochondria, membrane, and nucleus

hiPSC-CMs in 96-well plates were rinsed twice with Krebs' solution (KREBS) without calcium to remove cell debris and deplete calcium to slow beating. Cells were incubated with 1 μg/mL Hoechst in KREBS without calcium for 10-15 minutes at 37°C. Hoechst solution was removed and rinsed before incubating cells with 50 nM MitoTracker™ Deep Red in KREBS without calcium for 30 minutes at 37°C. MitoTracker™ Deep Red solution was removed and cells were rinsed once before incubating with 5 μg/mL WGA-488 in KREBS without calcium for 10 minutes at 37°C. The plate was immediately imaged afterwards using the Opera Phenix Plus High Content Screening System using a 40X water objective. See **Table 6** for excitation and emission filters used.

Dye	Excitation filter	Emission filter
Hoechst nucleic acid stain	375 nm	435 - 480 nm
Wheat Germ Agglutinin - Alexa Fluor 488	488 nm	500 - 550 nm
MitoTracker Deep Red Mitochondrial Stain	640 nm	650 - 760 nm

Table 6. Excitation and emission filters used for live cell imaging in first version of Cell Painting of hiPSC-CMs.

To make KREBS, add 29.2 mL of 5 M NaCl, 4.2 mL of 1 M KCl, 1 mL of 0.5 M $MgCl_2$, 20 mL of 0.5 M HEPES (pH=7.4), and 1 g of glucose to a 1 L beaker. Top volume to 1 L with distilled and deionized water. Adjust pH to 7.4 and keep at RT in the dark.

2.6.2 Cell Painting protocol 1: Fixed cell imaging for sarcomere, membrane, and nucleus morphology

Certain ultrastructure features, such as sarcomere organization, cannot be visualized in live cells as they require fixation and cell permeabilization. hiPSC-CMs in 96-well plates were rinsed 2-3 times with warm RPMI/B27 to remove cell debris before being incubated with 5 μg/mL wheat germ agglutinin (WGA) conjugated to Alexa Fluor™ 488 (WGA-488) (Thermo Scientific, W11261) dissolved in KREBS buffer without calcium for 10 minutes at 37°C to live stain hiPSC-CM membranes. After WGA-488 incubation was complete, cells were rinsed once with KREBS buffer without calcium and fixed with 2% paraformaldehyde for 10 minutes at RT. Fixed cells were then permeabilized with 0.3% Triton™ X-100 (Sigma, X100) in PBS for 10 minutes at RT and then blocked with 5% bovine serum albumin (BSA, Bioshop, 9048-46-8) solution in PBS for 1-4 hours at room temperature on a rotating platform shaker to prevent non-specific antibody binding. Blocking solution was then removed and fixed cells were incubated with a monoclonal mouse anti-α-actinin primary antibody (1:200, Sigma , A7811) in 5% BSA in PBS solution overnight at 4°C to bind to sarcomeres. The next day, the primary antibody was removed, and cells were incubated with a rabbit anti-mouse IgG Alexa Fluor 647 secondary antibody (1:1000, Thermo Scientific, A-21239) for 1-3 hours at RT. Secondary antibody was then discarded, and cells were incubated with 1 μg/mL Hoechst nucleic acid stain (Thermo Scientific, H3570) for 10 minutes at RT. Image acquisition was performed in the Opera Phenix Plus High Content Screening System (Revvity, previously Perkin Elmer) using a 40X water objective. See **Table 7** for excitation and emission filters used. Morphological features of sarcomeres, nuclei, and cell membranes were then measured for validation of maturation protocols and for characterizing hiPSC-CM morphology.

Dye	Excitation filter	Emission filter
Hoechst nucleic acid stain	375 nm	435-480 nm
Wheat Germ Agglutinin – Alexa Fluor 488	488 nm	500-550 nm
Rabbit anti-mouse IgG Alexa Fluor 647	640 nm	650-760 nm

Table 7. Excitation and emission filters used for fixed cell imaging in first version of Cell Painting of hiPSC-CMs.

2.6.3 Cell Painting protocol 2: Characterizing mitochondria, sarcomere, membrane, and nucleus morphology in the same cells

Once hiPSC-CMs were stained with MitoTracker Deep Red, Hoechst, and WGA-488 and images were acquired in live cells, the cells were rinsed twice with KREBS without calcium before fixation with 2% paraformaldehyde at RT for 10 minutes. Permeabilization and immunofluorescent staining protocol was then performed as described in section *2.6.2* with the one modification that goat anti-mouse IgG Alexa Fluor 555 secondary antibody (1:1000, ThermoFisher, A-21422) was used instead of rabbit anti-mouse IgG Alexa Fluor 647 secondary antibody to mark sarcomeres. See **Table 8** for excitation and emission filters used.

Dye	Excitation filter	Emission filter
Hoechst nucleic acid stain	375 nm	435-480 nm
Wheat Germ Agglutinin - Alexa Fluor 488	488 nm	500-530 nm
MitoTracker Deep Red	640 nm	650-760 nm
Goat anti-mouse IgG Alexa Fluor 555	561 nm	570-630 nm

Table 8. Excitation and emission filters used for second version of Cell Painting protocol. This version multiplexed four dyes/antibodies in four different channels, enabling us to characterize nucleus, membrane, mitochondria, and sarcomere morphology in the same hiPSC-CMs.

2.7 Image analysis

2.7.1 hiPSC-CM segmentation

hiPSC-CM segmentation was achieved using the Columbus software (Revvity, previously Perkin Elmer) and its analysis building blocks. Briefly, the first step was to filter the input image based on either the Alexa Fluor 647, Alexa Fluor 555, or MitoTracker Deep Red channel using Gaussian smoothing at 10 px width to act as a cytosolic marker. Then, we identified nuclei with the "find nuclei" block and from this, identified an initial cytoplasm around each of the nuclei using "find cytoplasm". The cytoplasm population was then modified using "modify population" and clustered by a distance of 3 μm to group nuclei of bi- or multi-nucleated cells together as part of the same cell. Then we used "find surrounding region" to identify the surrounding region of the grouped nuclei and identify the cytoplasm and cell membrane. We then used "select population" to remove cells touching the image border, cells that had areas < 400 μm^2, and cells that had sarcomere SER Edge texture values < 0.04 to eliminate partially imaged cells, debris, and fibroblasts, respectively, from the population prior to analysis of hiPSC-CM morphology.

2.7.2 Calculating hiPSC-CM and nuclei morphology properties

Following image segmentation, we calculated morphological properties of hiPSC-CMs and nuclei which were cell area, cell roundness, cell length, cell width, cell witdth:length ratio, nucleus area, and nucleus roundness using the Columbus software and selecting the building block "calculate morphology properties". The protocol to determine the number of mono-, bi-, and multi-

nucleated cells was modified from the analysis pipeline by Mosqueira *et al*. [70] which involved counting the number of initial nuclei found in the final grouped nuclei region of each cell.

2.7.3 Characterizing sarcomere organization

Following hiPSC-CM segmentation, sarcomere organization analysis was modified from the protocol by Mosqueira *et al*. [70] and from Cara Hawey's thesis, "Understanding dilated cardiomyopathy using cardiomyocytes made from patient-derived induced pluripotent stem cells" submitted in July 2022 to McGill University. Briefly, the Columbus analysis software was trained, using Haralick's texture features, to recognize four levels of sarcomere organization, ranging from highly aligned sarcomeres to punctate, or disorganized sarcomeres (**Figure 4**). The Columbus software was then able to sort hiPSC-CMs into their sarcomere organization category based on the training set provided and present a number and percentage of hiPSC-CMs that were sorted into each level of organization.

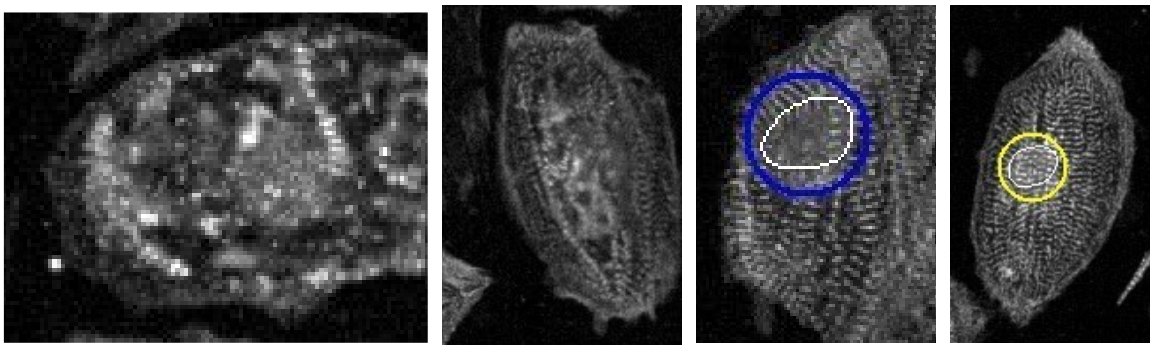

Figure 4. Examples of highly disorganized, disorganized, organized, and highly organized hiPSC-CMs used for training the Columbus software to recognize levels of sarcomere organization. At least 100 cells from each level of organization were used in the training set.

2.7.4. Characterizing mitochondria morphology

Percentage of mitochondria area was calculated by using the "find image region" block to identify the image region corresponding to mitochondria based on the MitoTracker Deep Red channel. Selecting "calculate morphology properties" and selecting "area" for the mitochondria image region calculated the area of the mitochondria region. Then, by selecting the "calculate properties" block, Columbus calculated the mitochondria image region area divided by the entire hiPSC-CM cell area to output the percentage of the cell occupied by mitochondria staining.

Mitochondria distribution was represented by the number of cells that had mitochondria distributed more closely around the nucleus versus along sarcomeres (**Figure 5**). Following hiPSC-CM segmentation, the Columbus software sorted hiPSC-CMs into their mitochondria distribution category by selecting the "select population" building block followed by the selection of the "linear classifier" method. The linear classifier method involved providing Columbus with a training set of at least 100 sample hiPSC-CMs from each category to train it to recognize and sort hiPSC-CMs based on mitochondria distribution. The number of cells in each category was the output.

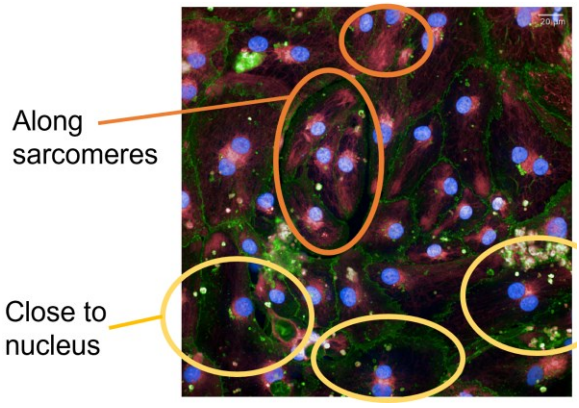

Figure 5. Examples of hiPSC-CMs with mitochondria distribution close to the nucleus versus along sarcomeres used in training set provided to Columbus software to categorize cells based on mitochondrial distribution.

3.0 RESULTS

3.1 Characterizing morphological features of hiPSC-CMs

As previously mentioned, genotype-phenotype associations in DCM remain poorly understood. In this thesis, I optimized a protocol to simultaneously evaluate cellular, nuclear, mitochondrial, and sarcomere morphology of hiPSC-CMs at the single cell level and in the context of DCM. The goal was to characterize cellular morphology phenotypes in DCM hiPSC-CMs to ultimately form phenotypic groups within our patient cohort that could be linked to the disease. To our knowledge, we are the first to do so and at the very least, methods developed in this thesis are new to the Hébert lab.

3.1.1 Troubleshooting methods to characterize hiPSC-CM morphology

Our current workflow is based on the Cell Painting protocol by Bray *et al.* [134], however, many modifications had to be made to properly visualize the ultrastructure of hiPSC-CMs. We tested various dyes, kits, and antibodies in different combinations (**Figure 6**) before arriving at our optimized workflow.

The first dye kit that we tested was the Perkin Elmer Cell Painting Kit because it was optimized for Cell Painting purposes and was accompanied by a validated protocol [135]. The objective was to characterize as many morphological parameters as possible and compare differences between patient hiPSC-CM lines using an automated analysis software to avoid bias. The kit was comprised of the following dyes: a mitochondrial dye, a nuclear dye, a nucleic acid stain, an endoplasmic reticulum (ER) dye, a cell membrane dye, and a cytoskeleton (actin) dye.

However, we encountered several issues with this kit. First, the ER dye and nucleic acid stain as well as the actin dye and the cell membrane dye had spectral overlap. This prevented the software from distinguishing between the individual structures during image analysis. Secondly, the membrane dye penetrated the whole cell and failed to accurately mark cell membranes which made it challenging to segment individual hiPSC-CMs from each other. Furthermore, the mitochondrial stain failed to reveal mitochondrial networks (**Figure 6A**). To address these issues, we decided that next steps would involve removing dyes for the ER, actin, and nucleic acid as there was little to no evidence that these structures were disrupted in DCM. Instead, we chose to introduce a sarcomere marker, an anti-α-actinin antibody, as sarcomere morphology was commonly reported to be disrupted in DCM. Next steps also included the optimization of staining conditions of the membrane marker, WGA-555, and the mitochondrial stain, MitoTracker Deep Red.

To optimize the mitochondrial stain, MitoTracker Deep Red, cells were incubated with different concentrations ranging from 100 nM – 500 nM of MitoTracker Deep Red for 30 minutes before fixing and imaging cells as recommended by the manufacturer's manual. The mitochondrial stain was blurry and oversaturated in all conditions and unexpectedly, many CMs had no stained mitochondria (**Figure 6B**). Following this, we incubated cells for 30 minutes with a lower concentration of MitoTracker Deep Red (50 nM) and imaged live cells rather than fixed cells which yielded clear mitochondrial networks (**Figure 6C**). Following the successful optimization of the mitochondrial dye, we realized that we would not be able to simultaneously image all dyes of interest because the sarcomere marker required fixation prior to staining. As a solution, we decided that for each plate, we would image on live cells prior to fixation, followed by a second imaging step on fixed cells.

To optimize the membrane stain, we incubated cells with different concentrations of WGA-555 ranging from 1-10 μg/mL, as recommended by the manufacturer's manual, both pre- or post-fixation. All of these conditions resulted in WGA-555 staining the whole cell rather than just the membrane, making it difficult for hiPSC-CM segmentation (**Figure 6D**). We were then recommended by a collaborator to incubate cells with 5 μg/mL WGA-488 for 10 minutes prior to imaging in live cells or fixation. Results showed distinct membranes that clearly separated individual hiPSC-CMs from each other in monolayers (**Figure 6E**). We observed that WGA-488 was gradually internalized by the cell and stained structures inside the cell within 1 hour from incubation. To avoid internalization, we decided that incubation with WGA-488 must directly precede imaging to minimize the time between incubation and image acquisition.

Once WGA-488 and MitoTracker Deep Red protocols were optimized, we observed that during live imaging following MitoTracker Deep Red and WGA-488 incubation, acquired images were blurry and focal points were challenging to determine because hiPSC-CMs were beating too much during image acquisition. To circumvent this issue, we incubated cells in KREBS without calcium. Calcium is crucial to cardiac contractility [136] and so removing it from the buffer solution slowed hiPSC-CM beating and resulted in clearer images.

Finally, once dyes were optimized, we analyzed the images using the automated analysis software, Columbus, to measure various morphological parameters. However, despite WGA-488 clearly marking cell membranes, the software was unable to properly segment hiPSC-CMs in monolayers. We were then recommended to include a cytosolic marker in addition to a membrane marker as the combination of both would facilitate hiPSC-CM segmentation during image analysis.

Therefore, we incubated cells with both DRAQ5 as a cytosolic marker and WGA-488 as a membrane marker. This combination of dyes enabled Columbus to properly segment individual hiPSC-CMs when grown in monolayers during image analysis (**Figure 6F**). However, we then realized that DRAQ5 and MitoTracker Deep Red had spectral overlap which would prevent us from using both simultaneously as we would not be able to distinguish signals. To address this issue, we removed DRAQ5 from our protocol and instead used image analysis tools in Columbus to filter and blur the MitoTracker Deep Red or sarcomere channels to serve as a surrogate for a cytosolic marker. This method yielded successful segmentation results.

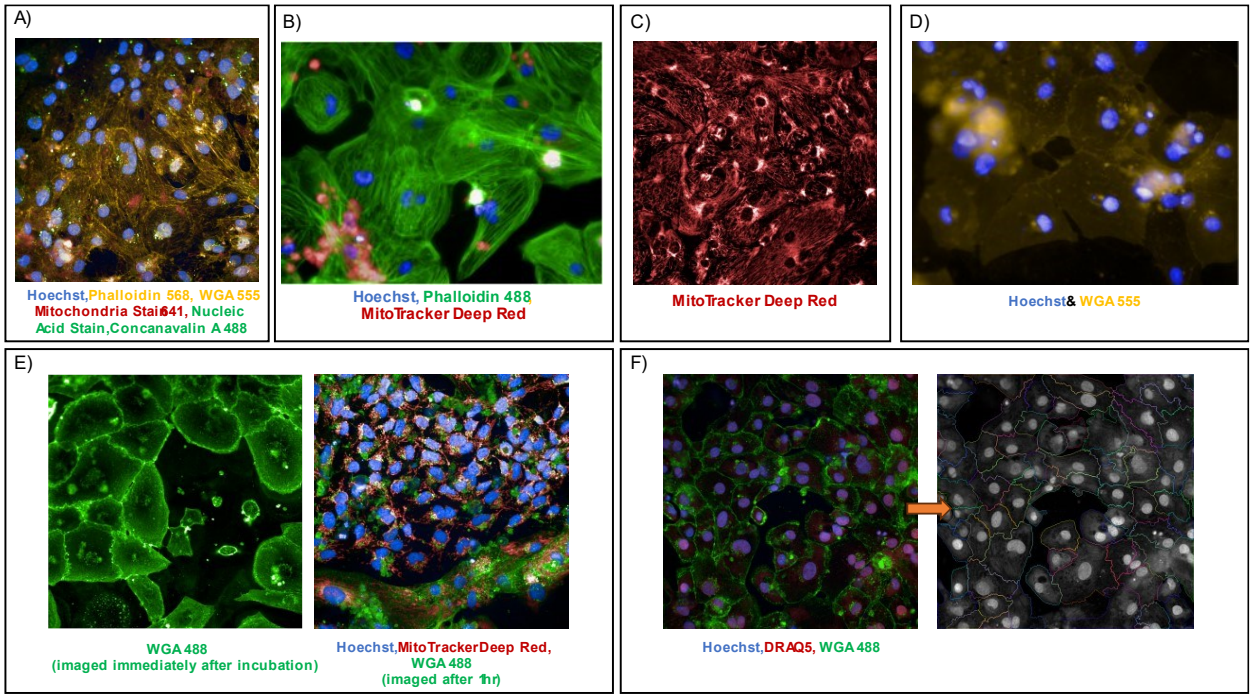

Figure 6. Testing different methods to characterize hiPSC-CM morphology. A) Perkin Elmer Cell Painting Kit image results. Dyes were Hoechst (nucleus), Phalloidin (actin filaments), WGA (cell membrane), Mitochondria stain, Nucleic acid stain, Concanavalin A (endoplasmic reticulum). **B)** hiPSC-CMs stained with 300 nM MitoTracker Deep Red, 165 nM Phalloidin-Alexa Fluor 488, and 1 µg/mL Hoechst. **C)** hiPSC-CMs stained with 50 nM MitoTracker Deep Red and imaged in live cells. **D)** hiPSC-CMs stained with 5 µg/mL WGA-555 and 1 µg/mL Hoechst and imaged as fixed cells. **E)** **Left:** hiPSC-CMs stained with 5 µg/mL WGA-488 and imaged immediately after incubation in live cells. **Right:** hiPSC-CMs stained with 5 µg/mL WGA-488, 1 µg/mL Hoechst, and 50 nM MitoTracker Deep Red and imaged about 1 hour after incubation in live cells resulting

in WGA-488 being internalized. **F)** 5 μM DRAQ5 as a cytosolic marker enabling image segmentation of individual hiPSC-CMs. Cells were also incubated with 1 μg/mL Hoechst and 5 μg/mL WGA-488 in live cells.

3.1.2 Optimized workflow to characterize hiPSC-CM morphology: Cell Painting protocol 1

After various troubleshooting experiments, we determined that the most suitable method for our research interests involved characterizing aspects of mitochondria morphology separately from characterizing overall hiPSC-CM morphology and sarcomere organization.

As the 1st version of our Cell Painting protocol, in one 96-well plate of hiPSC-CMs, cells were live stained with MitoTracker Deep Red, WGA-488, and Hoechst before live cell imaging to visualize mitochondria, the cell membrane, and the nucleus. In a separate 96-well plate of hiPSC-CMs, cells were live stained with WGA-488 and Hoechst before being fixed and permeabilized prior to incubation with an anti-α-actinin antibody coupled to Alexa Fluor 647 (anti-α-actinin-647). Then, the fixed cells were imaged with a high-content screening system and morphological features were analyzed. For each cell line, at least two separate 96-well plates of hiPSC-CMs were needed as MitoTracker Deep Red and anti-α-actinin-647 have spectral overlap.

3.1.3 Cell segmentation for characterizing hiPSC-CM morphology

CMs exist as syncytium *in vivo [137]*. Thus, i*n vitro*, hiPSC-CMs grow in monolayers or clusters, which can present a challenge to hiPSC-CM segmentation. Cell segmentation during image analysis relied on WGA-488 as a membrane marker and image analysis tools to blur the sarcomere or mitochondria channels to serve as a cytosolic marker. Even in confluent monolayers

or clusters, individual hiPSC-CMs can, up to a certain extent, be distinguished and recognized by the Columbus analysis software using this method **(Figure 7)**.

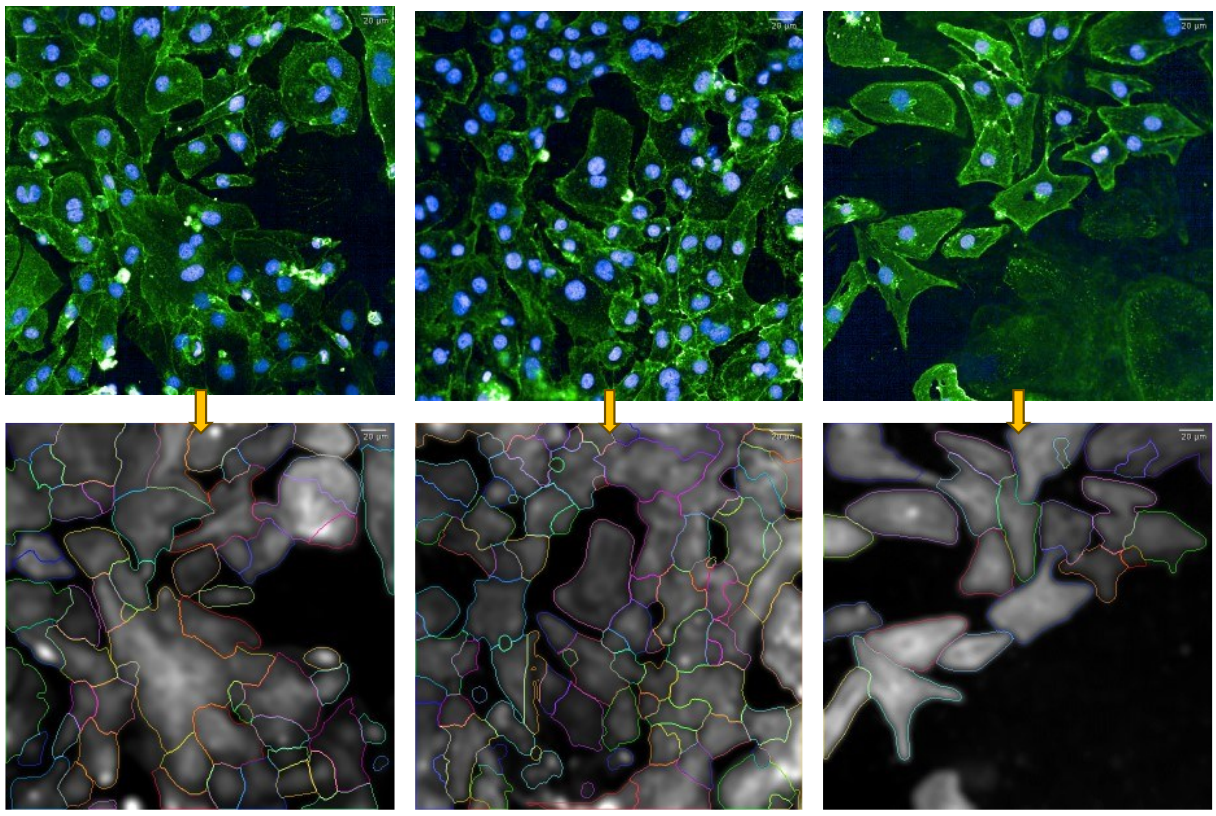

Figure 7. hiPSC-CM segmentation in Columbus analysis software. WGA 488 (green) acts as a cellular membrane marker and a filtered image of the mitochondria or sarcomere channel (not shown) serves as a cytosolic marker to help the Columbus software segment the image into individual hiPSC-CMs.

3.1.4 Characterizing aspects of mitochondria distribution and localization in hiPSC-CMs

Two morphological features of mitochondria that our "Cell Painting" workflow was developed to characterize were 1) mitochondria distribution within hiPSC-CMs and 2) the percentage area of the cell occupied by mitochondria (% mitochondria area). These morphological parameters were prioritized because the distribution of mitochondria within hiPSC-CMs [83] and

the percentage area, as a reflection of the amount of mitochondria within hiPSC-CMs [73], may reflect the disease and maturity status of patient-derived hiPSC-CM lines.

Mitochondria distribution was measured as a proportion of hiPSC-CMs that had mitochondria either mostly surrounding the nucleus or along sarcomeres **(Figure 8).** The Columbus analysis software was trained with sample images to categorize cells into either of the two categories. The Columbus software was also able to calculate % mitochondria area.

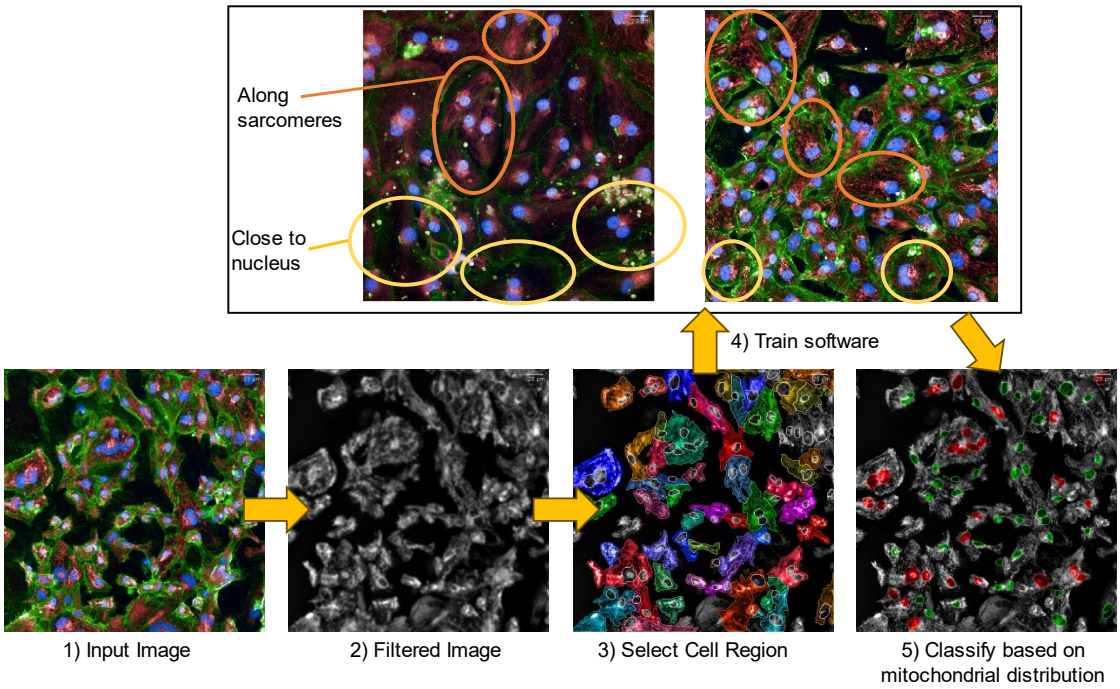

Figure 8. Analysis workflow to characterize mitochondria distribution WGA-488 (green) marks cell membranes, MitoTracker Deep Red (red) marks mitochondria, and Hoechst (blue) marks the nucleus. Analysis performed in Columbus analysis software.

We compared % mitochondria area and mitochondria distribution between three hiPSC-CM lines: AIW002-02 control subject, HID04C control subject, and HID041020 DCM patient (**Figure 9**). Preliminary results reveal differences in both morphological endpoints. AIW002-02

control hiPSC-CMs had a higher proportion of cells with mitochondria distributed around the nucleus (66%) compared to HID04C control hiPSC-CMs and HID041020 DCM hiPSC-CMs which had 42% and 41% of cells with mitochondria concentrated around the nucleus, respectively (n=1) (**Figure 9A**). As for % mitochondria area, HID04C control hiPSC-CMs had a significantly greater mean % mitochondria area (57%) compared to AIW002-02 control and HID041020 DCM hiPSC-CMs that had mean % mitochondria areas of 46% and 50%, respectively (n=1) (**Figure 9B**). However, with only a single experiment for each endpoint and a different number of cells in each hiPSC-CM group, it is difficult to say whether these statistically significant differences are due to the large sample size of each group and the differences in sample size between each group, or if they reflect biologically relevant inter-patient differences or differences in hiPSC-CM maturity. This is further discussed in the Discussion section.

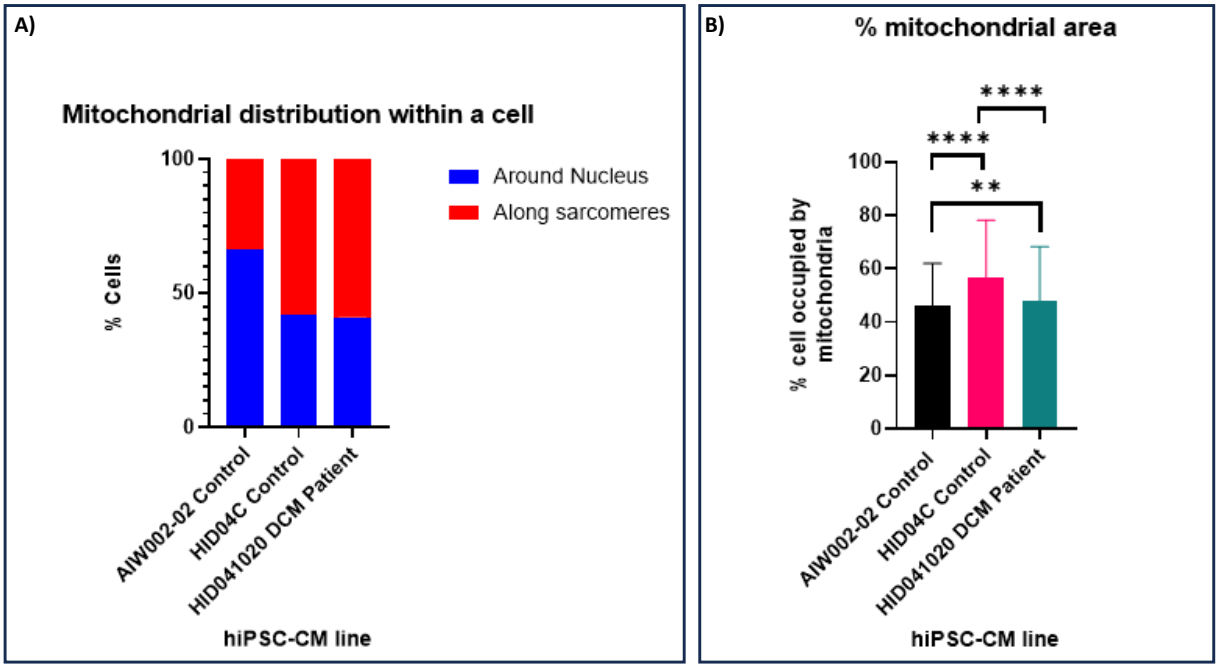

Figure 9. Comparison of mitochondrial distribution within a cell and percentage of mitochondrial area between different hiPSC-CM lines. A) Proportion of AIW002-02 control (n=32,969 cells), HID04C control (n=1,414 cells), and HID041020 DCM (n=4,001 cells) hiPSC-CMs that have mitochondria mostly distributed around the nucleus compared to mitochondria

mainly distributed along sarcomeres (n=1 biological replicates). **B)** Mean percentage area of AIW002-02 control (n=32,969 cells), HID04C control (n=1,414 cells), and HID041020 DCM (n=4,001 cells) hiPSC-CMs occupied by mitochondria (n=1 biological replicate). **p=0.0013 and ****p<0.0001. Unpaired t-tests were performed. SD bars are shown.

3.1.5 Characterizing differences in hiPSC-CM and nucleus morphology

We characterized differences in nucleus roundness, nucleus area, cell area, cell roundness, cell length, cell width, cell width:length ratio, and the number of mono-, bi-, and multi-nucleated cells between HID041020 DCM hiPSC-CMs and AIW002-02 control hiPSC-CMs. Unpaired t-tests were performed on a single set of CMs in each group (11,755 cells in AIW002-02 group and 2,455 cells in HID041020 group) that revealed HID041020 DCM hiPSC-CMs had significantly greater mean nucleus roundness ($t=19.08$, $p<0.0001$), nucleus area ($t=4.122$, $p<0.0001$), cell area ($t=2.079$, $p=0.0376$), and cell width ($t=3.764$, $p=0.0002$) compared to AIW002-02 control hiPSC-CMs (**Figure 10A, B, C, F**). In contrast, HID041020 DCM hiPSC-CMs had significantly decreased cell roundness ($t=16.84$, $p<0.0001$), cell length ($t=8.515$, $p<0.0001$), and cell width:length ratio ($t=6.847$, $p<0.0001$) compared to AIW002-02 control hiPSC-CMs (**Figure 10D, E, G**). Interestingly, AIW002-02 control hiPSC-CMs had a higher proportion of cells with binucleated (10%) and multinucleated cells (1%) compared to HID041020 DCM hiPSC-CMs (4% binucleated and 0% multinucleated) (**Figure 10H**). However, the statistical significance is likely due to the large number of cells in each group and the difference in sample size between both groups as this is only a single experiment. This is further discussed in the Discussion.

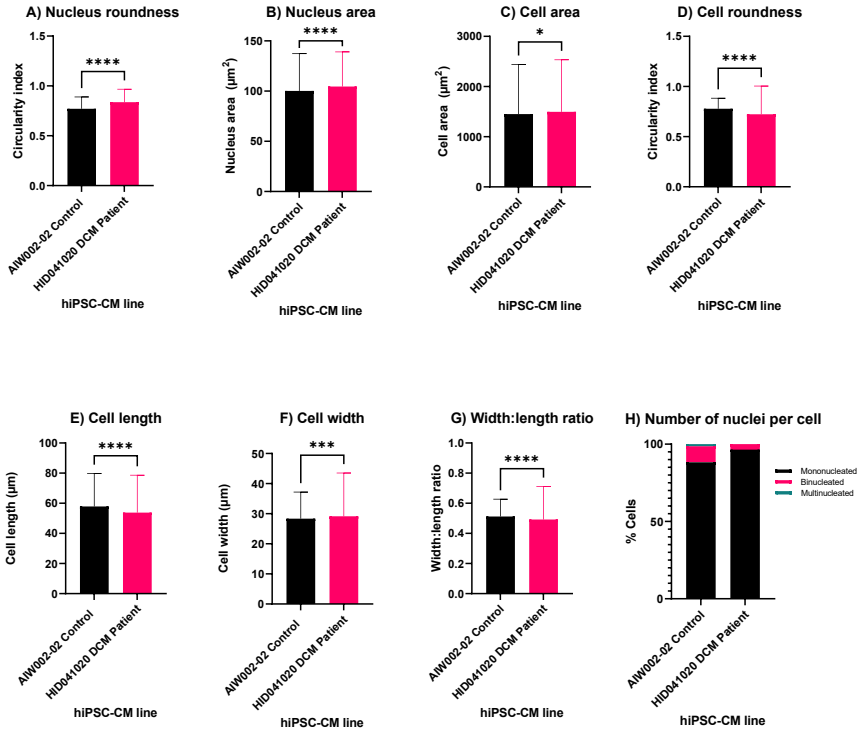

Figure 10. Preliminary analyses of cellular morphology in HID041020 DCM and AIW002-02 control hiPSC-CMs. Preliminary results obtained from Columbus image analysis software. Morphological features compared were **A)** nucleus roundness ($mean_{control}$: 0.7702 vs $mean_{DCM}$: 0.8370, t=19.08), **B)** nucleus area ($mean_{control}$: 100.2 µm^2 vs $mean_{DCM}$: 104.5 µm^2, t=19.08), **C)** cell area ($mean_{control}$: 1452 µm^2 vs $mean_{DCM}$: 1497 µm^2, t=2.079), **D)** cell roundness ($mean_{control}$: 0.7776 vs $mean_{DCM}$: 0.7228, t=16.84), **E)** cell length ($mean_{control}$: 57.91 µm vs $mean_{DCM}$: 53.82 µm, t=8.515), **F)** cell width ($mean_{control}$: 28.34 µm vs $mean_{DCM}$: 29.15 µm, t=3.764), **G)** cell width:length ratio ($mean_{control}$: 0.5123 vs $mean_{DCM}$: 0.4918, t=6.847), and **H)** proportion of mono-, bi-, and multi-nucleated cells. 11,755 cells in AIW002-02 group and 2,455 cells in HID041020 group. *: p<0.05, ***: p<0.0005, ****: p<0.0001. SD bars are shown.

3.1.6 Characterizing sarcomere organization

We trained the Columbus image analysis software to recognize and categorize hiPSC-CMs into four levels of sarcomere organization: highly disorganized, disorganized, organized, and highly organized (**Figure 11**). We compared sarcomere organization between AIW002-02 control hiPSC-CMs and HID041020 DCM hiPSC-CMs and we observed that HID041020 DCM hiPSC-

CMs had a higher proportion of cells with disorganized or highly disorganized sarcomeres (62.5%) compared to AIW002-02 control hiPSC-CMs (40.9%) (**Figure 12**). Although this may indicate that increased sarcomere disorganization, a feature of DCM in hiPSC-CMs, is recapitulated in the HID041020 DCM hiPSC-CMs compared to the AIW002-02 control hiPSC-CMs, these differences may be attributed to the difference in the number of cells in each group as this was a single experiment with 11,775 cells in the AIW002-02 group and 2,455 cells in the HID041020 group.

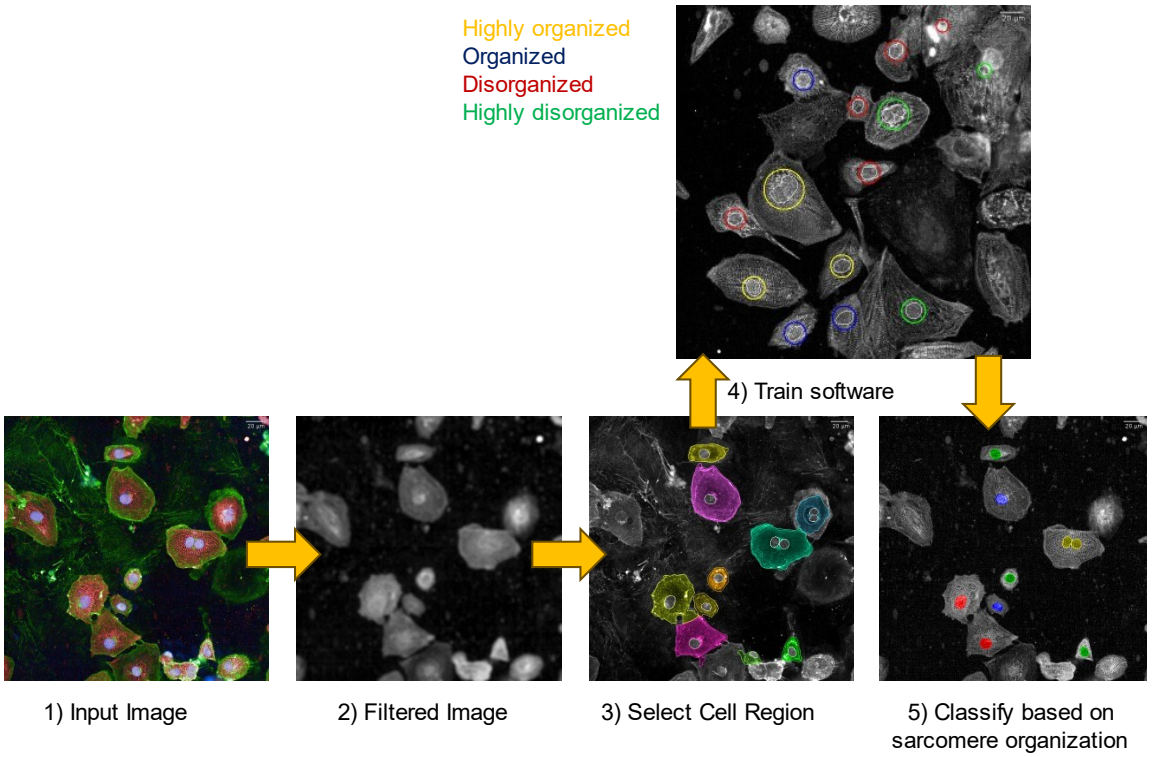

Figure 11. Image analysis pipeline to characterize sarcomere organization in hiPSC-CMs.

A)

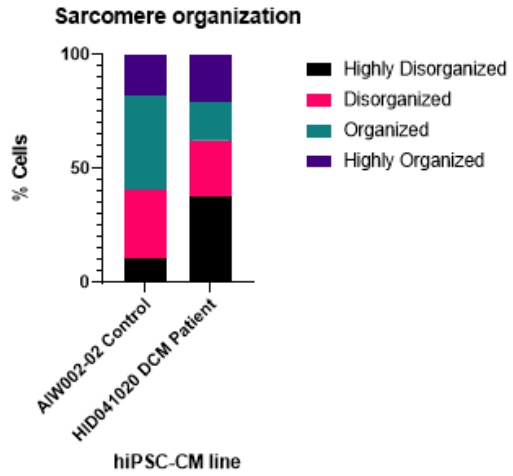

B)

	Highly Disorganized (%)	Disorganized (%)	Organized (%)	Highly Organized (%)
AIW002-02 Control	10.8%	30.1%	41.1%	18.0%
HID041020 DCM Patient	37.9%	24.6%	16.9%	20.6%

Figure 12. HID041020 DCM hiPCS-CMs have a higher proportion of cells with highly disorganized or disorganized sarcomeres compared to AIW002-02 control hiPSC-CMs. A) Stacked bar graphs to visualize the observation. **B)** Percentages of highly disorganized, disorganized, organized, and highly organized AIW002-02 or HID041020 hiPSC-CMs. N=1 biological replicate. 11,775 cells in AIW002-02 group and 2,455 cells in HID041020 group.

3.1.7 Cell Painting protocol 2: Characterizing mitochondria, cell morphology, and sarcomere organization in the same cells

A limitation of the 1st version of the Cell Painting protocol was that we had to assess mitochondria morphology separately from other morphological features, hindering us from extracting morphological features of interest from the same cells. To work around this, we replaced the secondary antibody, Alexa Fluor 647, targeting the anti-α-actinin primary antibody, with the Alexa Fluor 555 secondary antibody. This enabled us to measure mitochondrial properties and sarcomere morphology in the same cells because MitoTracker Deep Red and Alexa Fluor 555 did not have spectral overlap. Hence, the 2nd version of this Cell Painting protocol consisted of live staining cells with WGA-488, Hoechst, and MitoTracker Deep Red followed by live cell image acquisition. Then, the same hiPSC-CMs would be fixed, permeabilized, and incubated with anti-α-actinin-Alexa Fluor 555 before image acquisition. (**Figure 13**).

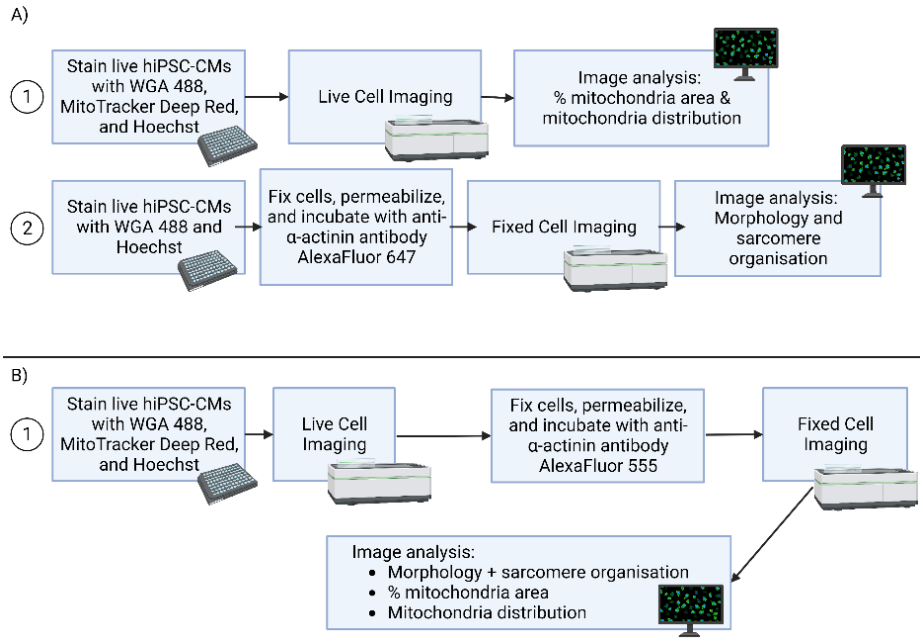

Figure 13. Comparison of 1st and 2nd version Cell Painting protocol. A) 1st version of the protocol required mitochondria and sarcomere morphology to be acquired in different cells. **B)** 2nd version of the protocol evaluates mitochondria, sarcomere, and cell morphology in the same cells.

In **Figures 10 and 12**, we characterized cell and sarcomere morphology of AIW002-02 hiPSC-CMs from the right half of the 96-well plate using the 1st version of the Cell Painting protocol. The remaining left half of the plate was used for testing the 2nd version of the Cell Painting protocol. In this experiment, confocal images revealed cells with defined sarcomere structures (**Figure 14A**) whereas other cells displayed inconsistent sarcomere immunostaining (**Figure 14B-C**). Anti-α-actinin-555 was also found to accumulate in cell debris rather than in hiPSC-CMs (**Figure 14D**). Analysis of sarcomere organization from these images revealed that only 0.6% of the AIW002-02 hiPSC-CMs had highly organized sarcomeres and that 70% had disorganized sarcomeres. This was a contrast to the 18% of AIW002-02 hiPSC-CMs from the 1st version of the Cell Painting protocol that had highly organized sarcomeres and 30% disorganized sarcomeres (**Figure 15**).

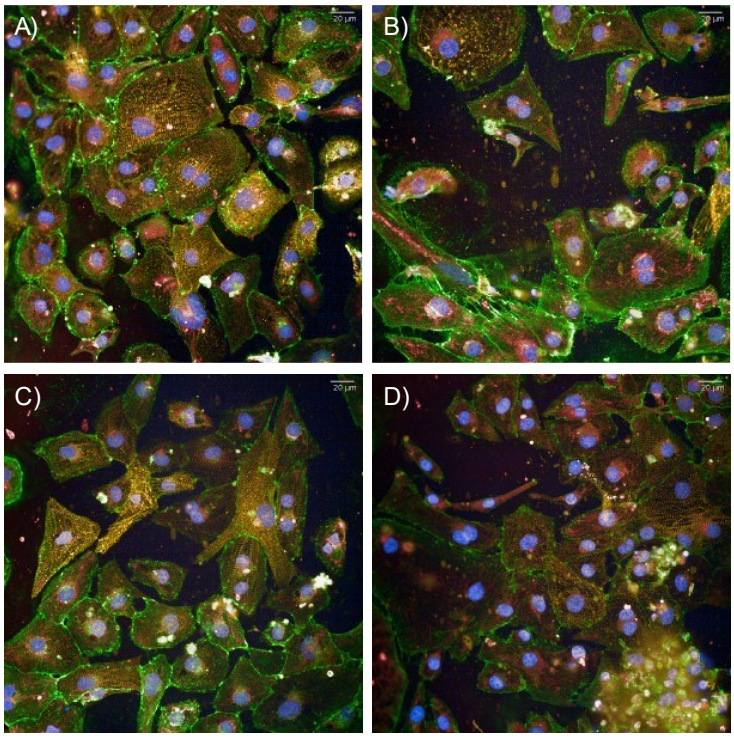

Figure 14. A-D) Examples of inconsistent immunostaining of sarcomeres using anti-α-actinin Alexa Fluor 555. AIW002-02 control hiPSC-CMs are pictured. WGA 488 (green) marks cell membranes, anti-α-actinin Alexa Fluor 555 (yellow) marks sarcomeres, Hoechst (blue) marks nuclei, and MitoTracker Deep Red (red) marks mitochondria.

A) Sarcomere organization

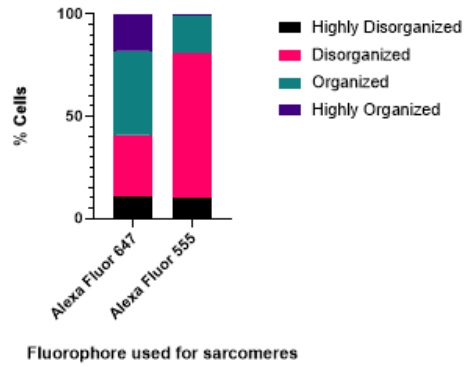

B)

	Highly Disorganized (%)	Disorganized (%)	Organized (%)	Highly Organized (%)
AIW002-02 Control (Alexa Fluor 647)	10.8	30.1	41.1	18.0
AIW002-02 Control (Alexa Fluor 555)	10.1	70.7	18.6	0.6

Figure 15. Differences in sarcomere organization when immunostaining sarcomeres with anti-α-actinin Alexa Fluor 647 versus anti-α-actinin Alexa Fluor 555. A) Stacked bar graphs of sarcomere organization based on secondary antibody used to mark sarcomeres. **B)** Proportion of hiPSC-CMs with highly disorganized, disorganized, organized, and highly organized sarcomeres when immunostaining sarcomeres with anti-α-actinin Alexa Fluor 647 and anti-α-actinin Alexa Fluor 555. hiPSC-CMs were derived from the AIW002-02 control patient. N=1 with 11,775 cells in the Alexa Fluor 647 group and 6,730 cells in the Alexa Fluor 555 group.

Finally, we compared cellular morphology features of AIW002-02 control hiPSC-CMs from the two different versions of the Cell Painting protocol. AIW002-02 cells incubated with anti-α-actinin Alexa Fluor 555 had significantly greater mean nucleus area, nucleus roundness, and cell length (**Figure 16A, B, E**) as well as significantly decreased mean cell area, width, roundness, and width:length ratios (**Figure 16C, D, F, G)** compared to AIW002-02 cells incubated with anti-α-actinin Alexa Fluor 647**.** However, the proportion of mono-, bi-, and multi-nucleated cells were very similar in both conditions. AIW002-02 cells incubated with Alexa Fluor 647 had 88.3% mononucleated, 10.3% binucleated, and 1.4% multinucleated cells. Similarly, AIW002-02 cells incubated with Alexa Fluor 555 had 87.7% mononucleated, 10.6% binucleated, and 1.7% multinucleated cells (**Figure 16H**). It must be noted that the statistically significant results are likely due to the large number of cells in each group and the difference in sample sizes between both groups (11,755 cells in Alexa Fluor 647 group and 6,730 cells in Alexa Fluor 555 group).

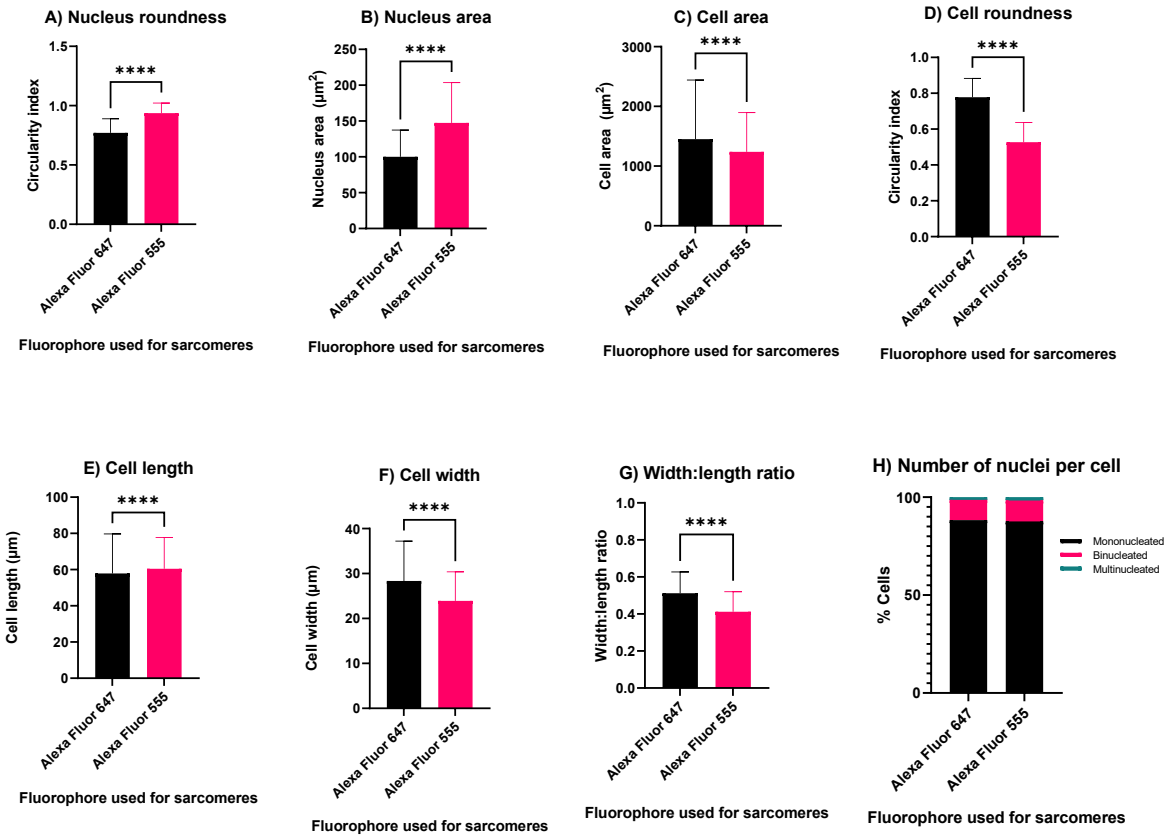

Figure 16. Comparison of morphological features in AIW002-02 control hiPSC-CMs measured using two different Cell Painting protocols. AIW002-02 control hiPSC-CMs were incubated with either anti-α-actinin Alexa Fluor 647 or Alexa Fluor 555. **A)** nucleus roundness ($mean_{647}$: 0.7702 vs $mean_{555}$: 0.9369, t=89.66), **B)** nucleus area ($mean_{647}$: 100.2 µm^2 vs $mean_{555}$: 147.3 µm^2, t=56.08), **C)** cell area ($mean_{647}$: 1452 µm^2 vs $mean_{555}$: 1238 µm^2, t=15.48), **D)** cell roundness ($mean_{647}$: 0.7776 vs $mean_{555}$: 0.5271, t=151.1), **E)** cell length ($mean_{647}$: 57.91 µm vs $mean_{555}$: 60.42 µm, t=7.925), **F)** cell width ($mean_{647}$: 28.34 µm vs $mean_{555}$: 23.91 µm, t=35.02), **G)** cell width:length ratio ($mean_{647}$: 0.5123 vs $mean_{555}$: 0.4123, t=57.21), and **H)** proportion of mono-, bi-, and multi-nucleated cells. n=1 biological replicate with 11,755 cells in Alexa Fluor 647 group and 6,730 cells in Alexa Fluor 555 group. ****: p<0.0001. SD bars are shown.

3.2 Metabolic Maturation of hiPSC-CMs

The immature phenotype of hiPSC-CMs complicates their use in disease modeling. Metabolic maturation medium formulations stand out as one of the more accessible and feasible options to mature hiPSC-CMs *in vitro*. Many of the previously highlighted metabolic maturation

methods consisted of only one or few maturation-inducing reagents tested independently, but some research groups have combined these previously identified maturation-inducing reagents into a single medium formulation to further enhance hiPSC-CM maturity. The goal of these experiments was to test different metabolic maturation protocols to select the optimal protocol to generate a more mature and disease-relevant model to perform our phenotypic assays on. Once established, the plan is to ultimately subject all our hiPSC-CMs to the selected metabolic maturation protocol prior to any phenotypic assay experiments in order to ensure that phenotyping is performed on more disease-relevant hiPSC-CMs that may better recapitulate hallmarks of the disease.

3.2.1 Metabolic maturation with the protocol by Funakoshi et al.

Funakoshi *et al*. reported a metabolic maturation protocol for hiPSC-CM embryoid bodies comprised of a low glucose basal medium supplemented with palmitate, dexamethasone, T3 hormone, and a PPARα agonist for the first 9 days before switching to only palmitic acid in a low glucose medium for the following 5 days [128]. hiPSC-CM embryoid bodies cultured in maturation medium had the ability to use fatty acids as an energy source, a higher mitochondrial mass, organized sarcomere structures, and increased contractility compared to control cells [128]. Given the promising results, we aimed to adapt this protocol for our own hiPSC-CM 2D cultures.

3.2.1.1 Metabolic maturation protocol by Funakoshi et al. results in cell death

Maturation medium (MM) was prepared according to the published protocol with the exception that the palmitate was purchased in complex with BSA from Cayman Chemicals rather than preparing the complex ourselves. Noticeable cell death was observed in the MM-treated

hiPSC-CMs by day 7 of the 15-day protocol, and near complete cell death was observed by day 13. No noticeable hiPSC-CM death was observed in the control hiPSC-CMs maintained in hiPSC-CM maintenance medium, RPMI + B27 (**Figure 17**).

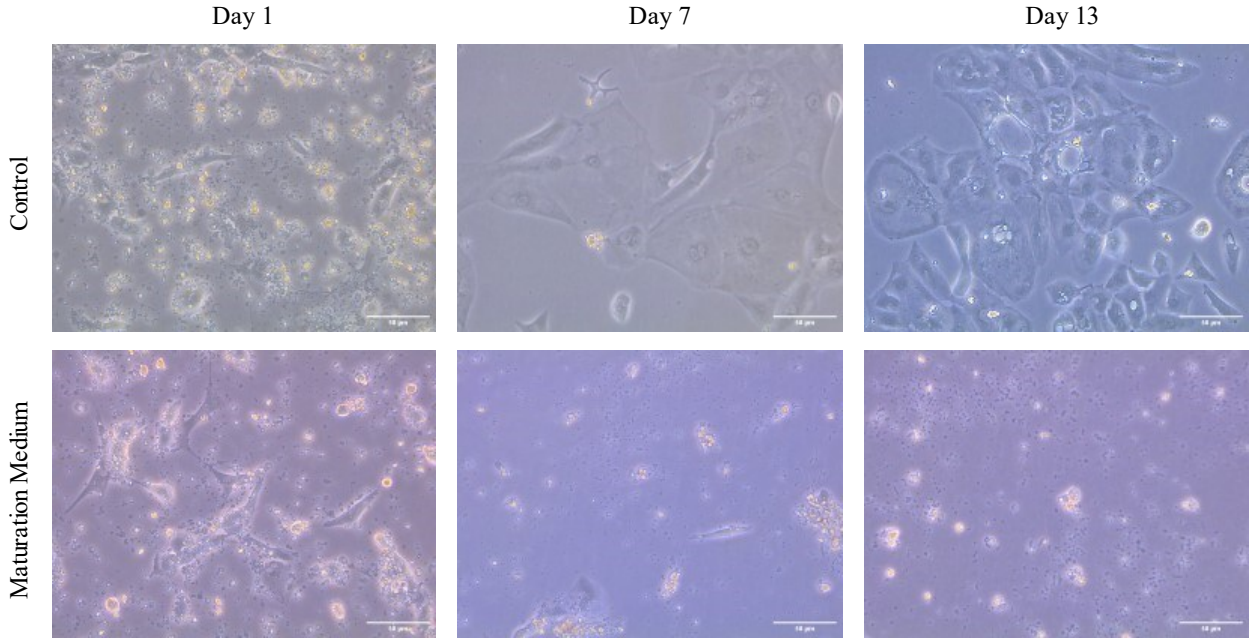

Figure 17. Maturation medium by Funakoshi *et al.* results in hiPSC-CM death by Day 7 of the 15-day protocol. Brightfield images of hiPSC-CMs in control medium or maturation medium taken at Day 1, 7, and 13. Control medium consisted of hiPSC-CM maintenance medium, RPMI + B27. Maturation medium consisted of a low glucose (2 g/L) DMEM basal medium supplemented with 200 µM palmitate, 100 ng/mL dexamethasone, 4 nM T3 hormone, and 1 µM GW7647 (PPARa agonist) for the first 9 days before switching to palmitate and low glucose basal medium only for the remaining 5 days. hiPSC-CMs were derived from the AIW002-02 control patient.

Given that the original protocol was intended for 3D embryoid bodies, modifications may have been required to suit our 2D hiPSC-CM cultures. To determine which MM ingredients needed to be adjusted, we treated hiPSC-CMs with each of the MM ingredients alone. By day 7, 200 µM palmitate treatment resulted in noticeable cell death in contrast to no observable cell death in hiPSC-CMs treated with 100 ng/mL dexamethasone, 4 nM T3 hormone, and 1 µM GW7647 (PPARα agonist) alone (**Figure 18**).

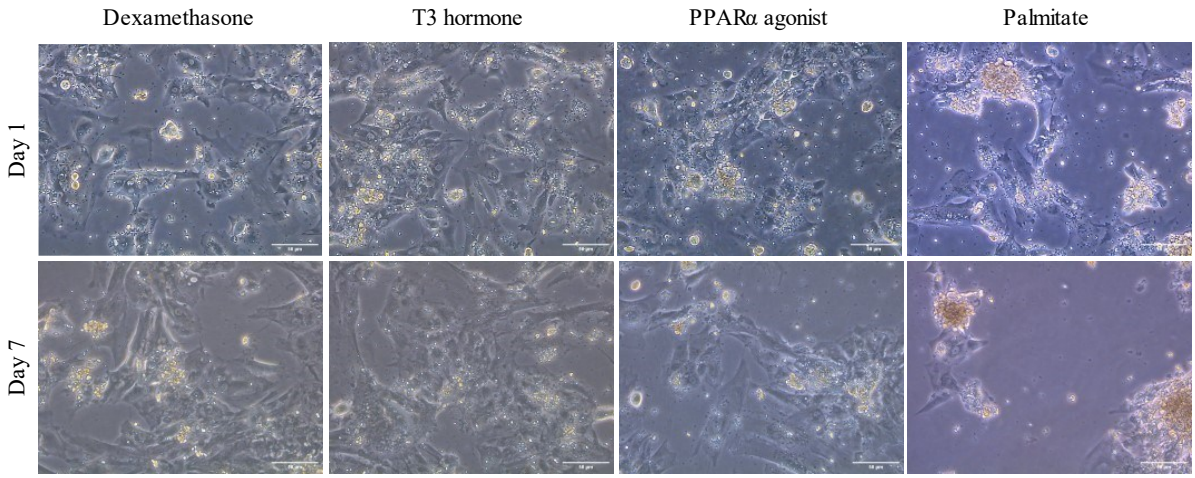

Figure 18. Palmitate alone resulted in hiPSC-CM death by Day 7 in contrast to dexamethasone, T3 hormone, and GW7647 (PPARα agonist) treatments alone. Brightfield images were acquired at day 1 and day 7 of the protocol to evaluate cell death over time in response to either 200 μM palmitate, 100 ng/mL dexamethasone, 4 nM T3 hormone, or 1 μM GW7647 (PPARa agonist). hiPSC-CMs were derived from the AIW002-02 control patient.

It has been documented that long-term exposure or exposure to high concentrations of fatty acids (FAs) in glucose-depleted media can lead to lipotoxicity and cell damage [138]. One study reported that one million hiPSC-CMs could take up to ~57 μM of the provided 231 μM FAs after two days of feeding [94]. These findings suggest that our observed hiPSC-CM death in response to 200 μM palmitate may be due to the long exposure and high concentrations of palmitate provided by the MM by Funakoshi *et al*. Additionally, the original protocol recommended 200 μM palmitate for 3D embryoid bodies in which hiPSC-CMs may experience FA exposure differently than in 2D monolayer cultures. Thus, our next step was to test different concentrations of palmitate.

We tested concentrations of 50 μM, 100 μM, 150 μM, and 200 μM palmitate. A 200 μM concentration of palmitate was used as a control for inducing cell death and control medium (RPMI+B27) was used as a control for ensuring cell survival. We observed that concentrations at and above 100 μM resulted in complete cell death by Day 13 (**Figure 19**).

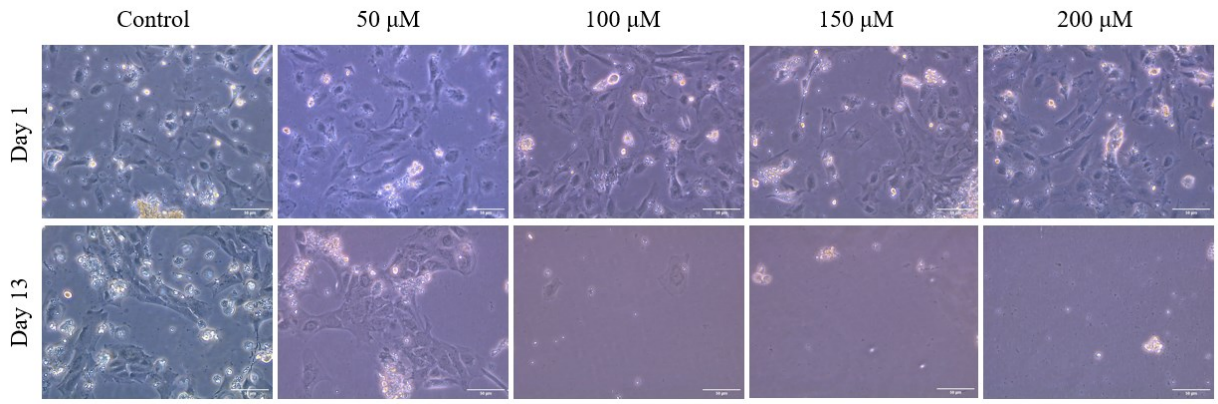

Figure 19. Palmitate concentrations at and above 100 µM resulted in complete hiPSC-CM death. Brightfield images were acquired at Day 1 and Day 13 to evaluate the effect of 50 µM, 100 µM, 150 µM, and 200 µM palmitate concentrations on hiPSC-CM death. hiPSC-CMs were derived from the AIW002-02 control patient.

Seeing as a palmitate concentration of 50 µM supported hiPSC-CM survival and a concentration above 100 µM resulted in cell death, the next step was to test palmitate concentrations below 100 µM to optimize the highest FA concentration sustainable to induce maturity while ensuring hiPSC-CM survival. However, we learned that our collaborators had tested and validated a different metabolic maturation protocol designed for 2D hiPSC-CM cultures by Feyen *et al*. [129]. We decided to switch over to testing the protocol by Feyen *et al*. as it would likely require less optimization than a protocol originally designed for 3D hiPSC-CM cultures.

3.2.2 Metabolic maturation with Feyen et al. protocol

In this procedure, the media formulation was comprised of a low glucose basal medium supplemented with fatty acids, L-lactate, vitamin B12, biotin, creatine monohydrate, taurine, L-carnitine, and non-essential amino acids, improved hallmarks of hiPSC-CM maturity [129]. Cells treated with this maturation media for 3-5 weeks had greater forces of contraction and a heavier

reliance on cardiac sodium channels for triggering action potentials rather than calcium currents compared to control cells. Sarcomere organization, aerobic respiration, and long-term survival were also improved, all of which enabled the authors to reliably model two genetic cardiac diseases following maturation treatment: long QT syndrome type 3 caused by a mutation in the cardiac sodium channel gene, *SCN5A*, and a type of DCM caused by a mutation in *RBM20* [129].

3.2.2.1 Metabolic maturation protocol by Feyen et al. results in longer and more elongated CMs

The MM was prepared according to the published protocol and after 3 weeks, MM-treated hiPSC-CMs had more elongated and rod-shaped phenotypes compared to the small and round-control hiPSC-CMs (**Figure 20**). These observations occurred in two trials of the protocol done in two different hiPSC-CM lines: HID041127 (DCM patient) and AIW002-02 (control patient).

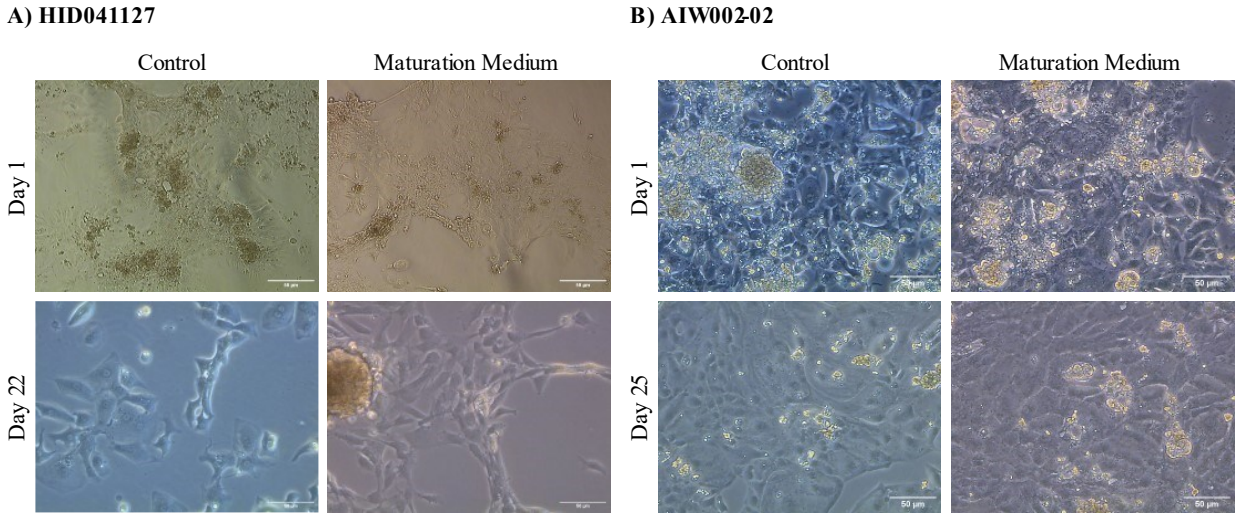

Figure 20. Feyen *et al*. metabolic maturation medium (MM) results in hiPSC-CMs with more elongated and rod-shaped phenotypes. MM-treated hiPSC-CMs demonstrate more elongated and rod-shaped phenotypes compared to round phenotypes in control hiPSC-CMs (RPMI+B27 medium) after 3 weeks (n=1). Images acquired with brightfield microscope. hiPSC-CMs derived from **A)** HID041127 DCM patient and **B)** AIW002-02 control patient.

3.2.2.2 Feyen et al. metabolic maturation protocol induces more mature CM gene expression

As CMs mature, key gene expression changes and isoform switches occur in genes encoding myofibrillar proteins, transcription factors, ion channels, metabolism, and more [89]. A commonly reported isoform switch that occurs during CM maturation is the switch from the fetal isoform (*TNNI1*) to the postnatal isoform (*TNNI3*) of the troponin I subunit [89]. It has also been reported that the gene encoding the transcription factor, *GATA4*, is highly expressed in fetal and neonatal CMs, but is expressed at low levels in adult CMs [139]. *GATA4* regulates the transcription of various cardiac genes such as those responsible for CM proliferation [140]. The transcription factor *NKX2.5* is crucial to mesoderm and CM differentiation during early embryonic development and is present in immature CMs, but expression decreases as CMs mature [141].

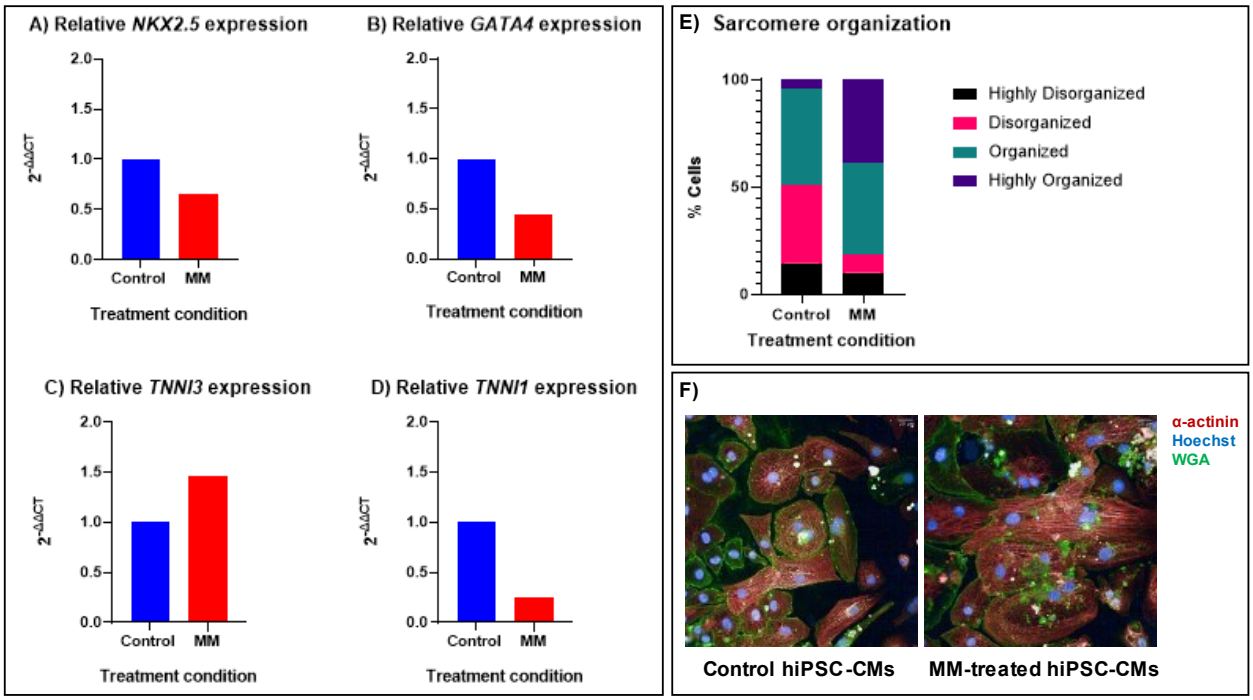

Figure 21. Validation of enhanced maturity in hiPSC-CMs following Feyen *et al.* metabolic maturation protocol. A-D) qPCR results comparing fold change in gene expression of **(A)** *NKX2.5*, **(B)** *GATA4*, **(C)** *TNNI3*, and **(D)** *TNNI1*, normalized to *GADPH* between MM-treated

hiPSC-CMs and control medium-treated hiPSC-CMs after 3 weeks. hiPSC-CMs were derived from the HID041127 DCM patient. **E)** Comparison of the proportion of MM-treated hiPSC-CMs and control hiPSC-CMs with highly disorganized, disorganized, organized, or highly organized sarcomeres as an indicator of maturity. hiPSC-CMs were derived from AIW002-02 control patient. n=1 with 2,498 MM-treated hiPSC-CMs and 6,854 control hiPSC-CMs. **F)** Sample confocal images of control (**left**) and MM-treated (**right**) hiPSC-CMs after immunofluorescent staining with anti-α-actinin Alexa Fluor 647 (sarcomeres, red), Hoechst dye (nucleus, blue), and wheat germ agglutinin dye (cell membrane, green). hiPSC-CMs were derived from AIW002-02 control patient.

To validate enhanced maturity after 3 weeks, changes in the expression of *TNNI1, TNNI3, GATA4,* and *NKX2.5* were measured using qPCR (**Figure 21A-D**). An expected decrease in *TNNI1, GATA4,* and *NKX2.5* expression normalized to housekeeping gene, *GAPDH*, was observed in MM-treated hiPSC-CMs compared to control hiPSC-CMs. An expected increase in *TNNI3* expression was also observed in MM-treated hiPSC-CMs compared to control hiPSC-CMs. Therefore, hallmarks of mature CM gene expression were observed following MM treatment. However, further validation and replicates are necessary to confirm results.

3.2.2.3 The second metabolic maturation protocol improves hiPSC-CM sarcomere organization

Next, we evaluated the extent to which this metabolic maturation protocol improved sarcomere organization as it is a hallmark of mature CMs in contrast to immature CMs that exhibit poorly aligned sarcomeres. Using our Cell Painting protocol and analysis workflow, we observed that MM-treated hiPSC-CMs had a higher proportion of cells with highly organized sarcomeres (39%) compared to control hiPSC-CMs maintained in RPMI+B27 medium (4%) (**Figure 21E**). We also observed that there was a lower proportion of MM-treated hiPSC-CMs with highly disorganized (10%) and disorganized (8%) sarcomeres compared to control hiPSC-CMs (15% highly disorganized and 37% disorganized) (**Table 9 and Figure 21E**). Confocal images of control

and MM-treated hiPSC-CMs also reveal that MM-treated hiPSC-CMs tend to be larger and more rod-shaped with more aligned sarcomeres compared to control hiPSC-CMs, exhibiting hallmarks of more mature CMs (**Figure 21F**). Cell Painting morphological analysis of images reveal that mean cell area ($t=32.52$, $p<0.0001$), length ($t=27.29$, $p<0.0001$), and width ($t=35.31$, $p<0.0001$) were significantly greater in MM-treated hiPSC-CMs compared to control hiPSC-CMs using unpaired t-tests (**Figure 22A-C**). As CMs mature, they transition from a mononucleated to binucleated phenotype [142]. However, MM-treated hiPSC-CMs exhibit a lower percentage of binucleated cells compared to control hiPSC-CMs (**Figure 22D**). These statistically significant differences are likely due to the large number of cells in both groups and the difference in sample sizes between both groups (2,498 MM-treated and 6,854 control hiPSC-CMs). Although interesting preliminary results, further replicates and validation are required.

	Highly Disorganized (%)	Disorganized (%)	Organized (%)	Highly Organized (%)
Control	14.6%	36.6%	44.5%	4.3%
Maturation medium	10.1%	8.4%	42.9%	38.6%

Table 9. Percentage of control and maturation medium (MM)-treated AIW002-02 hiPSC-CMs with highly disorganized, disorganized, organized, and highly organized sarcomeres. n=1 with 2,498 MM-treated hiPSC-CMs and 6,854 control hiPSC-CMs.

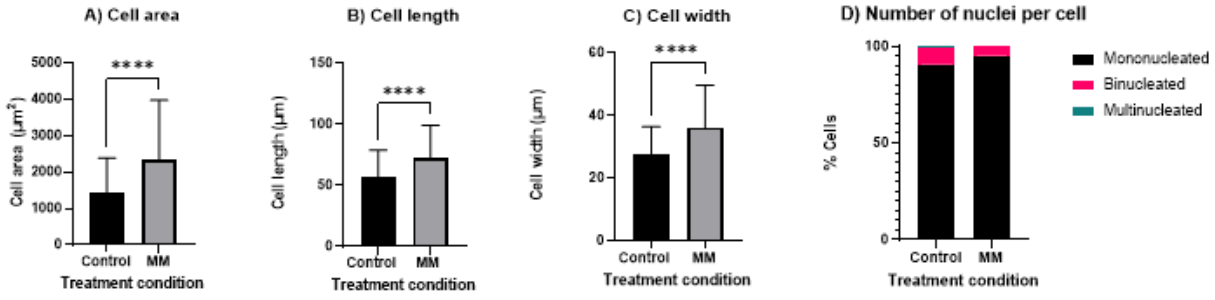

Figure 22. Morphological differences between maturation medium (MM)-treated hiPSC-CMs and control hiPSC-CMs. Comparison of **A)** cell area, **B)** cell length, **C)** cell width, and **D)**

proportion of mono-, bi-, and multi-nucleated cells between control and MM-treated hiPSC-CMs derived from AIW002-02 control patient. Unpaired t-tests reveal that mean cell area ($mean_{CTL}$= 1419 μm^2 vs $mean_{MM}$= 2326 μm^2, t=32.52), length ($mean_{CTL}$= 57.12 μm vs $mean_{MM}$= 71.94 μm, t=27.29), and width ($mean_{CTL}$= 27.68 μm vs $mean_{MM}$= 36.12 μm, t=35.31) were significantly greater in MM-treated hiPSC-CMs than in control medium-treated hiPSC-CMs. n=1 with 2,498 MM-treated and 6,854 control hiPSC-CMs. SD bars are shown. ****: $p<0.0001$.

These results suggest that this metabolic maturation protocol improves, up to a certain extent, some, but not all, hallmarks of maturity in our hiPSC-CMs and that further validation experiments and replicates are required to confirm enhanced maturity. Statistics on additional repeat experiments will be integrated by comparing means of means from single cell measurement experiments.

4.0 DISCUSSION

DCM is a heterogeneous disease with diverse etiologies and clinical manifestations that lead to high morbidity and mortality rates in affected patients. The heterogeneity of this disease is poorly understood and presents a challenge to efforts aimed at personalizing treatment options and improving patient outcomes [26]. hiPSC-CMs have proven their capacity to recapitulate underlying features of cardiac diseases, even on a patient-to-patient basis, making them an effective platform for disease modeling [26]. Phenotyping DCM patient-derived hiPSC-CMs may reflect underlying mechanisms of patient-specific cases of the disease, enabling us to gain insight into personalized treatment strategies in a bedside-to-bench-back-to-bedside manner.

In this thesis, assays and analytical tools have been developed to phenotype morphological features of DCM hiPSC-CMs which can be used in conjunction with other phenotypic assays to gain a better understanding of the pathogenesis of DCM in patient-specific cases. In addition, metabolic maturation methods were tested to enhance the maturity of patient-derived hiPSC-CMs to generate a more disease-relevant model.

4.1 Cell Painting – hiPSC-CM segmentation

The optimization of the hiPSC-CM segmentation method using the Columbus software in this thesis has enabled us to measure features of thousands of individual cells simultaneously in a high-throughput manner. The combination of WGA-488 as a membrane stain and the use of filtered mitochondria or sarcomere channels as a cytosolic marker have enabled the Columbus software to segment hiPSC-CMs within monolayers, as the membrane stain alone yielded poor

segmentation results. We must note that if cells are too confluent such that even the naked eye cannot discern cells from each other, then the software will also fail to do so. It is therefore important to seed cells at densities such as 15,000-20,000 cells per well in a 96-well plate and image within a week before excessive proliferation can occur and to include multiple rinsing steps to remove cell debris to ensure high-quality images.

However, even with optimal image conditions, Columbus, as with many computer programs, is not perfect and may still erroneously segment hiPSC-CMs to varying degrees. Despite this, it is a cost we are currently willing to accept given the high-throughput power of this method and that its accuracy is sufficient enough for our purposes. Furthermore, Columbus is user friendly and accessible compared to other programs that require coding. Our collaborators had attempted hiPSC-CM segmentation with Cell Profiler, an analysis program that requires coding, and the segmentation was suboptimal compared to Columbus. To work around the limitations of Columbus, we recommend adjusting analysis parameters to suit each experiment and set of images. To further improve cell segmentation, antibodies against membrane components such as the sodium-potassium channel or caveolin, and other software packages may be explored in the future.

4.2 Phenotyping mitochondrial morphology

4.2.1 Percentage mitochondria area

Mitochondria play a pivotal role in maintaining CM function as they generate the energy supply of CMs and are involved in regulating contractility. As DCM progresses, the number of healthy mitochondria in CMs declines, mitochondria shape and networks become abnormal or

fragmented, and the function of mitochondria become compromised [73]. In this thesis, we describe methods to evaluate mitochondrial phenotypes via our Cell Painting assay. We chose to use the MitoTracker Deep Red dye as it is a mitochondrial membrane potential-dependent dye [143] and thus, acts as an indicator of functional mitochondria within hiPSC-CMs.

The first phenotypic endpoint we investigated was the percentage of a cell occupied by functional mitochondria (% mitochondria area) using MitoTracker Deep Red. The goal was to compare the densities of healthy mitochondria within healthy and patient hiPSC-CMs. We compared two control hiPSC-CM lines and one DCM patient hiPSC-CM line. Surprisingly, the HID04C control hiPSC-CMs had a significantly greater mean % mitochondria area (57%) than both the AIW002-02 control (46%) and HID041020 DCM hiPSC-CMs (50%). Furthermore, it was surprising that the mean % mitochondria areas calculated were greater than 30% as mitochondria are reported to occupy 30% of a CM by volume [144]. There are many possible explanations for the results obtained. First, the mean % mitochondria area values that were > 30% measured from our preliminary experiments may be a consequence of the Columbus software overestimating the detected image region for mitochondria staining. As shown in **Figure 23**, certain areas with no mitochondria staining are mistakenly included in the image region. Threshold values may need to be more stringent in future analyses and other analysis methods may need to be explored.

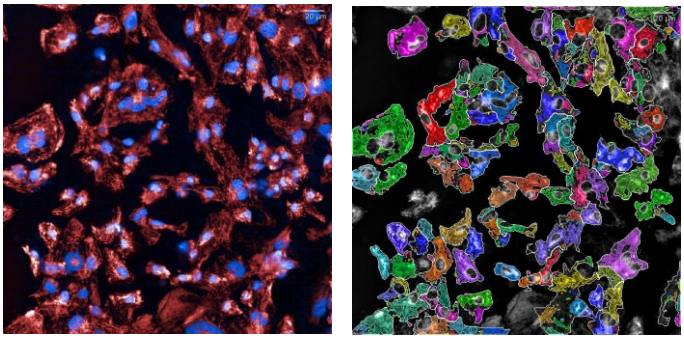

Figure 23. Columbus software overestimates the detection of mitochondria image regions. **Left:** MitoTracker Deep Red (red) stains mitochondria and Hoechst (blue) stains nuclei. Input image for percentage mitochondria area analysis with membrane channel not shown. **Right:** Columbus software overestimates the detection of mitochondria image regions (various colors).

Secondly, the images acquired in our Cell Painting workflow are 2D cross-sectional planes of hiPSC-CMs which may not recapitulate the volume, density, and distribution of mitochondria within a 3D cell. To address this limitation, future studies should acquire images at multiple planes and superimpose them during image analysis to evaluate this phenotype in a more 3D approach. Finally, there is variability in the dataset that was used for comparing % mitochondria area between the three different hiPSC-CM lines that must be considered. The number of wells and individual cells included in each group vary. There were 828 cells in the HID041020 DCM group, 1,650 cells in the HID04C control group, and 40,236 cells in the AIW002-02 control group. Furthermore, the age of the hiPSC-CMs among the groups also varied with cells being 46 days old, 72 days old, and 50 days old in the HID041020, HID04C, and AIW002-02 groups, respectively. These variables may have affected mean values for % mitochondria area. Future experiments will require standardized age and number of cells measured and compared or isogenic controls. Given the variability and lack of replicates, further optimization of this method is required.

Given the limitations of this method so far, other assays and methods may be recommended instead to assess mitochondrial health. Other reported imaging-based assays measure the intensity

ratio between membrane potential-dependent compounds such as JC-1 [78] or MitoTracker™ Deep Red and membrane potential-independent dyes such as MitoTracker™ Green or Nonyl Acridine Orange to assess mitochondrial potential per unit of mitochondrial mass on a single cell basis to measure healthy mitochondrial mass [77]. Imaging-based assays to evaluate mitochondria health should also be paired with functional assays such as Seahorse XF Analyzer (Agilent Technologies) assays which measure extracellular respiration rate and oxygen consumption rates as surrogate measures for oxidative phosphorylation and glycolysis in mitochondria [145].

4.2.2 Mitochondria distribution in hiPSC-CMs

The next mitochondrial phenotype we measured and described in this thesis was mitochondria distribution within a cell. Immature CMs are characterized by having more perinuclear mitochondria (PNM) than intermyofibrillar mitochondria (IFM) compared to mature CMs [82]. In failing hearts, PNM are more susceptible to membrane potential depolarization than IFM at baseline and under physiological stress [83]. Therefore, characterizing mitochondrial distribution within a CM may provide insight into the state of disease and maturity of CMs in DCM.

Preliminary results revealed that AIW002-02 control hiPSC-CMs had a higher proportion of cells with mitochondria distributed around the nucleus (66%) compared to HID04C control (42%) and HID041020 DCM (41%) hiPSC-CMs. Note, mitochondria measured in this assay are mitochondria with intact membrane potentials as we used the MitoTracker Deep Red stain. The fact that AIW002-02 control hiPSC-CMs had a higher proportion of cells with increased PNM

staining than the HID04C control hiPSC-CMs may indicate a less mature CM phenotype in the AIW002-02 control cells. This is also in line with the age of the cells at the time of manipulation. AIW002-02 control cells were 50 days old whereas the HID04C control cells were 72 days old when imaged. Furthermore, AIW002-02 control hiPSC-CMs also had a higher proportion of PNM staining compared to HID041020 DCM hiPSC-CMs which may reflect the disease status of these cells given that PNM are more sensitive to membrane depolarization in failing CMs. However, results are only preliminary and the number of cells in each group vary (828 HID041020 DCM hiPSC-CMs, 1,650 HID04C control hiPSC-CMs, and 40,236 AIW002-02 control hiPSC-CMs). Thus, we currently cannot firmly draw conclusions from these results.

Future experiments may use this endpoint to compare hiPSC-CMs pre- and post-metabolic maturation treatments to validate hiPSC-CM maturity. This endpoint can also be used to assess disease status of patient hiPSC-CM lines as well as provide insight into underlying mitochondria-related causes of DCM. However, in future experiments, it would be important to use a membrane potential-independent dye such as MitoTracker Green to normalize results to the total mitochondrial mass in order to reliably compare membrane depolarization in PNM between hiPSC-CM lines.

4.3 Characterizing hiPSC-CM cellular morphology

Features of hiPSC-CM cellular morphology may provide insight into underlying mechanisms of DCM. For example, abnormal nuclear shape, decreased nuclear roundness, fragmented nuclei, or multi-nucleated CMs are a phenotype reported in certain DCM cases caused by specific *LMNA* mutations [68]. Therefore, in this thesis, we developed two versions of a Cell

Painting assay to characterize cellular morphology features. The first version consisted of measuring mitochondria and sarcomere morphology in different cells and the second version was able to measure mitochondria, sarcomere, cell, and nuclei morphology in the same cells. Features measured were nucleus area, nucleus roundness, cell area, cell roundness, cell length, cell width, cell width:length ratio, and the proportion of mono-, bi-, and multi-nucleated cells. These morphological features may reveal underlying mechanisms of DCM and genotype-phenotype relationships. These features can also be used to validate hiPSC-CM maturation as CMs become larger, more elongated, less round, and more binucleated as they mature [82].

Using the first version of the Cell Painting protocol, we compared cellular morphology features between HID041020 DCM hiPSC-CMs and AIW002-02 control hiPSC-CMs. We observed that HID041020 DCM hiPSC-CMs had significantly greater mean nucleus roundness, nucleus area, cell area, and cell width than AIW002-02 control hiPSC-CMs. HID041020 DCM hiPSC-CMs also had significantly decreased cell roundness, cell length, and cell width:length ratios compared to AIW002-02 control hiPSC-CMs.

To our knowledge, increased nucleus area and cell width and decreased cell roundness and cell width:length ratios have not previously been reported in DCM hiPSC-CMs. It was interesting that HID041020 DCM hiPSC-CMs were larger than control hiPSC-CMs as this may reflect the compensatory hypertrophic response observed in CMs during dysfunction in DCM [48].

Furthermore, it was hypothesized that DCM hiPSC-CMs would have increased cell length relative to control as sarcomeres are reported to be added in series (eccentric hypertrophy) and

increase CM length as part of a compensatory mechanism in response to CM dysfunction [50]. However, a decrease in CM length was observed instead.

Also, decreased nucleus roundness was expected in the DCM group, but the opposite result was observed. Although statistically significantly different, due to the large number of hiPSC-CMs measured, the mean nucleus roundness values of control and DCM hiPSC-CMs ($mean_{control}$: 0.7702 vs $mean_{DCM}$: 0.8370) are still both above a 0.6 circularity index value. Previous reports have considered nuclei with a circularity index below 0.6 to be irregularly shaped [70].

Finally, the AIW002-02 control hiPSC-CMs had a higher proportion of binucleated (10%) and multinucleated cells (1%) compared to HID041020 DCM hiPSC-CMs. This was unexpected in the control hiPSC-CMs as multinucleated cells have been linked to cardiac disease progression [146]. In response to injury or disease, CMs undergo a hypertrophic response in terms of size and sarcomere growth and it is hypothesized that an increased number of nuclei may serve to provide increased transcriptional output to support growing CMs with higher demands [146]. Multinucleation has also been reported in certain *LMNA* mutations underlying DCM [84]. However, given that multinucleated cells only represent 1% of the control hiPSC-CMs and that 11,755 cells were measured in the control group whereas only 2,455 cells were measured in the DCM group, the difference may be negligeable given the difference in sample sizes.

This preliminary experiment was only performed in one biological replicate with a different number of cells measured in each group (11,755 cells in AIW002-02 control group and 2,455 cells in HID041020 DCM group) which likely affected the mean values and explains the statistically

significant results. Hence, more biological replicates and standardization of group sizes are required prior to confirming or explaining any of these results.

4.4 Sarcomere organization

In this thesis, we improved upon a previous method in our lab to evaluate sarcomere organization. Disorganized and misaligned sarcomeres have become an established phenotype of immature CMs and this phenotype is commonly reported in DCM *in vitro*, particularly in cases caused by mutations in myofibrillar protein-encoding genes and in response to stress. Therefore, evaluating the degree of sarcomere organization in hiPSC-CMs may reflect maturity status, disease progression, and underlying causes of DCM.

A former Master's student in the lab, Cara Hawey, adapted a protocol by Mosqueira *et al*. [70] to classify images of hiPSC-CMs based on the level of their sarcomere organization from highly disorganized, disorganized, organized, and highly organized. However, one of the limitations of her method was that there was no membrane stain and thus hiPSC-CM segmentation was not as reliable. Columbus would sometimes mistake sarcomere lines as cell borders and improperly segment cells if not separated properly during replating steps. To improve this method, we introduced the membrane stain, WGA-488, which enabled us to segment hiPSC-CMs even within monolayers, up to a certain extent.

Using this improved version of the sarcomere organization analysis method and the first version of our Cell Painting protocol, we compared sarcomere organization between HID041020 DCM hiPSC-CMs and AIW002-02 control hiPSC-CMs. As expected from DCM hiPSC-CMs, the

HID041020 DCM hiPSC-CMs had a higher proportion of cells with highly disorganized or disorganized sarcomeres and a decreased proportion of cells with highly organized or organized sarcomeres compared to AIW002-02 control hiPSC-CMs. Sarcomere disorganization is a phenotype commonly reported and recapitulated in hiPSC-CMs derived from DCM patients [64, 65, 147]. Hence, these results may suggest that the DCM phenotype was recapitulated by HID041020 DCM hiPSC-CMs compared to AIW002-02 control hiPSC-CMs. However, this experiment was only performed with one biological replicate and the number of cells in each group were different (11,755 cells in the AIW002-02 control group and 2,455 cells in the HID041020 group) which may influence the percentage values and results. Thus, we cannot make firm conclusions from this data.

In the future, it would be interesting to treat hiPSC-CMs with 10 μM norepinephrine or isoproterenol to recapitulate adrenergic stress *in vitro* and evaluate sarcomere organization following this treatment. Cara Hawey and other studies have reported that some DCM hiPSC-CM lines are more susceptible to adrenergic stress as demonstrated by an increased percentage of cells with disorganized sarcomeres following epinephrine treatment relative to baseline compared to control hiPSC-CMs [64]. This stress-induced sarcomere disorganization phenotype was rescued by pre-treating cells with β-blockers such as metoprolol [64], which may also be interesting to test in future experiments. These results may reveal underlying disease mechanisms at the myofilament and possible treatment responses among different patient-derived DCM hiPSC-CM lines.

4.5 Cell Painting protocol 2: Multiplexing dyes to characterize mitochondria, cell, nucleus, and sarcomere morphology in the same cells

The drawback to the first version of our Cell Painting protocol was that mitochondria morphology had to be evaluated separately and in different cells from those used to characterized cellular, nuclear, and sarcomere morphology. Seeking to improve our method, we aimed to combine these two acquisitions into the same experiment to extract all of our morphological features of interest from the same cells.

We began preliminary experiments to improve our original Cell Painting protocol with the goal of multiplexing markers for mitochondria, the cell membrane, the nucleus, and the sarcomeres. We did so by replacing the secondary antibody, Alexa Fluor 647, targeted to the anti-α-actinin primary antibody, with Alexa Fluor 555 to eliminate spectral overlap between the mitochondria and sarcomere stains. The first attempt at this version of the protocol yielded inconsistent immunostaining results with Alexa Fluor 555 which likely affected image segmentation as the sarcomere signals are used as a cytosolic marker for hiPSC-CM segmentation. Consequently, inconsistent immunostaining likely also affected our morphological results.

We received an old aliquot of Alexa Fluor 555 from a different lab as we only wanted to test the potential of this antibody in our multiplexing approach. The age, exposure to light, and number of freeze-thaw cycles of the aliquot were unknown and may have been responsible for inconsistent staining results [148]. Furthermore, the concentration and incubation time tested may not have been optimal with hiPSC-CMs and targeting anti-α-actinin. Finally, the high-content imaging system's parameters such as laser power and acquisition speed may also require adjusting.

Future optimization steps should involve using a new aliquot of Alexa Fluor 555 and testing various concentrations, incubation times, laser power intensities and acquisition speeds.

We compared the sarcomere organization results generated from the first version of the Cell Painting protocol with results generated from the second version of the protocol using different halves of the same plate of AIW002-02 control hiPSC-CMs for each protocol. The AIW002-02 cells that underwent the second version of the protocol (AIW002-02 Alexa Fluor 555) had a similar percentage of cells with highly disorganized sarcomeres as the AIW002-02 cells that underwent the first version of the Cell Painting protocol (AIW002-02 Alexa Fluor 647). However, AIW002-02 cells from the second version of the protocol with AlexaFluor 555 staining had 70.7% of cells with disorganized sarcomeres, 18.6% organized sarcomeres, and 0.6% highly organized sarcomeres. This is a contrast to AIW002-02 cells from the first version of the protocol with Alexa Fluor 647 which had 30.1% disorganized, 41.1% organized, and 18% highly organized sarcomeres. Furthermore, AIW002-02 Alexa Fluor 555 hiPSC-CMs had significantly greater mean nucleus area, nucleus roundness, and cell length, and significantly decreased mean cell area, width, roundness, and width:length ratios. The proportion of mono-, bi-, and multinucleated cells, however, were similar between both groups.

The goal was to assess whether both protocols would yield similar results using cells from the same hiPSC-CM line, passage, and 96-well plate. Hence, these results were surprising as the cells from both protocol conditions were from the same 96-well plate, but simply occupied different halves of the plate. We must note that there were 11,755 cells in the AIW002-02 Alexa Fluor 647 group and only 6,730 cells in the AIW002-02 control Alexa Fluor 555 group. The

different sample sizes may have influenced the results. However, it is surprising that the same number of wells in each condition contained such drastically different numbers of hiPSC-CMs given that they were from the same plate.

Possible explanations may include improper hiPSC-CM segmentation due to inconsistent Alexa Fluor 555 staining or inconsistent seeding densities when replating from 6-well to 96-well plates. Achieving consistent seeding densities when replating may be difficult when hiPSC-CMs are very confluent in 6-well plates and are difficult to separate which may create an uneven cell suspension and consequently, inconsistent seeding in 96-well plates. Furthermore, the series of wash steps and image acquisitions in the second Cell Painting protocol may have caused too much stress to the cells compared to the first version of the protocol which has less washing steps, resulting in more cell death prior to analyzing sarcomere organization. Overall, we cannot make conclusions from this experiment with a single biological replicate and it is evident that further optimization is required to reliably segment hiPSC-CMs and effectively multiplex markers for mitochondria, the cell membrane, nuclei, and sarcomeres. Future optimization experiments should address the possible sources of variability mentioned.

4.6 Metabolic Maturation

Although hiPSC-CMs provide a useful platform for disease modeling, their immature phenotype limits their use in recapitulating features of adult diseases. In this thesis, we tested two published metabolic maturation protocols on our 2D monolayer hiPSC-CM cultures.

4.6.1 Metabolic maturation using protocol by Funakoshi et al. [128]

The first protocol tested was one by Funakoshi *et al*. [128] comprised of a low glucose basal medium supplemented with palmitate, dexamethasone, T3 hormone, and a PPARα agonist for the first 9 days followed by palmitate and low glucose medium only for the remaining 5 days of the protocol. This protocol unfortunately resulted in cell death before reaching the end of the protocol.

We identified palmitate as the maturation medium (MM) component that was responsible for the observed cell death. This was in line with other reports of long-term exposure or exposure to high concentrations of fatty acids (FAs) in glucose-depleted media resulting in lipotoxicity and cell death [149]. The protocol was originally intended for 3D embryoid bodies in which hiPSC-CMs would experience FA exposure differently than in 2D cultures. Hence, we tested different concentrations of palmitate on hiPSC-CMs and observed that palmitate concentrations at or above 100 μM resulted in hiPSC-CM death. A concentration of 50 μM of palmitate was able to support hiPSC-CM survival which corroborated other reports in which one million hiPSC-CMs were able to take up to ~ 57 μM of FAs after two days of feeding [94].

We did not continue optimizing this protocol as we had decided to test a protocol already designed for 2D hiPSC-CM monolayers instead. However, if we were to continue optimizing this protocol, we would test palmitate concentrations in a range closer to 50 μM to determine the highest concentration of FAs that could sustain cell survival and induce the highest degree of maturation.

These experiments were only performed twice in AIW002-02 control hiPSC-CMs and therefore, further replicates are necessary to confirm results. Additionally, cell death was evaluated using visual inspection with a light microscope and image acquisition. To increase accuracy of hiPSC-CM apoptosis measurements throughout the maturation protocol, dyes such as CellTox Green (Promega) may be used instead to monitor cell viability over time. CellTox Green is a dead cell indicator that binds the DNA of dead cells due to their compromised membrane integrity [150]. Using the CellCyteX (Cytena), an incubator-safe live-imaging system with both fluorescent and brightfield channels, CellTox Green fluorescence may be monitored over time to better assess hiPSC-CM death during this metabolic maturation protocol.

4.6.2 Metabolic maturation using protocol by Feyen et al. [129]

The second metabolic maturation medium tested was by Feyen *et al*. [129]. The 3-5 week-long protocol was designed for 2D hiPSC-CM cultures and was comprised of a low glucose basal medium supplemented with fatty acids, L-lactate, vitamin B12, biotin, creatine monohydrate, taurine, L-carnitine, and non-essential amino acids [129]. This protocol resulted in MM-treated hiPSC-CMs with more elongated and rod-shaped phenotypes compared to the small and round phenotypes observed in the control medium-treated hiPSC-CMs. These phenotypes were observed in both the HID041127 DCM and AIW002-02 control hiPSC-CM lines. This may be indicative of increased maturity as rod-shaped phenotypes are features of mature CMs whereas small and round phenotypes are characteristic of fetal CMs [89]. However, further replicates are required to corroborate these observations. Morphological features are not sufficient evidence of increased maturity and therefore, further validation experiments were required.

We next validated the Feyen *et al*. protocol by evaluating the changes in mature gene expression using qPCR. MM-treated hiPSC-CMs had increased expression of the adult isoform (*TNNI3*) and decreased expression of the fetal isoform (*TNNI1*) of the gene encoding cardiac troponin I. An expected decrease in expression of genes encoding transcription factors, *GATA4* and *NKX2.5*, was also observed in MM-treated hiPSC-CMs compared to control. *GATA4* and *NKX2.5* expressions are present in early CM development, but decrease as CMs mature [139] [141]. These results may suggest that the MM improves hiPSC-CM maturity, but this experiment was only performed once in HID041127 DCM hiPSC-CMs. AIW002-02 control hiPSC-CMs reserved for qPCR experiments had become contaminated prior to RNA isolation. Hence, further replicates are necessary to evaluate whether these differences in expression are significant. Future studies should also investigate other gene expression changes that are key in CM maturation such as the expression of genes encoding the fetal isoform of myosin heavy chain (*MYH6*), adult isoform of myosin heavy chain (*MYH7*), fetal isoform of titin (*N2BA*), adult isoform of titin (*N2B*), sarco-endoplasmic reticulum ATPase (SERCA2A), potassium/sodium hyperpolarization-activated cyclic nucleotide-gated channel 4 (*HCN4*), and sodium channel protein type 5 subunit alpha (*SCN5A*).

Next, we compared sarcomere organization pre- and post-MM as improved sarcomere alignment is an established feature of mature CMs. As expected, MM-treated hiPSC-CMs had a higher proportion of cells with highly organized sarcomeres (39%) compared to control hiPSC-CMs (4%). There also was a lower percentage of MM-treated hiPSC-CMs with highly disorganized (10%) or disorganized (8%) sarcomeres compared to control hiPSC-CMs (15% highly disorganized and 37% disorganized). Although promising results, further replicates are

required as this experiment was only performed once in AIW002-02 control hiPSC-CMs and the number of cells in each group were different (2,498 MM-treated hiPSC-CMs and 6,854 control hiPSC-CMs). HID041127 hiPSC-CMs intended for sarcomere organization evaluation had become contaminated prior to immunostaining and imaging.

Preliminary qPCR and sarcomere organization results indicate that the metabolic maturation protocol by Feyen *et al.* yields more mature hiPSC-CMs and has proven to be a more suitable and successful method for our lab than the Funakoshi *et al*. protocol. Although these preliminary results are promising, we acknowledge that existing *in vitro* maturation techniques for hiPSC-CMs are still insufficient for replicating a fully-adult-like CM state as found *in vivo*. There is always room for improvement in hiPSC-CM maturity. However, the maturity status of our hiPSC-CMs following the Feyen *et al*. metabolic maturation protocol is currently sufficiently mature for our current research purposes. Our hiPSC-CMs express cardiac GPCRs important for CM function such as adrenergic receptors, angiotensin receptors, and endothelin receptors (data not shown) and a high proportion of organized sarcomeres (**Figure 21**) following metabolic maturation. These properties enable us to characterize features of GPCR signaling phenotypes, morphology, and calcium handling. Even prior to metabolic maturation experiments, other lab members were able to identify differences in calcium handling and GPCR signaling between patient hiPSC-CM lines. Other studies have also used the Feyen *et al* [129]. maturation protocol to induce a "mature enough" model for phenotyping diseases, such as catecholaminergic polymorphic ventricular tachycardia [126]. However, we are working to further improve maturity as there are still features of mature CMs that are lacking in our hiPSC-CMs, such as the presence of transverse tubules, which play an important role in calcium handling and contractility [151].

For this reason, we have recently started culturing 3D cardiac organoids from our patient hiPSC-CM lines for our phenotypic assays.

In addition to qPCR and sarcomere organization validation experiments, future experiments should validate functional hiPSC-CM maturity with contractility assays, electrophysiology assays, and metabolic assays. Previous Master's student in our lab, Cara Hawey, developed contractility and electrophysiology assays using the CardioExcyte96 (Nanion Technologies). The CardioExcyte96 uses electrodes to measure impedance and extracellular field potential (EFP) which can be used as surrogate measures of contractility and action potentials to characterize beat rate, beat amplitudes, EFP, and EFP amplitudes [152]. We would expect more mature CMs to have increased beat rates and amplitudes compared to immature CMs, particularly in response to epinephrine or norepinephrine [89]. Metabolic assays evaluating mitochondrial health and respiration can be evaluated using the Seahorse XF Analyzer (Agilent Technologies) which measures oxygen consumption rates (OCR) and extracellular acidification rates (ECAR) as surrogate measures of mitochondrial respiration and glycolysis, respectively [145]. We would expect mature CMs to have increased OCRs and decreased ECARs as the primary form of metabolism in CMs transitions from glycolysis to oxidative phosphorylation as CMs mature [89].

4.7 Limitations

The greatest limitation to the use of hiPSC-CMs in disease modeling remains their immature phenotype which closely resemble fetal or neonatal CMs rather than adult CMs. In this thesis, we have highlighted various methods that have successfully improved hiPSC-CM maturity including metabolic maturation medium, mechanical and electrical pacing, manipulating substrate

types and thicknesses, long-term culture, co-culture methods, and 3D cultures. The results in this thesis have demonstrated the potential of improved maturity in hiPSC-CMs using metabolic medium formulations. However, it is crucial to recognize that although these maturation methods enhance CM maturation, none of them have successfully matured hiPSC-CMs to resemble a fully "adult-like" state. These individual techniques alone are not sufficient to fully mature hiPSC-CMs and a combination of various methods will be needed to increase the extent of hiPSC-CM maturity possible *in vitro*. There has been a consensus that 3D engineered cardiac tissues comprised of hiPSC-CMs, non-CM cells, and ECM treated with soluble factors and subjected to electrical pacing and mechanical stress will produce the most mature CMs *in vitro* [89]. Even still, the regulators of CM maturation *in vitro* may be different or lack overlap with the regulators of CM maturation in *vivo* [89]. The most mature CMs *in vitro* are still far from resembling CMs *in vivo*. Hence, more research is required to understand regulators of CM maturation and *in vivo* validation of *in vitro* maturation methods may be useful in overcoming this hurdle. Significant progress has been made, however, and despite this limitation, hiPSC-CMs have provided valuable insight into underlying disease mechanisms of various diseases [153].

Another possible limitation of using hiPSC-CMs in disease modeling is the heterogeneity of hiPSC-CMs following differentiation. hiPSC-CM differentiation protocols generate >95% pure functional CMs [132]. The remaining 5% of cells include cells that have not fully differentiated from hiPSCs into CMs or other cell types that share lineages with CMs such as cardiac fibroblasts [132]. Non-CM cells may influence results or interfere with modeling of cardiac diseases. To mitigate this, our Cell Painting protocol excludes non-CM cells based on texture and intensity properties of anti-α-actinin primary antibody staining. Anti-α-actinin staining in CMs produces a

striated and band-like pattern in CMs [64], but reveals filamentous bundles of actin filaments in fibroblasts at lower fluorescence intensities [154] which can be filtered out during analysis.

Furthermore, even among the successfully differentiated hiPSC-CMs, there is heterogeneity in terms of maturity level and CM subtypes [155] which may contribute to the differences observed in the Cell Painting experiments. DCM mainly affects ventricular CMs, but hiPSC-CM populations display a spectrum of action potential phenotypes indicating that hiPSC-CMs contain subpopulations of nodal, atrial, and ventricular CMs [156]. Non-ventricular CMs may not fully recapitulate phenotypes of ventricular CMs in disease. To ensure pure ventricular CM populations, fluorescence-activated cell sorting (FACS) may be used to purify hiPSC-CM populations [156]. Alternatively, ventricular myosin light chain 2 (MYL2) is a marker unique to ventricular CMs [157] and immunofluorescence staining with anti-MYL2 antibodies can identify ventricular CMs within a population using fluorescence microscopy [157].

Furthermore, the process of induced reprogramming relies on erasing the existing epigenetic makeup of the cell of origin [158] which may obscure the retention of disease mechanisms of disorders influenced by epigenetic modifications [159]. However, reports have suggested that somatic cell source influences the efficiency of hiPSC differentiation into specific lineages, suggesting some retention of epigenetic memory [160]. The extent to which hiPSCs retain epigenetic memory following reprogramming is therefore complex and poorly understood [161] and hinders our ability to model DCM caused by an accumulation of epigenetic modifications and environmental factors over a lifetime, as is the case in many forms of DCM [10]. For example, diabetic cardiomyopathy is a common complication of type 2 diabetes [162].

Increasingly more research has revealed that the complex interplay between epigenetic changes and environmental factors may significantly contribute to the development of cardiovascular complications secondary to diabetes [162]. Therefore, the Heart-in-a-dish project is currently focused on studying genetic and chemotherapeutic-induced forms of DCM which we hope will provide insight into disease mechanisms that may have overlap with epigenetic-influenced or idiopathic forms of DCM.

When characterizing phenotypic differences between DCM and healthy patients, clinical data such as age and sex should be taken into consideration when drawing comparisons, which we have begun doing. In many cardiovascular diseases, male sex is a risk factor for developing heart failure [10]. DCM is more prevalent in men than it is in women, at a ratio of 3:1 for men to women [163]. Men with DCM tend to present symptoms at a younger age, experience more arrhythmias, dyspnea, and worse systolic dysfunction than women. Men are also more likely to progress towards end-stage heart failure and death than women [164]. However, studies on sex-specific differences in DCM are few and there is little information on sex-specific differences in treatment response, outcome, and underlying causes. Further emphasis should be placed on the study of sex-specific differences in DCM to understand disease or cardioprotective mechanisms and phenotypes to improve screening, diagnosis, and treatment of DCM in all patients [164].

Finally, in this thesis, we present tools to characterize morphological phenotypes in patient-derived hiPSC-CMs as part of the Heart-in-a-dish (HID) project which aims to phenotype hundreds of DCM patient hiPSC-CM lines and cluster patients with similar phenotypes to improve diagnostic guidelines and personalized treatments. Evidently, phenotyping morphological features

alone is insufficient to form DCM phenotypes. Therefore, morphological phenotypes will need to be coupled to other phenotypic endpoints to paint a complete picture of the disease in each patient. We discuss this further in future directions.

4.8 Future directions

Current treatments for DCM, a complex disease with high morbidity and mortality, are based on ejection fraction and NYHA classification, which is determined by the extent to which a cardiovascular disease limits physical activity [165]. Using this stratified one-fits-all approach disregards the complex underlying etiologies of the disease and the heterogeneity in treatment responses observed in patients [165]. In fact, the sequence in which pharmacological therapies for heart failure are administered is often determined by the order in which these drugs underwent their clinical trials rather than a biological justification [14]. Therefore, there have been many efforts to improve treatment guidelines for DCM patients in a more personalized approach [58]. Phenotyping DCM patients can generate cellular and molecular profiles that can be related back to clinical data and treatment responses. Patient clusters can be used to better understand DCM subtypes which can improve diagnosis and personalize treatment options and sequences in which they are administered in on a cluster-to-cluster basis. Previous studies have generated "phenogroups" based on patterns in clinical, genetic, and proteomic data from cardiac biopsies from DCM patients to inform better clinical decision-making for DCM patients [165]. However, this is just the beginning and further studies are required on a larger scale.

Using hiPSC-CMs, which recapitulate underlying features of the disease in a less invasive manner than cardiac biopsies, we can generate phenotypic clusters as part of a "bedside-to-benchside-back to-bedside" approach [58]. In contrast to studies that use hiPSC-CMs to model a specific case of DCM using one or two patient cell lines compared to isogenic controls, the Heart-in-a-dish (HID) project has established a pipeline to recruit, generate, and characterize hundreds of DCM patient hiPSC-CM lines to create cellular and molecular profiles linked to clinical data that may identify phenotypic clusters and help personalize treatment options.

In this thesis, as part of the HID project, we validated a metabolic maturation protocol and developed a Cell Painting assay for morphological phenotyping of hiPSC-CMs from DCM patients. However, the morphological phenotypes characterized using the Cell Painting assay will need to be matched to other phenotypic endpoints in order to cluster patients and fully recapitulate patient-specific cases of DCM. The HID project has already developed assays and tools to phenotype other features of the disease. Previous student, Cara Hawey, developed tools to phenotype contractility, electrophysiology, cell viability, and sarcomere organization. A previous PhD student, Dr. Kyla Bourque, developed a workflow to investigate cellular signaling events and kinase activities, such as those of PKA and $ERK_{1/2}$, in response to adrenergic, endothelin, and angiotensin receptor agonists in live cells, and in distinct subcellular compartments using genetically-encoded biosensors [166, 167]. A previous postdoctoral fellow, Dr. Karima Alim, developed a modified clustering analysis pipeline based on work by Chavez-Abiega *et al*. [168] to cluster hiPSC-CMs based on their response to GPCR ligands to better understand dysregulated signaling events downstream of key receptors involved in cardiac function and DCM. Finally, Master's student,

Grace Mazarura, is phenotyping signaling events in cardiac fibroblasts as they also play an important role in the progression of DCM.

Next steps will involve the combination of all of these methods to characterize patient-derived hiPSC-CMs from a morphological, calcium handling, and GPCR signaling perspective to cluster patients with similar phenotypes. To link these phenotypes together, not only will we assess morphological, calcium handling, and GPCR signaling phenotypes in hiPSC-CMs at baseline, but we will also do so in response to ligands that activate GCPR signaling pathways in the heart. The goal is to observe how changes in underlying signaling events are reflected in contractile function and morphology. These holistic cellular phenotypes are important, but a challenge will be linking these phenotypes to the disease. For example, we may see statistically significant differences in sarcomere organization between DCM and healthy hiPSC-CMs, but how do we determine the benchmark values for normal vs. diseased state and whether or not these differences are truly indicative of the disease state? To address this limitation, we will eventually compare our cellular and morphological phenotypes to clinical data and genotyping data from patients to generate "phenogroups" in order to link cellular phenotypes to clinical phenotypes of the disease in patients. This concept has been previously demonstrated when Verdonschot *et al*. [169] generated 4 "phenogroups" from a cohort of DCM patients using cardiac biopsies to establish "phenogroups" based on cardiac transcript signatures, disease aetiology, comorbidities, and cardiac function. This will also help us determine benchmark values that are truly indicative of the disease state. To determine whether our morphological parameters are in the normal range or not, we plan on comparing phenotypes from DCM patients to those of healthy individuals who do not have the disease. Finally, performing enough replicates of these experiments should generate a range of

normal values within which morphological parameters from our healthy hiPSC-CMs will fall under.

The logistics of combining our phenotypic approaches together may involve the same plate of hiPSC-CMs to first undergo assays to characterize contractility and electrophysiology. Once done, hiPSC-CMs can then be transduced with genetically-encoded biosensors to perform GPCR signaling assays on live cells before finally being stained with dyes and antibodies to characterize morphological features using the Cell Painting method. To match single-cell data from GPCR signaling experiments and Cell Painting experiments, we plan to use a cell registration method developed by postdoctoral fellow, Dr. Étienne Billard. After both GPCR signaling and Cell Painting experiments are complete, this method consists of matching single cell data based on matching x and y coordinates of single cells within an image from the same field, well, and plate. Coordinates are measured by the Columbus image analysis software.

To address the limitations of hiPSC-CM immaturity, we plan to continue trying different maturation methods and combinations. We will continue validating the Feyen *et al*. [129] metabolic maturation medium before implementing it regularly into our pipeline. Previous and current students, Dr. Kyla Bourque, Hanwen Wang, Arianna He, and Alex Cai, have generated 3D cardiac organoids from hiPSCs that self-assemble and differentiate into different cardiac cell types [170]. Co-culture and 3D culture methods are both taken advantage of in this 3D cardiac organoid model to mature hiPSC-CMs *in vitro* and generate a more disease-relevant model for our phenotypic assays. Cardiac specific and myofilament-localized genetically-encoded biosensor, RGECO-TnT [171], has already been successfully transduced into the hiPSC-CMs of our

generated cardiac organoids, demonstrating that GPCR signaling assays can be performed in this 3D model. The use of biosensors that localize to CM-specific structures enables us to eliminate variability of results that may be caused by the heterogeneity of cells within hiPSC-CM populations. To further circumvent the issue of hiPSC-CM subtype heterogeneity, we are currently developing genetically-encoded biosensors with CM-subtype-specific promoters [172].

Furthermore, we are in collaboration with the Ehrlicher lab at McGill to culture our hiPSC-CMs on substrates of different stiffnesses generated by the Ehrlicher lab to assess improvements in hiPSC-CM maturity. If results are successful, future directions would be to combine long-term hiPSC-CM culture, metabolic maturation, manipulating substrate thickness, and 3D cardiac organoid cultures to induce a more mature phenotype in our hiPSC-CMs and a more disease-relevant model for our phenotypic assays.

The phenotypic assays developed and mentioned in this thesis will enable us to compare cellular and molecular profiles between DCM patient lines to elucidate underlying disease mechanisms and better direct treatment strategies and drug discovery for DCM patients. Insight gained from phenotypic clusters may also elucidate mechanisms underlying sex differences in DCM. Our current and future efforts to mature hiPSC-CMs will provide a more disease-relevant model which will refine our ability to recapitulate features of the disease that can be characterized using our phenotypic assays. Overall, these efforts will all contribute towards our end goal of improving diagnosis, personalized treatment, and disease outcomes for DCM patients.

5.0 CONCLUSION

DCM is the second most common cause of heart failure and the most common indication for heart transplantation. It is a complex disease with heterogeneous etiologies, disease mechanisms, and clinical manifestations that are yet to be fully understood. Although therapeutic options are available, morbidity and mortality remain unacceptably high, highlighting the need for more effective and personalized treatment options for DCM patients. This thesis contributes towards a larger project, the "Heart-in-a-dish" project which aims to phenotype hiPSC-CMs derived from DCM patients to better understand underlying mechanisms of the disease and improve patient outcomes.

The work in my thesis focuses on the development of assays to phenotype morphological features of patient-derived hiPSC-CMs and to metabolically mature hiPSC-CMs to induce a more disease-relevant model. Troubleshooting was done to develop a Cell Painting assay to characterize various features of hiPSC-CM, nucleus, mitochondria, and sarcomere morphology at the single cell level in a high-throughput manner. This thesis demonstrates that this method can be used to characterize morphological differences in both control- and DCM patient-derived hiPSC-CMs. Additionally, we tested and validated a published metabolic maturation protocol which, according to our preliminary results, produced hiPSC-CMs with more mature sarcomere organization and gene expression phenotypes.

With our collaborators, we will use the assays developed in this thesis along with other phenotypic assays developed by other members of this project to characterize various features of DCM in patient-derived hiPSC-CMs. This workflow will allow us to better understand the disease

and cluster DCM patients with similar clinical, cellular, and molecular phenotypes into defined disease subgroups, paving the way for improved diagnostic guidelines, personalized treatment options, and novel therapeutic development to ultimately improve quality of life and outcomes in DCM patients.

REFERENCES

1. Lozano, R., et al., *Global and regional mortality from 235 causes of death for 20 age groups in 1990 and 2010: a systematic analysis for the Global Burden of Disease Study 2010.* Lancet, 2012. **380**(9859): p. 2095-128.
2. Canada, G.o., *Report From the Canadian Chronic Disease Surveillance System: Heart Disease in Canada, 2018*, P.H.A.o. Canada, Editor. 2018: Ottawa. p. 70.
3. Gerber, Y., et al., *A contemporary appraisal of the heart failure epidemic in Olmsted County, Minnesota, 2000 to 2010.* JAMA Intern Med, 2015. **175**(6): p. 996-1004.
4. Rosenbaum, A.N., K.E. Agre, and N.L. Pereira, *Genetics of dilated cardiomyopathy: practical implications for heart failure management.* Nat Rev Cardiol, 2020. **17**(5): p. 286-297.
5. Harmon, W.E., et al., *Pediatric transplantation, 1994-2003.* Am J Transplant, 2005. **5**(4 Pt 2): p. 887-903.
6. McKenna, W.J., B.J. Maron, and G. Thiene, *Classification, Epidemiology, and Global Burden of Cardiomyopathies.* Circ Res, 2017. **121**(7): p. 722-730.
7. Richardson, P., et al., *Report of the 1995 World Health Organization/International Society and Federation of Cardiology Task Force on the Definition and Classification of cardiomyopathies.* Circulation, 1996. **93**(5): p. 841-2.
8. Japp, A.G., et al., *The Diagnosis and Evaluation of Dilated Cardiomyopathy.* J Am Coll Cardiol, 2016. **67**(25): p. 2996-3010.
9. Halliday, B.P., et al., *Sex- and age-based differences in the natural history and outcome of dilated cardiomyopathy.* Eur J Heart Fail, 2018. **20**(10): p. 1392-1400.
10. Schultheiss, H.P., et al., *Dilated cardiomyopathy.* Nat Rev Dis Primers, 2019. **5**(1): p. 32.
11. Jefferies, J.L. and J.A. Towbin, *Dilated cardiomyopathy.* Lancet, 2010. **375**(9716): p. 752-62.
12. Cresci, S., et al., *Clinical and genetic modifiers of long-term survival in heart failure.* J Am Coll Cardiol, 2009. **54**(5): p. 432-44.
13. Weintraub, R.G., C. Semsarian, and P. Macdonald, *Dilated cardiomyopathy.* Lancet, 2017. **390**(10092): p. 400-414.
14. McMurray, J.J.V. and M. Packer, *How Should We Sequence the Treatments for Heart Failure and a Reduced Ejection Fraction?: A Redefinition of Evidence-Based Medicine.* Circulation, 2021. **143**(9): p. 875-877.
15. Packer, M. and J.J.V. McMurray, *Rapid evidence-based sequencing of foundational drugs for heart failure and a reduced ejection fraction.* Eur J Heart Fail, 2021. **23**(6): p. 882-894.
16. Frustaci, A., M.A. Russo, and C. Chimenti, *Randomized study on the efficacy of immunosuppressive therapy in patients with virus-negative inflammatory cardiomyopathy: the TIMIC study.* Eur Heart J, 2009. **30**(16): p. 1995-2002.
17. Zhou, P. and W.T. Pu, *Recounting Cardiac Cellular Composition.* Circ Res, 2016. **118**(3): p. 368-70.
18. Martin, A.A., et al., *Cardiac Sarcomere Signaling in Health and Disease.* Int J Mol Sci, 2022. **23**(24).
19. Eisner, D.A., et al., *Calcium and Excitation-Contraction Coupling in the Heart.* Circ Res, 2017. **121**(2): p. 181-195.

20. Katrukha, I.A., *Human cardiac troponin complex. Structure and functions.* Biochemistry (Mosc), 2013. **78**(13): p. 1447-65.
21. Hershberger, R.E., A. Morales, and J.D. Siegfried, *Clinical and genetic issues in dilated cardiomyopathy: a review for genetics professionals.* Genet Med, 2010. **12**(11): p. 655-67.
22. Herman, D.S., et al., *Truncations of titin causing dilated cardiomyopathy.* N Engl J Med, 2012. **366**(7): p. 619-28.
23. De Paris, V., et al., *Pathophysiology*, in *Dilated Cardiomyopathy: From Genetics to Clinical Management*, G. Sinagra, M. Merlo, and B. Pinamonti, Editors. 2019, Springer

Copyright 2019, The Author(s). Cham (CH). p. 17-25.
24. Fernández-Solà, J., *The Effects of Ethanol on the Heart: Alcoholic Cardiomyopathy.* Nutrients, 2020. **12**(2).
25. Burridge, P.W., et al., *Human induced pluripotent stem cell-derived cardiomyocytes recapitulate the predilection of breast cancer patients to doxorubicin-induced cardiotoxicity.* Nat Med, 2016. **22**(5): p. 547-56.
26. Bourque, K., et al., *Biosensor-based profiling to track cellular signalling in patient-derived models of dilated cardiomyopathy.* Cell Signal, 2022. **91**: p. 110239.
27. Bristow, M.R., et al., *Decreased catecholamine sensitivity and beta-adrenergic-receptor density in failing human hearts.* N Engl J Med, 1982. **307**(4): p. 205-11.
28. Barry, W.H. and E.M. Gilbert, *How do beta-blockers improve ventricular function in patients with congestive heart failure?* Circulation, 2003. **107**(19): p. 2395-7.
29. Sabbah, H.N., *Biologic rationale for the use of beta-blockers in the treatment of heart failure.* Heart Fail Rev, 2004. **9**(2): p. 91-7.
30. Motiejunaite, J., L. Amar, and E. Vidal-Petiot, *Adrenergic receptors and cardiovascular effects of catecholamines.* Ann Endocrinol (Paris), 2021. **82**(3-4): p. 193-197.
31. Kawai, T., et al., *AT1 receptor signaling pathways in the cardiovascular system.* Pharmacol Res, 2017. **125**(Pt A): p. 4-13.
32. Hunyady, L. and K.J. Catt, *Pleiotropic AT1 receptor signaling pathways mediating physiological and pathogenic actions of angiotensin II.* Mol Endocrinol, 2006. **20**(5): p. 953-70.
33. De Mello, W.C. and A.H. Danser, *Angiotensin II and the heart : on the intracrine renin-angiotensin system.* Hypertension, 2000. **35**(6): p. 1183-8.
34. Dostal, D.E., et al., *Molecular mechanisms of angiotensin II in modulating cardiac function: intracardiac effects and signal transduction pathways.* J Mol Cell Cardiol, 1997. **29**(11): p. 2893-902.
35. Marasciulo, F.L., M. Montagnani, and M.A. Potenza, *Endothelin-1: the yin and yang on vascular function.* Curr Med Chem, 2006. **13**(14): p. 1655-65.
36. Pieske, B., et al., *Functional effects of endothelin and regulation of endothelin receptors in isolated human nonfailing and failing myocardium.* Circulation, 1999. **99**(14): p. 1802-9.
37. Gallo, S., et al., *ERK: A Key Player in the Pathophysiology of Cardiac Hypertrophy.* Int J Mol Sci, 2019. **20**(9).
38. Qin, J., et al., *Structures of PKA-phospholamban complexes reveal a mechanism of familial dilated cardiomyopathy.* Elife, 2022. **11**.

39. Lv, J., et al., *Phosphoproteomic Analysis Reveals Downstream PKA Effectors of AKAP Cypher/ZASP in the Pathogenesis of Dilated Cardiomyopathy.* Front Cardiovasc Med, 2021. **8**: p. 753072.
40. Chatzifrangkeskou, M., et al., *Cofilin-1 phosphorylation catalyzed by ERK1/2 alters cardiac actin dynamics in dilated cardiomyopathy caused by lamin A/C gene mutation.* Hum Mol Genet, 2018. **27**(17): p. 3060-3078.
41. Yang, J.H., et al., *PKA catalytic subunit compartmentation regulates contractile and hypertrophic responses to β-adrenergic signaling.* J Mol Cell Cardiol, 2014. **66**: p. 83-93.
42. Liu, Y., et al., *Physiological and pathological roles of protein kinase A in the heart.* Cardiovasc Res, 2022. **118**(2): p. 386-398.
43. Purcell, N.H., et al., *Genetic inhibition of cardiac ERK1/2 promotes stress-induced apoptosis and heart failure but has no effect on hypertrophy in vivo.* Proc Natl Acad Sci U S A, 2007. **104**(35): p. 14074-9.
44. Li, D.Y., et al., *Role of ERK1/2 in the anti-apoptotic and cardioprotective effects of nitric oxide after myocardial ischemia and reperfusion.* Apoptosis, 2006. **11**(6): p. 923-30.
45. Holubarsch, C., et al., *Existence of the Frank-Starling mechanism in the failing human heart. Investigations on the organ, tissue, and sarcomere levels.* Circulation, 1996. **94**(4): p. 683-9.
46. Jackson, G., et al., *ABC of heart failure. Pathophysiology.* Bmj, 2000. **320**(7228): p. 167-70.
47. Delicce, A.V. and A.N. Makaryus, *Physiology, Frank Starling Law*, in *StatPearls*. 2023, StatPearls Publishing

Copyright © 2023, StatPearls Publishing LLC.: Treasure Island (FL).

48. Mihl, C., W.R. Dassen, and H. Kuipers, *Cardiac remodelling: concentric versus eccentric hypertrophy in strength and endurance athletes.* Neth Heart J, 2008. **16**(4): p. 129-33.
49. Nakamura, M. and J. Sadoshima, *Mechanisms of physiological and pathological cardiac hypertrophy.* Nat Rev Cardiol, 2018. **15**(7): p. 387-407.
50. Gaasch, W.H. and M.R. Zile, *Left ventricular structural remodeling in health and disease: with special emphasis on volume, mass, and geometry.* J Am Coll Cardiol, 2011. **58**(17): p. 1733-40.
51. Lilly, L.S., *Pathophysiology of Heart Disease*. 5 ed. The Cardiomyopathies, ed. C. Lee. 2011, Baltimore, MD: Lippincott Williams & Williams Wolters Kluwer Health. 459.
52. Brown, N.J., *Contribution of aldosterone to cardiovascular and renal inflammation and fibrosis.* Nat Rev Nephrol, 2013. **9**(8): p. 459-69.
53. Frangogiannis, N.G., *Cardiac fibrosis.* Cardiovasc Res, 2021. **117**(6): p. 1450-1488.
54. Takahashi, K. and S. Yamanaka, *Induction of pluripotent stem cells from mouse embryonic and adult fibroblast cultures by defined factors.* Cell, 2006. **126**(4): p. 663-76.
55. Park, I.H., et al., *Generation of human-induced pluripotent stem cells.* Nat Protoc, 2008. **3**(7): p. 1180-6.
56. Jimenez-Tellez, N. and S.C. Greenway, *Cellular models for human cardiomyopathy: What is the best option?* World J Cardiol, 2019. **11**(10): p. 221-235.
57. Zaragoza, C., et al., *Animal models of cardiovascular diseases.* J Biomed Biotechnol, 2011. **2011**: p. 497841.
58. Chun, Y.S., K. Byun, and B. Lee, *Induced pluripotent stem cells and personalized medicine: current progress and future perspectives.* Anat Cell Biol, 2011. **44**(4): p. 245-55.

59. Aboul-Soud, M.A.M., A.J. Alzahrani, and A. Mahmoud, *Induced Pluripotent Stem Cells (iPSCs)-Roles in Regenerative Therapies, Disease Modelling and Drug Screening.* Cells, 2021. **10**(9).
60. Louch, W.E., K.A. Sheehan, and B.M. Wolska, *Methods in cardiomyocyte isolation, culture, and gene transfer.* J Mol Cell Cardiol, 2011. **51**(3): p. 288-98.
61. Lian, X., et al., *Directed cardiomyocyte differentiation from human pluripotent stem cells by modulating Wnt/β-catenin signaling under fully defined conditions.* Nature Protocols, 2013. **8**(1): p. 162-175.
62. Lian, X., et al., *Insulin inhibits cardiac mesoderm, not mesendoderm, formation during cardiac differentiation of human pluripotent stem cells and modulation of canonical Wnt signaling can rescue this inhibition.* Stem Cells, 2013. **31**(3): p. 447-57.
63. Yang, L., et al., *Human cardiovascular progenitor cells develop from a KDR+ embryonic-stem-cell-derived population.* Nature, 2008. **453**(7194): p. 524-8.
64. Sun, N., et al., *Patient-specific induced pluripotent stem cells as a model for familial dilated cardiomyopathy.* Sci Transl Med, 2012. **4**(130): p. 130ra47.
65. Cuello, F., et al., *Impairment of the ER/mitochondria compartment in human cardiomyocytes with PLN p.Arg14del mutation.* EMBO Mol Med, 2021. **13**(6): p. e13074.
66. Yamasaki, A.E., A.D. Panopoulos, and J.C.I. Belmonte, *Understanding the genetics behind complex human disease with large-scale iPSC collections.* Genome Biology, 2017. **18**(1): p. 135.
67. Eschenhagen, T. and L. Carrier, *Cardiomyopathy phenotypes in human-induced pluripotent stem cell-derived cardiomyocytes-a systematic review.* Pflugers Arch, 2019. **471**(5): p. 755-768.
68. Shah, D., et al., *Modeling of LMNA-Related Dilated Cardiomyopathy Using Human Induced Pluripotent Stem Cells.* Cells, 2019. **8**(6).
69. Wyles, S.P., et al., *Modeling structural and functional deficiencies of RBM20 familial dilated cardiomyopathy using human induced pluripotent stem cells.* Hum Mol Genet, 2016. **25**(2): p. 254-65.
70. Mosqueira, D., K. Lis-Slimak, and C. Denning, *High-Throughput Phenotyping Toolkit for Characterizing Cellular Models of Hypertrophic Cardiomyopathy In Vitro.* Methods Protoc, 2019. **2**(4).
71. Knight, W.E., et al., *Maturation of Pluripotent Stem Cell-Derived Cardiomyocytes Enables Modeling of Human Hypertrophic Cardiomyopathy.* Stem Cell Reports, 2021. **16**(3): p. 519-533.
72. Huethorst, E., et al., *Enhanced Human-Induced Pluripotent Stem Cell Derived Cardiomyocyte Maturation Using a Dual Microgradient Substrate.* ACS Biomater Sci Eng, 2016. **2**(12): p. 2231-2239.
73. Ramaccini, D., et al., *Mitochondrial Function and Dysfunction in Dilated Cardiomyopathy.* Front Cell Dev Biol, 2020. **8**: p. 624216.
74. Rohani, L., et al., *Reversible Mitochondrial Fragmentation in iPSC-Derived Cardiomyocytes From Children With DCMA, a Mitochondrial Cardiomyopathy.* Can J Cardiol, 2020. **36**(4): p. 554-563.
75. Zak, R., et al., *Mitochondrial proliferation in cardiac hypertrophy.* Basic Res Cardiol, 1980. **75**(1): p. 171-8.

76. Doherty, E. and A. Perl, *Measurement of Mitochondrial Mass by Flow Cytometry during Oxidative Stress.* React Oxyg Species (Apex), 2017. **4**(10): p. 275-283.
77. Mitra, K. and J. Lippincott-Schwartz, *Analysis of mitochondrial dynamics and functions using imaging approaches.* Curr Protoc Cell Biol, 2010. **Chapter 4**: p. Unit 4.25.1-21.
78. Elefantova, K., et al., *Detection of the Mitochondrial Membrane Potential by the Cationic Dye JC-1 in L1210 Cells with Massive Overexpression of the Plasma Membrane ABCB1 Drug Transporter.* Int J Mol Sci, 2018. **19**(7).
79. Shimada, T., et al., *Morphological studies of different mitochondrial populations in monkey myocardial cells.* Cell Tissue Res, 1984. **238**(3): p. 577-82.
80. Hackenbrock, C.R., *Ultrastructural bases for metabolically linked mechanical activity in mitochondria. I. Reversible ultrastructural changes with change in metabolic steady state in isolated liver mitochondria.* J Cell Biol, 1966. **30**(2): p. 269-97.
81. Wilding, J.R., et al., *Altered energy transfer from mitochondria to sarcoplasmic reticulum after cytoarchitectural perturbations in mice hearts.* J Physiol, 2006. **575**(Pt 1): p. 191-200.
82. Karbassi, E., et al., *Cardiomyocyte maturation: advances in knowledge and implications for regenerative medicine.* Nat Rev Cardiol, 2020. **17**(6): p. 341-359.
83. Voglhuber, J., et al., *Functional remodelling of perinuclear mitochondria alters nucleoplasmic Ca(2+) signalling in heart failure.* Philos Trans R Soc Lond B Biol Sci, 2022. **377**(1864): p. 20210320.
84. Shemer, Y., et al., *Investigating LMNA-Related Dilated Cardiomyopathy Using Human Induced Pluripotent Stem Cell-Derived Cardiomyocytes.* Int J Mol Sci, 2021. **22**(15).
85. Maurer, M., et al., *Impaired lamin localization to the nuclear envelope is responsible for nuclear damage in LMNA mutant iPSC-derived cardiomyocytes.* bioRxiv, 2021: p. 2021.10.30.466591.
86. Yang, J., et al., *Phenotypic Variability in iPSC-Induced Cardiomyocytes and Cardiac Fibroblasts Carrying Diverse LMNA Mutations.* Front Physiol, 2021. **12**: p. 778982.
87. Bray, M.-A., et al., *Cell Painting, a high-content image-based assay for morphological profiling using multiplexed fluorescent dyes.* Nature Protocols, 2016. **11**(9): p. 1757-1774.
88. Cimini, B.A., et al., *Optimizing the Cell Painting assay for image-based profiling.* bioRxiv, 2022: p. 2022.07.13.499171.
89. Guo, Y. and W.T. Pu, *Cardiomyocyte Maturation: New Phase in Development.* Circ Res, 2020. **126**(8): p. 1086-1106.
90. Maroli, G. and T. Braun, *The long and winding road of cardiomyocyte maturation.* Cardiovasc Res, 2021. **117**(3): p. 712-726.
91. Jiang, Y., et al., *Maturation of Cardiomyocytes Derived from Human Pluripotent Stem Cells: Current Strategies and Limitations.* Mol Cells, 2018. **41**(7): p. 613-621.
92. Li, A., et al., *Mitochondrial Dynamics in Adult Cardiomyocytes and Heart Diseases.* Front Cell Dev Biol, 2020. **8**: p. 584800.
93. Yang, X., L. Pabon, and C.E. Murry, *Engineering adolescence: maturation of human pluripotent stem cell-derived cardiomyocytes.* Circ Res, 2014. **114**(3): p. 511-23.
94. Yang, X., et al., *Fatty Acids Enhance the Maturation of Cardiomyocytes Derived from Human Pluripotent Stem Cells.* Stem Cell Reports, 2019. **13**(4): p. 657-668.
95. Horikoshi, Y., et al., *Fatty Acid-Treated Induced Pluripotent Stem Cell-Derived Human Cardiomyocytes Exhibit Adult Cardiomyocyte-Like Energy Metabolism Phenotypes.* Cells, 2019. **8**(9).

96. Isu, G., et al., *Fatty acid-based monolayer culture to promote in vitro neonatal rat cardiomyocyte maturation.* Biochim Biophys Acta Mol Cell Res, 2020. **1867**(3): p. 118561.
97. Lin, B., et al., *Culture in Glucose-Depleted Medium Supplemented with Fatty Acid and 3,3',5-Triiodo-l-Thyronine Facilitates Purification and Maturation of Human Pluripotent Stem Cell-Derived Cardiomyocytes.* Front Endocrinol (Lausanne), 2017. **8**: p. 253.
98. Malandraki-Miller, S., et al., *Changing Metabolism in Differentiating Cardiac Progenitor Cells-Can Stem Cells Become Metabolically Flexible Cardiomyocytes?* Front Cardiovasc Med, 2018. **5**: p. 119.
99. Shabani, P., et al., *Exogenous treatment with eicosapentaenoic acid supports maturation of cardiomyocytes derived from embryonic stem cells.* Biochem Biophys Res Commun, 2015. **461**(2): p. 281-6.
100. Yang, X., et al., *Tri-iodo-l-thyronine promotes the maturation of human cardiomyocytes-derived from induced pluripotent stem cells.* J Mol Cell Cardiol, 2014. **72**: p. 296-304.
101. Rog-Zielinska, E.A., et al., *Glucocorticoid receptor is required for foetal heart maturation.* Hum Mol Genet, 2013. **22**(16): p. 3269-82.
102. Parikh, S.S., et al., *Thyroid and Glucocorticoid Hormones Promote Functional T-Tubule Development in Human-Induced Pluripotent Stem Cell-Derived Cardiomyocytes.* Circ Res, 2017. **121**(12): p. 1323-1330.
103. Chirico, N., et al., *Small molecule-mediated rapid maturation of human induced pluripotent stem cell-derived cardiomyocytes.* Stem Cell Res Ther, 2022. **13**(1): p. 531.
104. Tian, Y. and E.E. Morrisey, *Importance of myocyte-nonmyocyte interactions in cardiac development and disease.* Circ Res, 2012. **110**(7): p. 1023-34.
105. Pasquier, J., et al., *Coculturing with endothelial cells promotes in vitro maturation and electrical coupling of human embryonic stem cell-derived cardiomyocytes.* J Heart Lung Transplant, 2017. **36**(6): p. 684-693.
106. Ieda, M., et al., *Cardiac fibroblasts regulate myocardial proliferation through beta1 integrin signaling.* Dev Cell, 2009. **16**(2): p. 233-44.
107. Giacomelli, E., et al., *Human-iPSC-Derived Cardiac Stromal Cells Enhance Maturation in 3D Cardiac Microtissues and Reveal Non-cardiomyocyte Contributions to Heart Disease.* Cell Stem Cell, 2020. **26**(6): p. 862-879.e11.
108. Theocharis, A.D., et al., *Extracellular matrix structure.* Adv Drug Deliv Rev, 2016. **97**: p. 4-27.
109. Ribeiro, A.J., et al., *Contractility of single cardiomyocytes differentiated from pluripotent stem cells depends on physiological shape and substrate stiffness.* Proc Natl Acad Sci U S A, 2015. **112**(41): p. 12705-10.
110. Xi, Y., et al., *Substrate Stiffness Alters Human Induced Pluripotent Stem Cell-derived Cardiomyocyte Differentiation And Maturation.* Circulation research, 2019. **140**.
111. Feaster, T.K., et al., *Matrigel Mattress: A Method for the Generation of Single Contracting Human-Induced Pluripotent Stem Cell-Derived Cardiomyocytes.* Circ Res, 2015. **117**(12): p. 995-1000.
112. Forte, G., et al., *Substrate stiffness modulates gene expression and phenotype in neonatal cardiomyocytes in vitro.* Tissue Eng Part A, 2012. **18**(17-18): p. 1837-48.
113. Herron, T.J., et al., *Extracellular Matrix-Mediated Maturation of Human Pluripotent Stem Cell-Derived Cardiac Monolayer Structure and Electrophysiological Function.* Circ Arrhythm Electrophysiol, 2016. **9**(4): p. e003638.

114. Martewicz, S., et al., *Substrate and mechanotransduction influence SERCA2a localization in human pluripotent stem cell-derived cardiomyocytes affecting functional performance.* Stem Cell Res, 2017. **25**: p. 107-114.
115. Xi, Y.S., Sheng-an; Mesquita, Fernanda; Hochman-Mendez, Camila; Lee, Po-Feng; So, Shuiping; Gu, Jianhua; Cheng, Jie; Sampaio, Luiz; Xiang, Meixiang; Taylor, Doris A, *Abstract 17119: substrate stiffness alters human induced pluripotent stem cell-derived cardiomyocyte differentiation and maturation*, in *Circulation*. 2019.
116. Crestani, T., et al., *Electrical stimulation applied during differentiation drives the hiPSC-CMs towards a mature cardiac conduction-like cells.* Biochem Biophys Res Commun, 2020. **533**(3): p. 376-382.
117. Ruan, J.L., et al., *Mechanical Stress Conditioning and Electrical Stimulation Promote Contractility and Force Maturation of Induced Pluripotent Stem Cell-Derived Human Cardiac Tissue.* Circulation, 2016. **134**(20): p. 1557-1567.
118. Machiraju, P. and S.C. Greenway, *Current methods for the maturation of induced pluripotent stem cell-derived cardiomyocytes.* World J Stem Cells, 2019. **11**(1): p. 33-43.
119. Seibertz, F., et al., *Electrophysiological and calcium-handling development during long-term culture of human-induced pluripotent stem cell-derived cardiomyocytes.* Basic Res Cardiol, 2023. **118**(1): p. 14.
120. Lewandowski, J., et al., *The impact of in vitro cell culture duration on the maturation of human cardiomyocytes derived from induced pluripotent stem cells of myogenic origin.* Cell Transplant, 2018. **27**(7): p. 1047-1067.
121. Lundy, S.D., et al., *Structural and functional maturation of cardiomyocytes derived from human pluripotent stem cells.* Stem Cells Dev, 2013. **22**(14): p. 1991-2002.
122. Kamakura, T., et al., *Ultrastructural maturation of human-induced pluripotent stem cell-derived cardiomyocytes in a long-term culture.* Circ J, 2013. **77**(5): p. 1307-14.
123. Ergir, E., et al., *Generation and maturation of human iPSC-derived 3D organotypic cardiac microtissues in long-term culture.* Scientific Reports, 2022. **12**(1): p. 17409.
124. Cho, J., et al., *From engineered heart tissue to cardiac organoid.* Theranostics, 2022. **12**(6): p. 2758-2772.
125. Shen, S., et al., *Physiological calcium combined with electrical pacing accelerates maturation of human engineered heart tissue.* Stem Cell Reports, 2022. **17**(9): p. 2037-2049.
126. Arslanova, A., et al., *Using hiPSC-CMs to Examine Mechanisms of Catecholaminergic Polymorphic Ventricular Tachycardia.* Curr Protoc, 2021. **1**(12): p. e320.
127. Zhu, L., et al., *Cardiac Organoids: A 3D Technology for Modeling Heart Development and Disease.* Stem Cell Rev Rep, 2022. **18**(8): p. 2593-2605.
128. Funakoshi, S., et al., *Generation of mature compact ventricular cardiomyocytes from human pluripotent stem cells.* Nature Communications, 2021. **12**(1): p. 3155.
129. Feyen, D.A.M., et al., *Metabolic Maturation Media Improve Physiological Function of Human iPSC-Derived Cardiomyocytes.* Cell Rep, 2020. **32**(3): p. 107925.
130. Okita, K., et al., *A more efficient method to generate integration-free human iPS cells.* Nature Methods, 2011. **8**(5): p. 409-412.
131. Chen, C.X., et al., *A Multistep Workflow to Evaluate Newly Generated iPSCs and Their Ability to Generate Different Cell Types.* Methods Protoc, 2021. **4**(3).

132. Lian, X., et al., *Directed cardiomyocyte differentiation from human pluripotent stem cells by modulating Wnt/β-catenin signaling under fully defined conditions.* Nat Protoc, 2013. **8**(1): p. 162-75.
133. Tohyama, S., et al., *Distinct Metabolic Flow Enables Large-Scale Purification of Mouse and Human Pluripotent Stem Cell-Derived Cardiomyocytes.* Cell Stem Cell, 2013. **12**(1): p. 127-137.
134. Bray, M.A., et al., *Cell Painting, a high-content image-based assay for morphological profiling using multiplexed fluorescent dyes.* Nat Protoc, 2016. **11**(9): p. 1757-74.
135. Beth, A.C., et al., *Optimizing the Cell Painting assay for image-based profiling.* bioRxiv, 2022: p. 2022.07.13.499171.
136. Rüegg, J.C., *Cardiac contractility: how calcium activates the myofilaments*. Naturwissenschaften, 1998. **85**(12): p. 575-82.
137. Forny, C., R. Sube, and E.A. Ertel, *Contractions of Human-iPSC-derived Cardiomyocyte Syncytia Measured with a Ca-sensitive Fluorescent Dye in Temperature-controlled 384-well Plates.* J Vis Exp, 2018(140).
138. Correia, C., et al., *Distinct carbon sources affect structural and functional maturation of cardiomyocytes derived from human pluripotent stem cells.* Sci Rep, 2017. **7**(1): p. 8590.
139. Kawaguchi, N., *Chapter Six - Adult Cardiac-Derived Stem Cells: Differentiation and Survival Regulators*, in *Vitamins & Hormones*, G. Litwack, Editor. 2011, Academic Press. p. 111-125.
140. Malek Mohammadi, M., et al., *The transcription factor GATA4 promotes myocardial regeneration in neonatal mice.* EMBO Mol Med, 2017. **9**(2): p. 265-279.
141. Tsui, J.H., et al., *Tunable electroconductive decellularized extracellular matrix hydrogels for engineering human cardiac microphysiological systems.* Biomaterials, 2021. **272**: p. 120764.
142. Paradis, A.N., M.S. Gay, and L. Zhang, *Binucleation of cardiomyocytes: the transition from a proliferative to a terminally differentiated state.* Drug Discov Today, 2014. **19**(5): p. 602-9.
143. Xiao, B., et al., *Flow Cytometry-Based Assessment of Mitophagy Using MitoTracker.* Front Cell Neurosci, 2016. **10**: p. 76.
144. Piquereau, J., et al., *Mitochondrial dynamics in the adult cardiomyocytes: which roles for a highly specialized cell?* Front Physiol, 2013. **4**: p. 102.
145. Caines, J.K., D.A. Barnes, and M.D. Berry, *The Use of Seahorse XF Assays to Interrogate Real-Time Energy Metabolism in Cancer Cell Lines.* Methods Mol Biol, 2022. **2508**: p. 225-234.
146. Derks, W. and O. Bergmann, *Polyploidy in Cardiomyocytes: Roadblock to Heart Regeneration?* Circ Res, 2020. **126**(4): p. 552-565.
147. Briganti, F., et al., *iPSC Modeling of RBM20-Deficient DCM Identifies Upregulation of RBM20 as a Therapeutic Strategy.* Cell Rep, 2020. **32**(10): p. 108117.
148. Brey, R.L., et al., *Effects of repeated freeze-thaw cycles on anticardiolipin antibody immunoreactivity.* Am J Clin Pathol, 1994. **102**(5): p. 586-8.
149. Correia, C., et al., *Distinct carbon sources affect structural and functional maturation of cardiomyocytes derived from human pluripotent stem cells.* Scientific Reports, 2017. **7**(1): p. 8590.
150. Ahmad, S., K.C. Wood, and J.E. Scott, *A high throughput proliferation and cytotoxicity assay for co-cultured isogenic cell lines.* MethodsX, 2022. **9**: p. 101927.

151. Hong, T. and R.M. Shaw, *Cardiac T-Tubule Microanatomy and Function.* Physiol Rev, 2017. **97**(1): p. 227-252.
152. Doerr, L., et al., *New easy-to-use hybrid system for extracellular potential and impedance recordings.* J Lab Autom, 2015. **20**(2): p. 175-88.
153. Parrotta, E.I., et al., *Modeling Cardiac Disease Mechanisms Using Induced Pluripotent Stem Cell-Derived Cardiomyocytes: Progress, Promises and Challenges.* Int J Mol Sci, 2020. **21**(12).
154. Feramisco, J.R. and S.H. Blose, *Distribution of fluorescently labeled alpha-actinin in living and fixed fibroblasts.* J Cell Biol, 1980. **86**(2): p. 608-15.
155. Jiang, C.L., et al., *Cell type determination for cardiac differentiation occurs soon after seeding of human-induced pluripotent stem cells.* Genome Biology, 2022. **23**(1): p. 90.
156. Karakikes, I., et al., *Human induced pluripotent stem cell-derived cardiomyocytes: insights into molecular, cellular, and functional phenotypes.* Circ Res, 2015. **117**(1): p. 80-8.
157. Sharma, A., J.C. Wu, and S.M. Wu, *Induced pluripotent stem cell-derived cardiomyocytes for cardiovascular disease modeling and drug screening.* Stem Cell Research & Therapy, 2013. **4**(6): p. 150.
158. Medvedev, S.P., E.A. Pokushalov, and S.M. Zakian, *Epigenetics of pluripotent cells.* Acta Naturae, 2012. **4**(4): p. 28-46.
159. Chamberlain, S.J., *Disease modelling using human iPSCs.* Human Molecular Genetics, 2016. **25**(R2): p. R173-R181.
160. Scesa, G., R. Adami, and D. Bottai, *iPSC Preparation and Epigenetic Memory: Does the Tissue Origin Matter?* Cells, 2021. **10**(6).
161. Li, Y. and R. Darabi, *Role of epigenetics in cellular reprogramming; from iPSCs to disease modeling and cell therapy.* J Cell Biochem, 2022. **123**(2): p. 147-154.
162. Hao, J. and Y. Liu, *Epigenetics of methylation modifications in diabetic cardiomyopathy.* Front Endocrinol (Lausanne), 2023. **14**: p. 1119765.
163. Cannatà, A., et al., *Sex Differences in the Long-term Prognosis of Dilated Cardiomyopathy.* Can J Cardiol, 2020. **36**(1): p. 37-44.
164. Taylor, C.N. and E.S. Lau, *Sex Differences in Cardiomyopathy.* Current Cardiovascular Risk Reports, 2022. **16**(11): p. 159-170.
165. Verdonschot, J.A.J., et al., *Phenotypic clustering of dilated cardiomyopathy patients highlights important pathophysiological differences.* European Heart Journal, 2021. **42**(2): p. 162-174.
166. Kyla, B., et al., *Effective use of genetically-encoded optical biosensors for profiling signalling signatures in iPSC-CMs derived from idiopathic dilated cardiomyopathy patients.* bioRxiv, 2022: p. 2022.09.06.506800.
167. Jones-Tabah, J., et al., *In vivo detection of GPCR-dependent signaling using fiber photometry and FRET-based biosensors.* Methods, 2022. **203**: p. 422-430.
168. Chavez-Abiega, S., et al., *Single-cell imaging of ERK and Akt activation dynamics and heterogeneity induced by G-protein-coupled receptors.* J Cell Sci, 2022. **135**(6).
169. Verdonschot, J.A.J., et al., *Phenotypic clustering of dilated cardiomyopathy patients highlights important pathophysiological differences.* Eur Heart J, 2021. **42**(2): p. 162-174.
170. Drakhlis, L., et al., *Human heart-forming organoids recapitulate early heart and foregut development.* Nat Biotechnol, 2021. **39**(6): p. 737-746.

171. Sparrow, A.J., et al., *Measurement of Myofilament-Localized Calcium Dynamics in Adult Cardiomyocytes and the Effect of Hypertrophic Cardiomyopathy Mutations.* Circ Res, 2019. **124**(8): p. 1228-1239.
172. Chen, Z., et al., *Subtype-specific promoter-driven action potential imaging for precise disease modelling and drug testing in hiPSC-derived cardiomyocytes.* European Heart Journal, 2017. **38**(4): p. 292-301.